# Spectroscopic Studies On Functional Nanohybrids And Their Potential Biological Applications

**THESIS**

**SUBMITTED FOR THE DEGREE OF**

**DOCTOR OF PHILOSOPHY (SCIENCE)**

**BY**

**ARPAN BERA**

**DEPARTMENT OF CHEMISTRY**

**UNIVERSITY OF CALCUTTA**

**2022**

*To My Family*

# *Acknowledgements*

*This gives me enormous pleasure and satisfaction to pay my admiration to those who have helped, motivated and contributed to accomplish my dissertation work. I would like to thank all of them for their kind support.*

*First and foremost, I owe my deepest gratitude to my enthusiastic supervisor, Professor Samir Kumar Pal, for providing me the opportunity to work under his supervision. I am very grateful for his constant motivation, belief in my capabilities and his persistent availability to clarify my doubts despite his extremely busy schedule. His immense knowledge in multidisciplinary field of science and technology, commitment to the highest scientific standards, unconditional support during crisis that, taken together, make him an exemplary mentor. I feel to be fortunate enough to learn from his instrumental expertise and detail insight into various experimental problems. This work would not have been possible without his thoughtful guidance, warm encouragement, unconditional support, constructive criticism with simultaneous allocation to express my ideas to work independently and his inexhaustible help. His positive vibes, everlasting energy, disciplined nature, great leadership quality and enduring willingness for learning motivates me substantially and thank you very much Sir for inspiring me to believe in my dreams.*

*I express my gratitude to all the faculty members and the office staffs of S. N. Bose National Centre for Basic Sciences for their assistances in my research career. A sincere appreciation to all other non-academic staffs and gardeners of SNBNCBS who have actively maintained the magnificent ambiance of the centre. I acknowledge Department of Science and Technology (DST), India for providing me INSPIRE fellowship as financial assistance.*

*I'd like to express my sincere gratitude to all my seniors and colleagues for providing an enriching work environment. I am especially thankful to Dr. Damayanti Bagchi for mentoring me at the initial stage of my research work. My sincere appreciation goes to all my seniors: Dr. Priya Singh, Dr. Jayita Patawari, Aniruddha, Dr. Tuhin Kumar Maji, Dr. Probir Kumar Sarkar, Dr. Animesh Halder, Dr. Tatini Rakshit, Dr. Soumendra Darbar, Soumendra da, Arkoda, pritamda and earlier lab-member Dr. Tanushree Dutta and Dr. Gulmi Chakraborty, Anindita, Sayan, Oiendrila and Sumana di. I acknowledge Prof. (Dr.) Ranjan Das for working with me on the topic of hybrid materials. My sincere admiration goes to all the present group members: Nur, Susmita, Dipanjan, Lopamudra, Amrita, Ria and nivedita for providing a homely and a cheerful environment, and also for assisting me during research work. Special thanks to nivedita, Nur & Dipanjan for their assistance in formatting and proof-reading of my thesis. Very special thanks to Nur and Dipanjan and Arkada with whom I shared many wonderful and glorious moments over the last four years. I also thank Arkada, Susmita and Ria with whom I shared many joyful moments in recent past. I pay tribute to all my teachers throughout my life. I also want to thank all my friends especially Nur, Dipanjan, Sourav, Arkada and Souvikda for their support and all the good times I shared with them.*

*Finally, I would like to pay high regards to my family and all of my relatives for their love, affection, praise, and good wishes. Without the enormous sacrifices of my Father and mother, encouragement and support from my elder sister and brother-in-law, fondness of my little niece and blessing from my uncle, this thesis would not have acquired its shape. I hereby acknowledge and thank all those who directly or indirectly supported me in this mesmerizing venture.*

*Dated:*

*Department of Chemical, Biological and Macromolecular Sciences,*
*S. N. Bose National Centre for Basic Sciences,*
*Salt Lake, Kolkata 700106, India* *(Arpan Bera)*

# CONTENTS

## Chapter 3: Instrumentation and Sample Preparation

# Chapter 1

# Introduction

## 1.1. Background:

The most emerging branch in pharmaceutical sciences known as "Pharmaceutical nanotechnology" presents new tools, opportunities and scope, which are expected to have significant applications in disease diagnostics and therapeutics. Recently nano-pharamceuticals reveal enormous potential in drug delivery as carrier for spatial and temporal delivery of bioactive and diagnostics. Additionally it also provides smart materials for tissue engineering. This discipline is now well-established for drug delivery, diagnostics, prognostic and treatment of diseases through its Nano engineered tools [1]. Some nanotech based products and delivery systems are already in market. Pharmaceutical nanotechnology comprised of nano-sized products which can be transformed in numerous ways to improve their characteristics. Drugs that are transformed into nano range offer some unique features which can lead to prolonged circulation, improved drug localization, enhanced drug efficacy etc. [2]. Various pharmaceutical nanotechnology based systems can be termed nanopharmaceuticals like polymeric nanoparticles, magnetic nanoparticles, liposomes, carbon nanotubes, quantum dots, dendrimers, metallic nanoparticles, polymeric nanoparticles, etc. have brought about revolutionary changes in drug delivery as well as the total medical service system. With the aid of nanopharmaceuticals, Pharmaceutical nanotechnology could have a profound influence on disease prevention to provide better insights into the molecular basis of disease [3]. However, some recently found health risk evidence limits their utilization in pharmaceutical industry. Some concerning issues like safety, bioethical issues, toxicity hazards, physiological and pharmaceutical challenges get to be resolved by the scientists. Current researchers are still lacking sufficient data and guidelines regarding safe use of these nanotechnology based devices and materials. Therefore pharmaceutical nanotechnology is still in infancy. The present chapter

summarizes the types of nanopharmaceuticals with the most important applications and nanoparticles associated with health risk information available now.

## 1.2. Nanoparticles:

A nanoparticle or ultrafine particle is usually defined as a particle of matter that is between 1 and 100 nanometres (nm) in diameter. The term is sometimes used for larger particles, up to 500 nm or fibers and tubes that are less than 100 nm in only two directions. At the lowest range, metal particles smaller than 1 nm are usually called atom clusters instead. Nanoparticles are usually distinguished from microparticles (1-1000 μm), "fine particles" (sized between 100 and 2500 nm), and "coarse particles" (ranging from 2500 to 10,000 nm), because their smaller size drives very different physical or chemical properties, like colloidal properties and ultrafast optical effects or electric properties [1]. Being more subject to the Brownian motion, they usually do not sediment, like colloidal particles that conversely are usually understood to range from 1 to 1000 nm. Being much smaller than the wavelengths of visible light (400-700 nm), nanoparticles cannot be seen with ordinary optical microscopes, requiring the use of electron microscopes or microscopes with laser. For the same reason, dispersions of nanoparticles in transparent media can be transparent, whereas suspensions of larger particles usually scatter some or all visible light incident on them. Nanoparticles also easily pass through common filters, such as common ceramic candles, so that separation from liquids requires special nanofiltration techniques.

In general, the small size of nanoparticles leads to a lower concentration of point defects compared to their bulk counterparts, but they do support a variety of dislocations that can be visualized using high-resolution electron microscopes. However, nanoparticles exhibit different dislocation mechanics, which, together with their unique surface structures, results in mechanical properties that are different from the bulk material.

Non-spherical nanonparticles (e.g., prisms, cubes, rods etc.) exhibit shape-dependent and size-dependent (both chemical and physical) properties (anisotropy). Non-

spherical nanoparticles of gold (Au), silver (Ag), and platinum (Pt) due to their fascinating optical properties are finding diverse applications. Non-spherical geometries of nanoprisms give rise to high effective cross-sections and deeper colors of the colloidal solutions. The possibility of shifting the resonance wavelengths by tuning the particle geometry allows using them in the fields of molecular labeling, biomolecular assays, trace metal detection, or nanotechnical applications. Anisotropic nanoparticles display a specific absorption behavior and stochastic particle orientation under unpolarized light, showing a distinct resonance mode for each excitable axis. This property can be explained by the fact that on a daily basis there are new developments being made in the field of synthesis of these nanoparticles for preparing them in high yield.

## 1.3. Hybrid Materials: A Brief Overview:

Hybrid materials are composites consisting of two distinct molecular components interacting at the microscopic level providing new characteristics or altered properties compared to the original constituents. The molecular cross-talking at the interface between the two constituents is often responsible to generate novel properties and improved activities in the hybrid material.[4] The molecular level interaction at the interface can be classified into two segments such as non-covalent (electrostatic, van der Waal etc.) interaction and covalent conjugation.[5] The hybrids formed through non-covalent and covalent interaction are often termed as class-I and II hybrids respectively. However, depending upon the nature and strength of interaction, the functionalities of the hybrids get altered. The hybrid materials with improved properties often depict superior functionalities.

The two counterparts of hybrid materials are divided into various sections. The classification of hybrid materials is a very subjective thing with different authors classifying them in different manners. This reflects the diversity of this field. Most commonly they are classified on the basis of the degree and nature of interaction between one inorganic and another organic building block assembled at the nanoscale. However, sometimes one organic material interacts with another organic dye at the nanoscale, imparting alteration in the dye characteristics. Organic

nanoparticles mainly focused on the generally coarse crystalline synthesis product into the finest particulate dispersion possible, with greater water stability which is essential for pharmaceutical activity [6]. These organic nanomaterials mainly consist of sizes between 50 to 500 nm. The other important classification is the inorganic-organic nanohybrids which mainly interact through covalent conjugation and surface attachment and thus can be included as class-II nanohybrids [7]. Hybrid organic-inorganic materials have been developed in the past 30 years or so, as intimate combinations of these dissimilar materials. The quantum leap in behavior often possible with hybrids arises principally from two sources: the reduction of the domain size of the inorganic phase to 100 nm or below (often much less), and generation of enormous interfacial areas, which enable numerous covalent bonds or other compatibilization between the phases. In some hybrid materials, the individual component has not been detected as a distinct phase. The realm of quantum effects and tunable electronic, optical, and magnetic properties are readily accessible in hybrid materials which extends its applicability [8].

## 1.4. Hybrid Materials of NIR Active Medicinally Important Molecules:

Medicines are most often organic compounds, which are divided into the broad classes of small organic molecules. Inorganic and organometallic compounds are also useful as drugs (e.g., lithium and platinum-based agents such as lithium carbonate and cis-platin as well as gallium) [9]. In case of medicinal activity, the drug molecules should have some molecular properties are important for a drug's pharmacokinetics in the human body, including their absorption, distribution, metabolism and excretion ("ADME") [10]. Hence, formulation of hybrid materials consisting of pharmaceutically relevant molecules as one of its primary components is very important. The ability to combine a multitude of organic and inorganic components in a modular fashion allows for systematic tuning of various properties including tuneable size, high drug loading, tailorable surface properties, controllable or stimuli responsive drug release kinetics, improved bioavailability, pharmacokinetics, and biocompatibility of the resultant hybrid material [11]. In general, small organic drug molecules can be entrapped within organic

nanoparticles (liposomes, dendrimers etc.) which led to formation of class-I hybrids that improve lipophilicity of drug with enhanced permeability and retention (EPR) effects [12]. On the other hand, using covalent conjugation strategy, medicines can form complexes or attached to the surface of an inorganic nano-dimensional system [13]. These class-II hybrids often lead to alteration of redox-modulatory properties with precise enhanced drug action.

For non-invasive photodynamic therapy (PDT) the efficiency of reactive oxygen species (ROS) generation by drug molecules has been taken under consideration. The photosensitizer (organic molecules or drug) absorbs light and generates ROS (such as singlet oxygen, hydroxyl radical, superoxide etc.) from neighbouring water and oxygen molecules. Amongst all, NIR (near infrared region) active photosensitizers are more potent for therapeutic applications. NIR light is less absorbed and scattered by human tissue and hence it has more penetration depth than visible light. In last few decades, some NIR medicinally relevant photosensitizers have been used in photodynamic therapy, bio imaging and others bio-medical applications. NIR cyanine dyes are the most promising in terms of bio-compatibility ability of ROS generation. They have also been utilized in photothermal therapy because of their photo thermal effect. But they have some limitation such as short circulation time, poor solubility in water and poor photostability. Hence, formulation of nanohybrid could achieve a huge impact for

## 1.5. Scope of the Spectroscopic Investigation on Hybrid:

The redox potential of electron transfer and trans-cellular bioavailability are the key parameters of redox active drug for biological activity. Both the parameters are expected to be influenced upon hybrid formation. Hybrid materials 1often offer modulated physico-chemical properties than the individual counterparts due to presence of interfacial junction [14]. Research on the transformed physicochemical properties of drug upon generation of hybrids has attracted attention of the scientific community as they have wide therapeutic applications to combat various life-threatening diseases. When multiple drug molecules bind to a single organic

nanoparticle (class I nanohybrid) bioavailability of the drug in the cells is increased. Thus, the localization and structure integrity of a drug essentially dictates the efficacy of the vehicle and the medicinal activity of the drug [15]. Hence it is important to study the interfacial dynamic. The class-II hybrids have stronger conjugation than class I hybrids. Besides, the proximity of the drug molecule to the inorganic counterparts would change the electron electronic properties (electron transfer process) of the drug [16]. The organic-inorganic interfacial charge transfer dynamics impose the overall activity of the composites. The photoelectron transfer process occurs from the LUMO of dye to the vacant molecular orbital of inorganic systems. The excited state photoelectron transfer process depicts the conjugation in the hybrid and the nature of hybridization [17]. In case of photosensitive drugs loaded nano-dimensional system, the photoinduced electron transfer process from dye to the inorganic counterpart results in production of reactive oxygen species (ROS). Hence, the formulation of these kinds of hybrids is superior to conventional medicine with respect to control release of drug, disease site-specific delivery and therapeutic effect. In this respect, synthesis and mechanism of different hybrid material formation is within the purview of our studies.

Microscopic characterization using electron microscopy such as scanning electron microscopy (SEM) [18], transmission electron microscopy (TEM) [19], scanning tunnelling microscopy (STM) [20] provide the information about the inorganic parts of the hybrid. High resolution transmission electron microscopy (HRTEM) could determine the lattice fringes and the crystal inter-planar distance. X-ray diffraction (XRD) is used for determining the crystal plane diffraction pattern of the inorganic parts. Atomic force microscopy (AFM) could provide the surface topology of the hybrid materials. However, Fourier-transform infrared spectroscopy (FTIR) and nuclear paramagnetic resonance spectroscopy (NMR) could determine the perturbation of the organic part during attachment with inorganic part. The change in signals of the drug molecules within the hybrids compared to the free drug molecules detects the nature of covalent conjugation. However, all those methods are only capable to study the nano-bio interface in an indirect manner, the nature of

organic bonds or the crystal structure of inorganic part. The study on interfacial dynamics in the hybrids could be sufficient to completely understand the interfacial properties. In order to study the interfacial dynamics, electronic spectroscopy including steady-state and excited state spectroscopy could be considered as one of the best available tools. Ultrashort pulsed lasers are the key for ultrafast laser spectroscopy to study the dynamics on extremely short fast scales (attoseconds to nanoseconds) [21]. There are several methods which have been used to examine dynamics of charge carriers, atoms and molecules. Time-correlated single photon counting (TCSPC) measures relaxation of molecules from an excited state to a lower energy state. Since various molecules in a sample will emit photons at different times depending their simultaneous excitation, the decay should have a certain rate rather than occurring at a specific time after excitation. By observing the time at which individual molecules take to emit their photons, and then combining all these data points, intensity vs. time graph can be generated that displays the exponential decay curve typical to these processes.

The key focus of this thesis is the investigation of excited-state dynamical processes at the heterogeneous interface of the hybrid materials. This is very important for both fundamental and application basis study. In one of our studies, we have explored the improvement of photostability of a well-known NIR cyanine dye (IR820) upon formulation of nanohybrid with semiconductor (ZnO NPs) nanoparticles. The study reveals the excited state photoelectron transfer process from the LUMO (lowest unoccupied molecular orbital) IR820 to the CB (conduction band) ZnO in the IR820-ZnO nanohybrid that alters its increment of photostability and overall activity for' potential biological applications. In another study, we have functionalized ZnO NPs with another well-known cyanine dye indocyanine green (ICG) and formulated ICG-ZnO nanohybrid. The excited state photoelectron transfer process in the nanohybrid enhances the overall production of reactive oxygen species (ROS) because free electrons and holes generate a huge amount of ROS from neighbouring water and oxygen molecule. Also, the attachment on the ZnO surface protects ICG from higher order H aggregation. In a recent study, we have utilized

the effect of duel sensitization for antibacterial photodynamic therapy (aPDT). At first, we have synthesized Au dopped ZnO NPs (Au-ZnO) and then functionalized by a well-known vitamin (riboflavin). The combined effect of dipolar coupling and excited state photoelectron transfer causes a huge charge separation in the Rf-Au-ZnO tri-hybrid which influences the efficient production of ROS under blue light excitation. We have demonstrated that the Rf-Au-ZnO nanohybrid exhibits enhanced aPDT activity compared to that of Rf-ZnO nanohybrid and other controls. We report the development of a sustained Zn micronutrient delivery system to engineer the surface of ZnO NPs in a facile route at room temperature. The overarching goal was to understand how the formation of the nanoheterojunctions and resultant change in the NP dissolution patterns could favour the Zn micronutrient management. In another study, we have synthesized MnS nanoparticles and functionalized by citrate. The surface modification by citrate makes it soluble in water. The citrate capped MnS NPs exhibit strong photoluminescence. UV-Vis absorption spectra explore the d-d and ligand to metal charge transfer (LMCT) band of MnS. It generates a huge amount of ROS in dark at acidic pH. The greater efficiency in ROS at pH 5 and pH 7 demonstrates bilirubin degradation and remarkable antimicrobial activity. The results obtained by all these studies of hybrid materials from synthesis to spectroscopic characterization to prevailing health benefits, could be incorporated in designing new-age hybrids for benefit of human health. We have successfully show**n** that the nanohybrid exhibits enhanced PDT activity compared to that of only drug. The hybrids are shown to **be** highly effective **in** destruction of drug resistance bacterial infection and their biofilm.

## 1.6. Objective:

The use of hybrid materials for their beneficial biological applications has attracted immense attention in recent time in order to address the healthcare challenges worldwide. Among them, metal-drug complexes, organic nanoparticles encapsulating drug molecules and semiconductor inorganic nanoparticles attached to drugs need to be evaluated in detail to understand the interfacial properties that are responsible for betterment in medicinal activity which could give rise to design

of heterostructures with efficient charge separation useful for various diseased conditions. The objective of this thesis is to fabricate various types of hybrid materials, unravel the ultrafast dynamical processes across the interface of heterostructures to enhance the medicinal efficiency. The special emphasis has been given to the correlation between the ultrafast processes at the interface and their implications in terms of improved biological applications.

Depending upon the nature and strength of interaction, the functionalities of the hybrids get altered. Thus, there is necessity to study the interfacial processes using experimental tools and to fully understand the interfacial dynamics at the nano-junction. The hybrid materials with improved properties often depict superior functionalities. The current generation of hybrids formed using commercially available drug molecules with some inorganic counterparts often enhance bioavailability and activity of the drug with an enhanced permeability and retention (EPR) effect at the target site [22]. Besides, the fabricated hybrid materials can incorporate 'sense and act' like stimuli responsive drug action and thus lowers the side effects of treatment [23-25]. The precise knowledge of interfacial charge transfer properties is important to fully understand the mechanism of drug action and their alteration upon hybrid formation within the scope of our studies. Besides, light-mediated treatment methodologies such as photodynamic therapy (PDT) involve photosensitizer molecules, which could be activated by specific photon energy followed by production of reactive oxygen species (ROS) for therapeutic use [26]. Therapeutic efficacy of photoactive drugs using near-infrared light can provide new avenues by using biological window of optical transparency [27]. This often suggests implication of a NIR-absorbing dye molecule or nanomaterials as a photosensitizer in PDT, which in turn improves the penetration potency of the light used. Recently, several NIR dyes have found application in PDT because of their better light absorptivity and ability in generating singlet oxygen [27-29]. Among them, ICG (Indocyanine green) and IR820 possess considerably low toxicity and very good biocompatibility compared to the other NIR dyes. One of the disabilities of these NIR dyes is poor photostability under NIR radiation [30, 31]. Basically, the

production of efficient singlet oxygen by cyanine dyes leads to oxidation of the dye ($^1O_2$, being low lying LUMO is a very strong oxidising agent) [32] that is responsible for its photo-degradation [33]. To control the problem of low photostability of these cyanine dyes, few methods have been reported [33, 34]. However, for all these methods complicated costly synthetic strategies are required. The present research includes studies on the photostability of a very well-known cyanine dye IR820. We have chosen semiconductor zinc oxide nanoparticles (ZnO NPs) and developed IR820 functionalized nanohybrid IR820-ZnO. We specifically select ZnO NPs due to their biocompatibility, low cost and ease of synthesis [35]. The excited state interaction between the ZnO and IR820 is thoroughly characterized using ultrafast spectroscopic tools. The photo-induced reactive oxygen species (ROS) such as super oxide, singlet were detected using appropriate molecular probes. The photostability of IR820 dye on ZnO surface is increased with a significant extent as compared to free IR820. A singlet oxygen quencher ($NaN_3$) was used to analyze the singlet oxygen mediated photodegradation of IR820 dye and its improvement of photostability on the surface of ZnO. Moreover, the hybrids show pH responsive drug delivery. The developed strategy could be applied for other NIR cyanine dyes that will improve their potential applications in light-harvesting fields. In this direction, we have fabricated a nanohybrid of ZnO nanoparticles (NP) and ICG which which provides lesser H-aggregation between ICG molecules on its surface and yield significantly greater amount of ROS relative to ICG upon photoexcitation, due to excited state electron transfer from ICG to ZnO. Classical MD simulation shows the dimeric structure of ICG breakes down on ZnO surface which corroborates results from the aggregation study in water. Density functional theory (DFT) along with time-dependent DFT studies elucidate that upon photoexcitation electron transfer takes place from the higher energy orbital of ICG to the conduction band of ZnO which is also explored from time resolved study. The greater efficiency in ROS generation by the ICG-ZnO nanohybrid than ICG or ZnO demonstrates remarkable antimicrobial activity against gram-negative bacteria *E. coli.*

Utilization of duel sensitization can be very useful in order to get more efficiency in photodynamic therapy. This novel approach is based on the fluorescence resonance

energy transfer (FRET) between covalently linked donor molecules to the acceptor, attached to the surface of semiconductor which has been previously used to enhance the efficiency in dye sensitized solar cell [36]. However, the implementation of this kind of system in PDT is not highlighted in the contemporary literatures. In this regard, development of organic/inorganic nanohybrid system using plasmonic NPs could be a better solution for the enhanced efficacy in PDT. In this direction, we have selected riboflavin (Rf) as a model photosensitizer, attached with Au decorated ZnO. Picosecond-resolved fluorescence study explores the excited-state photoelectron transfer process from Rf to ZnO and FRET from Rf to Au in Rf-ZnO-Au nanohybrids which has been confirmed by fluorescence transient of Rf-$Al_2O_3$-Au nanohybrid. The presence of Au influences huge charge separation in the Rf-ZnO-Au nanohybrid upon blue light irradiation which leads to greater production of ROS upon blue light irradiation. It provides promising aspect for the improvement of Visible/NIR light driven photodynamic therapy which could be translated into another suitable photosensitizer.

Nanoscale science and nanotechnology are expected to bring about revolutionary advances in agrochemical industry. Zinc (Zn) is a plant micronutrient required only in small quantities for optimum plant yield [37]. Zinc deficiency in crop (eg., wheat) plants poses a formidable challenge to global public health which has led to the development of biofortification [38] and ferti-forticitaion [39] methods of grain Zn enrichment. The solubility and dissolution (release) kinetics of ZnO NPs have been utilized as a source of Zn in Zn-deficient environments [40]. We have investigated Surface functionalized ZnO-based nanoformulations for the controlled release of Zn micronutrient in soil, which is a desirable feature for micronutrient delivery systems. In reflecting on the final outcome, this study reveals a promising strategy to reduce resource loss and environmental burden by judicious selection of nutrient forms, which signals the advent of need-based micronutrient delivery systems.

In the past few years, transition metal sulphide ($M_xS_y$) nanoparticles have attracted increasing attention from biomedical researchers across the globe, because of their exciting properties which have been mainly explored for energy- and catalysis-

related applications [41]. Whereas, it's biological applications are barely reported. Also, there are no reports of any synthesis and surface modification techniques for achieving MnS NPs having intrinsic photoluminescence. In this direction, we have synthesized MnS nanoparticles and functionalized by citrate. The surface modification by citrate makes it soluble in water. The citrate capped MnS NPs exhibits strong photoluminescence. UV-Vis absorption spectra explore the d-d and ligand to metal charge transfer (LMCT) band of MnS. It generates huge amount of ROS in dark at acidic pH. The greater efficiency in ROS at pH 5 and pH 6.5 demonstrates bilirubin degradation and remarkable antimicrobial activity. The results obtained by all these studies of hybrid materials from synthesis to spectroscopic characterization to prevailing health benefits, could be incorporated in designing new-age hybrids for benefit of human health.

## 1.7. Summary of the Work Done:

### 1.7.1. Spectroscopic Studies on NIR Active Nanohybrids for Potential Enhaced Biological Activity:

#### 1.7.1.1 Improvement of Photostability and NIR Activity of Cyanine Dye Through Nanohybrid Formation: Key Information From Ultrafast Dynamical Studies [42]:

NIR light harvesting has enormous importance for different potential applications in the modern era of research. Some NIR cyanine dyes such as IR820 have achieved great success in energy harvesting and cancer therapy. However, their action is limited for low photostability, considerable thermal degradation, short circulation times and nonspecific bio-distribution. Our present study is an attempt to overcome such limitations by attaching a model cyanine dye IR820 with ZnO nanoparticles. We have prepared IR820-ZnO nanohybrid and characterized it using microscopic and optical spectroscopic tools. Thermogravimetric analysis has shown greater thermal stability of IR820-ZnO nanohybrid compared to free dye. We have explored the enhancement in photostability of IR820 upon nanohybrid formation. We have detected generation of photo-induced reactive oxygen species (ROS) such as super oxide, singlet oxygen etc. using appropriate molecular probes. The formation of

IR820-ZnO nanohybrid reduces production of photo-induced singlet oxygen. However, it depicts an alternate trend in overall ROS formation (increases total ROS) under red light illumination. To correlate, enhanced photostability of IR820 on ZnO surface, we have explored excited state dynamical processes at the interface in nanohybrid. We have illustrated photoinduced excited state electron transfer process from LUMO of IR820 to conduction band of ZnO. This photo-electron transfer process enhances the production of ROS, decreases the formation of singlet oxygen that altogether leads to improvement in photostability and overall activity. A quencher of singlet oxygen sodium azide ($NaN_3$) was used to further confirm direct association of singlet oxygen generation with photostability issue of IR820. Also, ZnO is able to deliver the dye selectively in acidic environment that suggest its diseased site specific targeted activity. Our results provide a promising improvement for potential use of IR820 through formation of nanohybrid that could be translated for other NIR cyanine dyes.

## 1.7.2. Synthesis and combined Spectroscopic Computational Studies on a NIR-Active Nanohybrid for Potential Biological Application:

**1.7.2.1. Improving Therapeutic Potential of a NIR Photo-Sensitizer via Fabrication of Nanohybrids: An Optical Spectroscopic and Computational Study [43]:** Implementation of near infrared radiation (NIR) active drug in photodynamic therapy (PDT) is considered a highly promising alternative to traditional cure. Because of strong NIR absorbance, indocyanine green (ICG) has become attractive in emerging photo-theranostics. ICG generates single oxygen and shows photothermal effect under NIR irradiation. However, ICG is unable to produce sufficient amount of other reactive oxygen species (ROS) such as superoxide, hydroxyl radical. But, its ability of singlet oxygen generation under NIR irradiation is arrested by its tendency to aggregate in aqueous medium. Because of this limitation it shows better effectiveness in photothermal therapy than photodynamic agent. Herein, we have addressed to overcome this limitation via the fabrication of zinc oxide (ZnO) based ICG-ZnO nanohybrid which provides lesser H-aggregation between ICG molecules on its surface and yield significantly large amount of ROS relative to ICG upon

photoexcitation due to excited state electron transfer from ICG to ZnO. Also, this surface functionalization prevents ICG from aggregation in water significantly. Classical MD simulation shows the dimeric structure of ICG breakes down on ZnO surface which corroborates results from the aggregation study in water. Density functional theory (DFT) along with time-dependent DFT studies elucidate that upon photoexcitation electron transfer takes place from the lowest unoccupied molecular orbital of ICG to the conduction band of ZnO. The greater efficiency in ROS generation by the ICG-ZnO nanohybrid than ICG or ZnO demonstrates remarkable antimicrobial activity against gram-negative bacteria *E. coli.* Overall, the present study highlights the scope of developing ICG-ZnO nanohybrid as a highly efficient NIR agent for use in antibacterial photodynamic therapy as well as PDT.

## 1.7.3. Synthesis and Characterization of a Nanohybrid Through Surface Sensitization of an Oxide Material With Agriculturally-Relevant Organic Ligand for Sustained Delivery of Micronutrient:

**1.7.3.1. Surface Engineered ZnO-Humic/Citrate Interfaces: Photoinduced Charge Carrier Dynamics and Potential Application for Smart and Sustained Delivery of Zn Micronutrient [44]:** Nanoscale science and nanotechnology are expected to bring about revolutionary advances in the agrochemical industry. Smart delivery of micronutrients enabling sustained release is one such innovative approach to combat the poor nutrient uptake efficiency of conventional micronutrient sources. Herein, we report a bottom-up surface fabrication strategy to modify nanosized ZnO NPs surfaces at an atomic scale for sustained release of Zn micronutrients. A large sized environmentally relevant macromolecule humic acid (HA) and a comparatively smaller biologically pertinent citrate ligand were used to functionalize ZnO NPs (30 nm), and the resultant nanohybrids were characterized using electron microscopy, diffraction, and spectroscopic techniques. Functionalization with citrate ligand turns the NP smaller than its original size. The resultant modification in the dissolution characteristics of ZnO NPs leads to sustained release of Zn over a broad pH range. Functionalization with HA causes minimum alteration of NP sizes. But dissolution patterns of NPs examined separately in the presence of HA depicts stabilization of

colloidal suspensions. Additionally, picosecond-resolved lifetime measurements reveal efficient photoinduced charge transfer at the nanoheterojunction interfaces. To evaluate the impact of newly developed Zn delivery system on Zn bioavailability, their impacts on the growth of wheat plants (Triticum aestivum) was tested. Results reveal considerable growth enhancements of plants treated with functionalized NPs. The micronutrient nanoformulation requires no auxiliaries and is applicable to plant systems in aqueous dispersions. Our study reinstates the importance of "convergence thinking" or coming together of technologies as a key to creating a fundamental framework toward environmental sustainability.

## 1.7.4. Synthesis of Different Types of Metal Oxide Nanoparticles and to Study Their Activities for Potential Biological Applications:

**1.7.4.1. Dual-Sensitization via Electron and Energy Harvesting in a Nanohybrid for Improvement of Therapeutic Efficacy [45]:** We demonstrate experimental evidence of the effect of surface plasmon resonance of noble metal nanoparticles (NPs) on the activity of a well-known bio medicinal drug in proximity of a semiconductor having wide band gap for enhanced PDT efficacy. We have chosen riboflavin (Rf) (or vitamin B2) as a model photosensitizer, attached with ZnO NPs and further attached with gold (Au) NPs decorated ZnO to increase the efficiency. The synthesized nanohybrids are characterized with the help of different microscopic, optical spectroscopic and density functional theory (DFT) based techniques. The DFT and time dependent DFT based calculations validate the experimental findings. A detailed ultrafast spectroscopic study has been further carried out to study the excited state charge dynamics in the interface of the nanohybrids. The occurrence of Förster's Resonance Energy Transfer (FRET) between Rf and Au has been found to be the key reason for the increased efficiency in the Rf-ZnO-Au nanohybrid over the Rf-ZnO one. The dipolar coupling between Au and Rf in the Rf-ZnO-Au nanohybrid further facilities the generation of ROS in comparison to the Rf-ZnO under blue light irradiation. The greater efficiency in ROS generation by the Rf-ZnO-Au nanohybrid has been utilized for antimicrobial action against methicillin-resistant *S. aureus* (MRSA). Overall, the present study highlights

the duel sensitization for enhanced electron injection efficiency in Rf-ZnO-Au nanohybrid in order to use as antibacterial agent that could be translated in photodynamic therapy.

### 1.7.5. Synthesis of Different Metal Sulphide Nanoparticles for Their Light Harvesting Activity Including Anticancer Effects:

**1.7.5.1. Implementation of Surface Functionalization of MnS Nanoparticle for Achieving of Novel Optical Properties and Improving Therapeutic Potential:** In the past few years, metal sulfide nanoparticles (NPs) have been achieved enormous interest due to their photo and electrochemical properties, which can rival some metal oxide NPs. However, there are fewer reports on synthesis and surface functionalization to achieve intrinsic optical properties. Here, we demonstrate a novel synthesis and surface modification of manganese sulfide (MnS) NPs to achieve intrinsic photoluminescence and special electrochemical properties for potential therapeutic applications. The MnS NPs were characterized using microscopic and optical spectroscopic tools. Fourier-transform infrared spectroscopy (FTIR) demonstrates the binding of citrate on the surface of MnS NPs. The surface modification of insoluble as-prepared MnS NPs by citrate makes it soluble in water. The UV-Vis absorption spectra explore the d-d and ligand to metal charge transfer (LMCT) band of citrate-MnS. The citrate-MnS NPs exhibit strong photoluminescence. It generates a huge amount of ROS at neutral/acidic pH without any photo-activation. The higher efficiency in ROS generation at pH 5 and pH 7 demonstrates bilirubin degradation and remarkable antimicrobial activity against *Staphylococcus hominies* (*S. homins*). The results obtained by our present study from synthesis to spectroscopic characterization to prevailing health benefits which could be incorporated in designing new-age surface functionalized metal sulfide NPs for benefit of human health.

## 1.8. Plan of Thesis:

The plan of the thesis is as follows:

**Chapter 1**: This chapter gives a brief introduction to the scope and motivation behind the thesis work. A brief summary of the work done is also included in this chapter.

**Chapter 2:** This chapter provides a brief overview of the steady-state and dynamical tools, the structural aspects of dyes and fluorescent probes used in the experiments.

**Chapter 3:** Details of instrumentation, data analysis and experimental procedures have been discussed in this chapter.

**Chapter 4:** In this chapter, the improvement of photostability and NIR activity of a well-known cyanine dye (IR820) has been explained. The photostability and overall activity of IR820 is increased upon nanohybrid formation with ZnO NPs. The ultrafast excited state photoinduced charge transfer process explains the better photostability of IR820 on ZnO surface.

**Chapter 5:** In this chapter, we have explored to improve therapeutic potential of ICG as a NIR photosensitizer by functionalization with ZnO nanoparticles. The H-aggregation of ICG is reduced on the ZnO surface whereas the nanohybrid produces a huge amount ROS under red light irradiation. The nanohybrid shows strong antibacterial activity against well-known gram negative bacteria *E. coli*.

**Chapter 6:** This chapter provides a bottom-up surface functionalization strategy to modify nanosized zinc oxide (ZnO NPs) surface at an atomic scale for slow and sustained release of Zn micronutrient. The resultant modification in the dissolution characteristics of ZnO NPs leads to sustained release of Zn over a broad pH range.

**Chapter 7:** This chapter gives the experimental evidence of the effect of surface plasmon resonance of noble metal nanoparticles (NPs) on the activity of a well-known bio medicinal drug in proximity of a semiconductor having wide band gap for enhanced Photodynamic therapy (PDT) efficacy. The greater efficiency in ROS generation by the Rf-ZnO-Au nanohybrid has been utilized for antimicrobial action in dose-dependent manner against MRSA due to photoinduced ROS.

**Chapter 8:** This chapter demonstrate the implementation of MnS nanoparticles for potential use in biological application through the surface functionalization by citrate. The greater efficiency in ROS generation by the C-MnS in at pH 5 demonstrates remarkable antimicrobial activity against gram positive bacteria *Staphylococcus hominis*.

# References

[1] S. Bhatia, Nanoparticles types, classification, characterization, fabrication methods and drug delivery applications, in: Natural polymer drug delivery systems, *Springer* 2016, 33.

[2] M.Z.H. Saad, R. Jahan, U. Bagul, Nanopharmaceuticals: A new perspective of drug delivery system, *Asian J. Biomed. Pharm. Sci.* 2 (2012) 11.

[3] M. Prasad, U.P. Lambe, B. Brar, I. Shah, J. Manimegalai, K. Ranjan, R. Rao, S. Kumar, S. Mahant, S.K. Khurana, Nanotherapeutics: An insight into healthcare and multi-dimensional applications in medical sector of the modern world, *Biomed. Pharmacother.* 97 (2018) 1521.

[4] Y. Zhu, L. Li, C. Zhang, G. Casillas, Z. Sun, Z. Yan, G. Ruan, Z. Peng, A.-R.O. Raji, C. Kittrell, A seamless three-dimensional carbon nanotube graphene hybrid material, *Nat. Commun.* 3 (2012) 1225.

[5] P. GÃ3mez-Romero, C. Sanchez, Functional hybrid materials, *John Wiley & Sons* 2006.

[6] D. Horn, J. Rieger, Organic nanoparticles in the aqueous phase—theory, experiment, and use, *Angew. Chem.* 40 (2001) 4330.

[7] H. Ishii, K. Sugiyama, E. Ito, K. Seki, Energy level alignment and interfacial electronic structures at organic/metal and organic/organic interfaces, *Adv. Mater.* 11 (1999) 605.

[8] P.J. Hagrman, D. Hagrman, J. Zubieta, Organic–inorganic hybrid materials: From "simple" coordination polymers to organodiamine-templated molybdenum oxides, *Angew. Chem.* 38 (1999) 2638.

[9] D.S. Alberts, P. Liu, E.V. Hannigan, R. O'toole, S.D. Williams, J.A. Young, E.W. Franklin, D.L. Clarke-Pearson, V.K. Malviya, B. DuBeshter, Intraperitoneal cisplatin plus intravenous cyclophosphamide versus intravenous cisplatin plus intravenous cyclophosphamide for stage III ovarian cancer, *N. Engl. J. Med.* 335 (1996) 1950.

[10] A. Urtti, Challenges and obstacles of ocular pharmacokinetics and drug delivery, *Adv. Drug Deliv. Rev.* 58 (2006) 1131.

[11] E. Ruiz-Hitzky, K. Ariga, Y.M. Lvov, Bio-inorganic hybrid nanomaterials: Strategies, synthesis, characterization and applications, *Wiley-VCH* 2008.

[12] S. Mitragotri, P. Stayton, Organic nanoparticles for drug delivery and imaging, *MRS Bull.* 39 (2014) 219.

[13] T.Y. Ohulchanskyy, I. Roy, L.N. Goswami, Y. Chen, E.J. Bergey, R.K. Pandey, A.R. Oseroff, P.N. Prasad, Organically modified silica nanoparticles with covalently incorporated photosensitizer for photodynamic therapy of cancer, *Nano. Lett.* 7 (2007) 2835.

[14] J.B. Hall, M.A. Dobrovolskaia, A.K. Patri, S.E. McNeil, Characterization of nanoparticles for therapeutics, *Nanomedicine* 2 (2007) 789.

[15] T.S. Hauck, S. Giri, Y. Gao, W.C. Chan, Nanotechnology diagnostics for infectious diseases prevalent in developing countries, *Adv. Drug Deliv. Rev.* 62 (2010) 438.

[16] J.S. Walsh, G.T. Miwa, Bioactivation of drugs: Risk and drug design, *Annu. Rev. Pharmacol. Toxicol.* 51 (2011) 145.

[17] M.E. Davis, Z. Chen, D.M. Shin, Nanoparticle therapeutics: An emerging treatment modality for cancer, in, *World Sci.* 22 (2010) 239.

[18] J.-K.F. Suh, H.W. Matthew, Application of chitosan-based polysaccharide biomaterials in cartilage tissue engineering: A review, *Biomaterials* 21 (2000) 2589.

[19] T.K. Maji, D. Bagchi, P. Kar, D. Karmakar, S.K. Pal, Enhanced charge separation through modulation of defect-state in wide band-gap semiconductor for potential photocatalysis application: Ultrafast spectroscopy and computational studies, J. *Photochem. Photobiol. A* 332 (2017) 391.

[20] M.-C. Shih, S.-S. Li, C.-H. Hsieh, Y.-C. Wang, H.-D. Yang, Y.-P. Chiu, C.-S. Chang, C.-W. Chen, Spatially resolved imaging on photocarrier generations and band alignments at perovskite/$PbI_2$ heterointerfaces of perovskite solar cells by light-modulated scanning tunneling microscopy, *Nano. Lett. 17* (2017) 1154.

[21] S.K. Pal, A.H. Zewail, Dynamics of water in biological recognition, *Chem. Rev.* 104 (2004) 2099.

[22] H. Kobayashi, R. Watanabe, P.L. Choyke, Improving conventional enhanced permeability and retention (EPR) effects; what is the appropriate target?, *Theranostics* 4 (2014) 81.

[23] S. Mura, J. Nicolas, P. Couvreur, Stimuli-responsive nanocarriers for drug delivery, *Nat. Mater.* 12 (2013) 991.

[24] M.A.C. Stuart, W.T. Huck, J. Genzer, M. Müller, C. Ober, M. Stamm, G.B. Sukhorukov, I. Szleifer, V.V. Tsukruk, M. Urban, Emerging applications of stimuli-responsive polymer materials, *Nat. Mater.* 9 (2010) 101.

[25] R. Cheng, F. Meng, C. Deng, H.-A. Klok, Z. Zhong, Dual and multi-stimuli responsive polymeric nanoparticles for programmed site-specific drug delivery, *Biomaterials* 34 (2013) 3647.

[26] D.E. Dolmans, D. Fukumura, R.K. Jain, Photodynamic therapy for cancer, *Nat. Rev. Cancer* 3 (2003) 380.

[27] C. Wang, H. Tao, L. Cheng, Z. Liu, Near-infrared light induced *in vivo* photodynamic therapy of cancer based on upconversion nanoparticles, *Biomaterials* 32 (2011) 6145.

[28] R.L. Watley, S.G. Awuah, M. Bio, R. Cantu, H.B. Gobeze, V.N. Nesterov, S.K. Das, F. D'Souza, Y. You, Dual functioning thieno-pyrrole fused BODIPY dyes for NIR optical imaging and photodynamic therapy: Singlet oxygen generation without heavy halogen atom assistance, *Chem. Asian. J.* 10 (2015) 1335.

[29] B. Zhou, Y. Li, G. Niu, M. Lan, Q. Jia, Q. Liang, Near-infrared organic dye-based nanoagent for the photothermal therapy of cancer, *ACS Appl. Mater.* 8 (2016) 29899.

[30] A. Fernandez-Fernandez, R. Manchanda, T. Lei, D.A. Carvajal, Y. Tang, S.Z.R. Kazmi, A.J. McGoron, Comparative study of the optical and heat generation properties of IR820 and indocyanine green, *Mol. Imaging* 11 (2012) 7290.2011. 00031.

[31] N. Shao, Y. Qi, H. Lu, D. He, B. Li, Y. Huang, Photostability highly improved nanoparticles based on IR-780 and negative charged copolymer for enhanced photothermal therapy, *ACS Biomater. Sci. Eng.* 5 (2018) 795.

[32] A. Pajares, J. Gianotti, E. Haggi, G. Stettler, F. Amat-Guerri, S. Criado, S. Miskoski, N.A. García, Kinetic study of the singlet molecular oxygen-mediated

photodegradation of monohydroxylated N-heteroaromatic compounds, *J. Photochem. Photobiol. A* 119 (1998) 9.

[33] B.R. Renikuntla, H.C. Rose, J. Eldo, A.S. Waggoner, B.A. Armitage, Improved photostability and fluorescence properties through polyfluorination of a cyanine dye, *Org. Lett.* 6 (2004) 909.

[34] Q. Zheng, S. Jockusch, G.G. Rodríguez-Calero, Z. Zhou, H. Zhao, R.B. Altman, H.D. Abruña, S.C. Blanchard, Intra-molecular triplet energy transfer is a general approach to improve organic fluorophore photostability, *Photochem. Photobiol. Sci.* 15 (2016) 196.

[35] D. Bagchi, V.S. Rathnam, P. Lemmens, I. Banerjee, S.K. Pal, NIR-Light-active ZnO-based nanohybrids for bacterial biofilm treatment, *ACS omega* 3 (2018) 10877.

[36] C. Siegers, J. Hohl-Ebinger, B. Zimmermann, U. Würfel, R. Mülhaupt, A. Hinsch, R. Haag, A dyadic sensitizer for dye solar cells with high energy-transfer efficiency in the device, *ChemPhysChem* 8 (2007) 1548.

[37] S. Kabiri, F. Degryse, D.N. Tran, R.C. da Silva, M.J. McLaughlin, D. Losic, Graphene oxide: A new carrier for slow release of plant micronutrients, *ACS Appl. Mater. Interfaces* 9 (2017) 43325.

[38] I. Cakmak, M. Kalayci, Y. Kaya, A. Torun, N. Aydin, Y. Wang, Z. Arisoy, H. Erdem, A. Yazici, O. Gokmen, Biofortification and localization of zinc in wheat grain, *J. Agric. Food Chem.* 58 (2010) 9092.

[39] A. Dapkekar, P. Deshpande, M.D. Oak, K.M. Paknikar, J.M. Rajwade, Zinc use efficiency is enhanced in wheat through nanofertilization, *Sci. Rep.* 8 (2018) 6832.

[40] N. Milani, M.J. McLaughlin, S.P. Stacey, J.K. Kirby, G.M. Hettiarachchi, D.G. Beak, G. Cornelis, Dissolution kinetics of macronutrient fertilizers coated with manufactured zinc oxide nanoparticles, *J. Agric. Food Chem.* 60 (2012) 3991.

[41] A. Balakrishnan, J.D. Groeneveld, S. Pokhrel, L. Mädler, Metal sulfide nanoparticles: Precursor chemistry, *Chemistry* 27 (2021) 6390.

[42] A. Bera, D. Bagchi, S.K. Pal, Improvement of photostability and NIR activity of cyanine dye through nanohybrid formation: Key information from ultrafast dynamical studies, *J. Phys. Chem. A* 123 (2019) 7550.

[43] A. Bera, M.N. Hasan, U. Pal, D. Bagchi, T.K. Maji, T. S. Dasgupta, R. Das, S.K. Pal, Fabrication of nanohybrids toward improving therapeutic potential of a NIR photo-sensitizer: An optical spectroscopic and computational study, *J. Photochem. Photobiol. A* 424 (2022) 113610.

[44] T. Dutta, D. Bagchi, A. Bera, S. Das, T. Adhikari, S.K. Pal, Surface engineered ZnO-humic/citrate interfaces: Photoinduced charge carrier dynamics and potential application for smart and sustained delivery of zn micronutrient, *ACS Sustain. Chem. Eng.* 7 (2019) 10920.

[45] A. Bera, M.N. Hasan, A. Chatterjee, D. Mukherjee, S.K. Pal, Dual sensitization via electron and energy harvesting in a nanohybrid for improvement of therapeutic efficacy, *ACS Phys. Chem. Au* 3 (2022) 171.

# Chapter 2

# An Overview of Experimental Techniques and Systems

In order to investigate the dynamical processes involved in hybrid materials, different steady-state and dynamical tools have been employed. These include photoinduced electron transfer (PET), Förster resonance energy transfer (FRET) and distance distribution from FRET. In this chapter, we have included a brief discussion about the above-mentioned tools. Overviews of the various systems, probes and dyes used in the studies have also been provided.

## 2.1. Steady-State and Dynamical Tools:

**2.1.1. Photoinduced Electron Transfer (PET):** PET can be described as the movement of an electron caused by the absorption of light from an electron-rich species (D) to an electron deficient species (A), as shown in equation 2.1.

$$D + A \rightarrow D^+ + A^- \tag{2.1}$$

The first law of photochemistry tells us that a photoinduced process must be initiated by the absorption of light. In PET, the absorbing species can either be a donor, the acceptor, or a ground-state complex between the donor and acceptor, often referred to as a charge transfer complex. These possibilities are shown in equations 2.2−2.4.

$$D \xrightarrow{h\upsilon} D^* + A \longrightarrow D^+ + A^- \tag{2.2}$$

$$A \xrightarrow{h\upsilon} A^* + D \longrightarrow D^+ + A^- \tag{2.3}$$

$$(D \cdots A) \xrightarrow{h\upsilon} (D \cdots A)^* \longrightarrow D^+ + A^- \tag{2.4}$$

Transport of charges or excitons are commonly seen as fundamental processes in many optoelectronic devices as well as biological systems. The creation, diffusion,

and annihilation of excitons and the mobility of charges are some of the key processes in many light-responsive assemble structures of biological significance [1]. PET is an important process in many biochemical systems, such as those in respiration and photosynthesis [2, 3]. To gain a deep understanding for these systems, it is important to describe the rates of these processes with a few empirically derived parameters [4]. Therefore, it has become increasingly important to develop computational techniques that allow us to calculate the rate of charge or energy transport. In our systems the apparent rate constants, $k_{nr}$, were determined for the nonradiative processes by comparing the lifetimes of donor in the absence ($\tau_0$) and in the presence ($\tau$) of an acceptor, using equation 2.5.

$$k_{nr} = 1/\langle\tau\rangle - 1/\langle\tau_0\rangle \qquad (2.5)$$

The direction of electron transfer in the excited state is determined by the oxidation and reduction potential of the ground and excited states. Upon excitation the electron donor transfers an electron to the acceptor with a rate $k_{nr}$, forming the charge transfer complex. This complex may emit as an exciplex ($\eta\nu_E$) or be quenched and return to the ground state. The important part of this process is the decrease in total energy of the charge transfer complex. The energy decreases because the ability to donate or accept electrons changes when a fluorophore is in the excited state. Excitation provides the energy to drive charge separation. D and A do not form a complex when both are in the ground state because this is energetically unfavorable. The energy released by electron transfer can also change if the ions become solvated and/or separated in a solvent with a high dielectric constant. This thesis demonstrates several PET processes, particularly in hybrid materials and discusses the consequences of various interfacial electron transfer processes in dye/semiconductor system including a series of charge transfer processes which occur cooperatively.

**2.1.2. Förster Resonance Energy Transfer (FRET):** FRET is an electrodynamic phenomenon involving the nonradiative transfer of the excited state energy from

the donor dipole (D) to an acceptor dipole (A) in the ground state (Figure 2.1.a). Basically, FRET is of two types: (i) homo-molecular FRET and (ii) hetero-molecular FRET. In the former case the same fluorophore acts both as energy donor and acceptor, while in the latter case two different molecules act as donor and acceptor [5].Each donor-acceptor (D-A) pair participating in FRET is characterized by a distance known as Förster distance ($R_0$) i.e., the D-A separation at which energy transfer is 50% efficient. The rate of resonance energy transfer ($k_T$) from donor to an acceptor is given by [6],

$$k_T = \frac{1}{\tau_D}\left(\frac{R_0}{r}\right)^6 \tag{2.6}$$

where $\tau_D$ is the lifetime of the donor in the absence of acceptor and $r$ is the donor to acceptor (D-A) distance. The rate of transfer of donor energy depends upon the extent of overlap of the emission spectrum of the donor with the absorption spectrum of the acceptor ($J(\lambda)$), the quantum yield of the donor ($Q_D$), the relative orientation of the donor and acceptor transition dipoles ($\kappa^2$) and the distance between the donor and acceptor molecules ($r$) (Figure 2.1.b). In order to estimate FRET efficiency of the donor and hence to determine distances between donor-acceptor pairs, the methodology described below is followed [7]. $R_0$ is given by,

$$R_0 = 0.211\left[\kappa^2 n^{-4} Q_D J(\lambda)\right]^{1/6} \text{ (in Å)} \tag{2.7}$$

where $n$ is the refractive index of the medium, $Q_D$ is the quantum yield of the donor and $J(\lambda)$ is the overlap integral. $\kappa^2$ is defined as,

$$\kappa^2 = \left(\cos\theta_T - 3\cos\theta_D \cos\theta_A\right)^2 = \left(\sin\theta_D \sin\theta_A \cos\varphi - 2\cos\theta_D \cos\theta_A\right)^2 \tag{2.8}$$

where $\theta_T$ is the angle between the emission transition dipole of the donor and the absorption transition dipole of the acceptor, $\theta_D$ and $\theta_A$ are the angles between these dipoles and the vector joining the donor and acceptor and $\varphi$ is angle between the planes of the donor and acceptor (Figure 2.1.b). $\kappa^2$ value can vary from 0 to 4. For collinear and parallel transition dipoles, $\kappa^2 = 4$; for parallel dipoles, $\kappa^2 = 1$; and

for perpendicularly oriented dipoles, $\kappa^2 = 0$. For donor and acceptors that randomize by rotational diffusion prior to energy transfer, the magnitude of $\kappa^2$ is assumed to be 2/3.

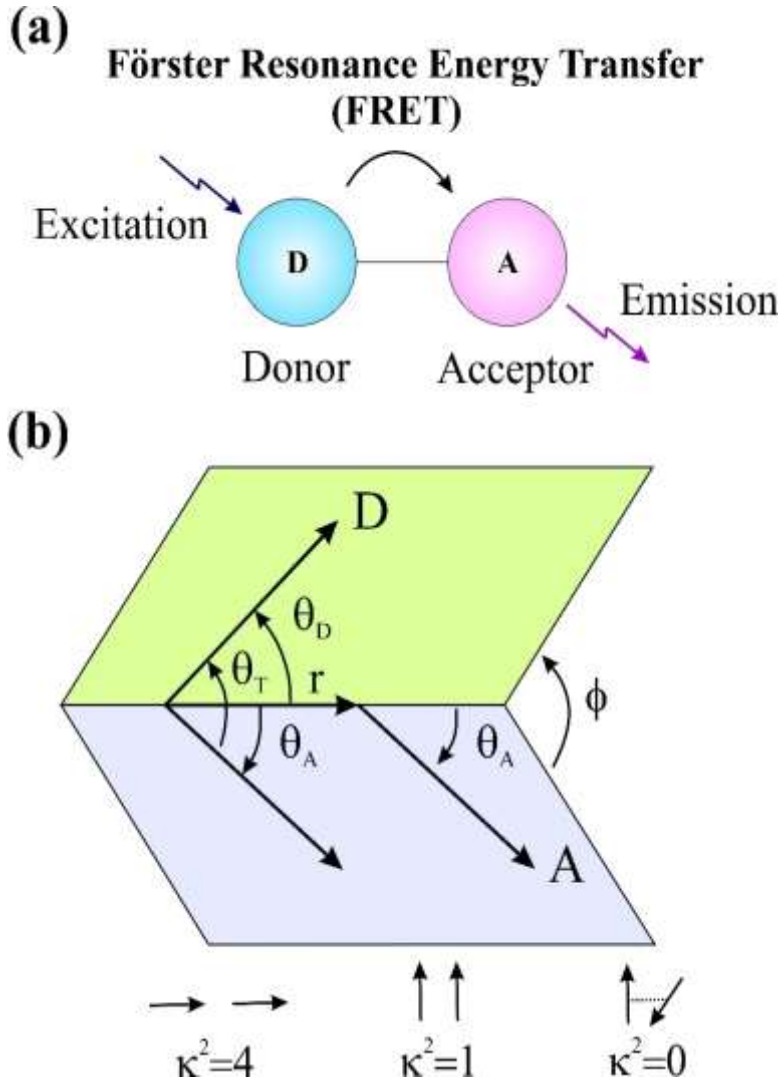


***Figure 2.1.*** *(a) Schematic illustration of the FRET process (b) Dependence of the orientation factor $\kappa^2$ on the directions of the emission and absorption dipoles of the donor and acceptor, respectively.*

However, in systems where there is a definite site of attachment of the donor and acceptor molecules, to get physically relevant results, the value of $\kappa^2$ has to be estimated from the angle between the donor emission and acceptor absorption dipoles. $J(\lambda)$, the overlap integral, which expresses the degree of spectral overlap between the donor emission and the acceptor absorption, is given by [8], where $F_D(\lambda)$ is the fluorescence intensity of the donor in the wavelength range of $\lambda$ to

$\lambda+d\lambda$ and is dimensionless. $\varepsilon_A(\lambda)$ is the extinction coefficient (in $M^{-1}cm^{-1}$) of the acceptor at $\lambda$. If $\lambda$ is in nm, then $J(\lambda)$ is in units of $M^{-1}\,cm^{-1}\,nm^4$.

$$J(\lambda) = \frac{\int_0^\infty F_D(\lambda)\varepsilon_A(\lambda)\lambda^4 d\lambda}{\int_0^\infty F_D(\lambda)d\lambda} \tag{2.9}$$

Once the value of $R_0$ is known, the efficiency of energy transfer can be calculated. The efficiency of energy transfer ($E$) is the fraction of photons absorbed by the donor which are transferred to the acceptor and is defined as,

$$E = \frac{k_T(r)}{\tau_D^{-1} + k_T(r)} \tag{2.10}$$

$$\text{Or, } E = \frac{R_0^6}{r^6 + R_0^6} \tag{2.11}$$

For D-A systems decaying with multiexponential lifetimes, $E$ is calculated from the amplitude weighted lifetimes $\langle\tau\rangle = \sum_i \alpha_i\tau_i$ of the donor in absence ($\tau_D$) and presence ($\tau_{DA}$) of the acceptor as,

$$E = 1 - \frac{\tau_{DA}}{\tau_D} \tag{2.12}$$

The D-A distances can be measured using equations (2.11) and (2.12).

**2.1.3. Data Analysis of Time-Resolved Fluorescence Transients:** Curve fitting of the time-resolved fluorescence transients was carried out using a nonlinear least square fitting procedure to a function (2.13) comprised of convolution of the IRF

$$(X(t) = \int_0^t E(t')R(t-t')dt') \tag{2.13}$$

($E$(t)) with a sum of exponentials (2.14) with pre-exponential factors ($B_i$),

$$(R(t) = A + \sum_{i=1}^{N} B_i e^{-t/\tau_i}) \tag{2.14}$$

characteristic lifetimes ($\tau_i$) and a background ($A$). Relative concentration in a multiexponential decay is expressed as (2.15).

$$c_n = \frac{B_n}{\sum_{i=1}^{N} B_i} \times 100 \tag{2.15}$$

The average lifetime (amplitude-weighted) of a multiexponential decay is expressed as,

$$\tau_{av} = \sum_{i=1}^{N} c_i \tau_i \tag{2.16}$$

**2.1.4. Distance Distribution between Donor and Acceptor:** Distance distribution between donor and acceptor was estimated according to the procedure described in the literature [8]. The observed fluorescence transients of the donor molecules in absence of acceptor were fitted using a nonlinear least-squares fitting procedure (software SCIENTIST) to the following function,

$$I_D(t) = \int_0^t E(t')\, p(t'-t)\, dt' \tag{2.17}$$

which comprises the convolution of the instrument response function (IRF) ($E(t)$) with exponential $\left(p(t) = \sum_i \alpha_{Di} \exp(-t/\tau_{Di})\right)$. The convolution of the distance distribution function $P(r)$ in the fluorescence transients of donor in presence of acceptor in the system under studies is estimated using the same software (SCIENTIST) in the following way.

The intensity decay of D-A pair, spaced at a distance $r$, is given by

$$I_{DA}(r,t) = \sum_i \alpha_{Di} \exp\left[ -\frac{t}{\tau_{Di}} - \frac{t}{\tau_{Di}} \left( \frac{R_0}{r} \right)^6 \right] \tag{2.18}$$

and the intensity decay of the sample considering distance distribution probablity function, $P(r)$ is given by,

$$I_{DA}(t) = \int_{r=0}^{\infty} P(r) I_{DA}(r,t)\, dr \tag{2.19}$$

where *P(r)* consist of the folowing terms:

$$P(r) = \frac{1}{\sigma\sqrt{2\pi}} \exp\left[ -\frac{1}{2}\left( \frac{\bar{r} - r}{\sigma} \right)^2 \right] \tag{2.20}$$

In this equation $\bar{r}$ is the mean of the Gaussian with a standard deviation of $\sigma$. Usually, distance distributions are described by the full width at half maxima (*hw*). This half width is given by $hw = 2.354\sigma$.

**2.2. Molecular Probes:** In this section, we will discuss about the different probe molecules that have been used in the course of study.

**2.2.1. Indocyanine Green (IR820):** IR820 is an indocyanine dye, which has a broad absorption band at 820 nm in methanol. It is a near infrared dye (NIR) with a molar absorptivity of 72 x $10^4$ $dm^3mol^{-1}cm^{-1}$ in water. It is a cost-effective imaging agent with low cytotoxicity. It can be used for image guided photothermal therapy for the treatment of cancer. It is also used as a contrasting agent for the detection and quantification of infected tissues in animals.

**2.2.2. Indocyanine Green (ICG):** ICG is a cyanine dye used in medical diagnostics. It is used for determining cardiac output, hepatic function, liver and gastric blood flow, and for ophthalmic angiography. It has a peak spectral absorption at about 800 nm. These infrared frequencies penetrate retinal layers, allowing ICG angiography to image deeper patterns of circulation than fluorescein angiography. ICG binds tightly to plasma proteins and becomes confined to the vascular system. ICG has a half-life of 150 to 180 seconds and is removed from circulation exclusively by the liver to bile juice.

**2.2.3. Riboflavin (Rf):** Riboflavin is a water-soluble member of the B-vitamin family. It is essential to the formation of two major coenzymes, flavin mononucleotide and flavin adenine dinucleotide. These coenzymes are involved in energy metabolism, cellular respiration, and antibody production, as well as normal growth and development. The coenzymes are also required for the

metabolism of niacin, vitamin $B_6$, and folate. Riboflavin is prescribed to treat corneal thinning, and taken orally, may reduce the incidence of migraine headaches in adults. It is found in food and sold as a dietary supplement. Sufficient dietary and supplemental Rf intake appears to have a protective effect on various medical conditions such as sepsis, ischemia etc., while it also contributes to the reduction in the risk of some forms of cancer in humans. These biological effects of RF have been widely studied for their anti-oxidant, anti-aging, anti-inflammatory, anti-nociceptive and anti-cancer properties. Moreover, the combination of Rf and other compounds or drugs can have a wide variety of effects and protective properties, and diminish the toxic effect of drugs in several treatments.

**2.2.4. Dichlorofluorescin (DCFH):** Dichlorofluorescin (DCFH) is a probe that is trapped within cells and is easily oxidized to fluorescent dichlorofluorescein (DCF) [9]. Dichlorofluorescin (DCFH) is non-fluorescent which convert to fluorescent DCF upon oxidation through reacting with reactive oxygen species (ROS). This quantifies amount of ROS as well as cellular oxidative stress.

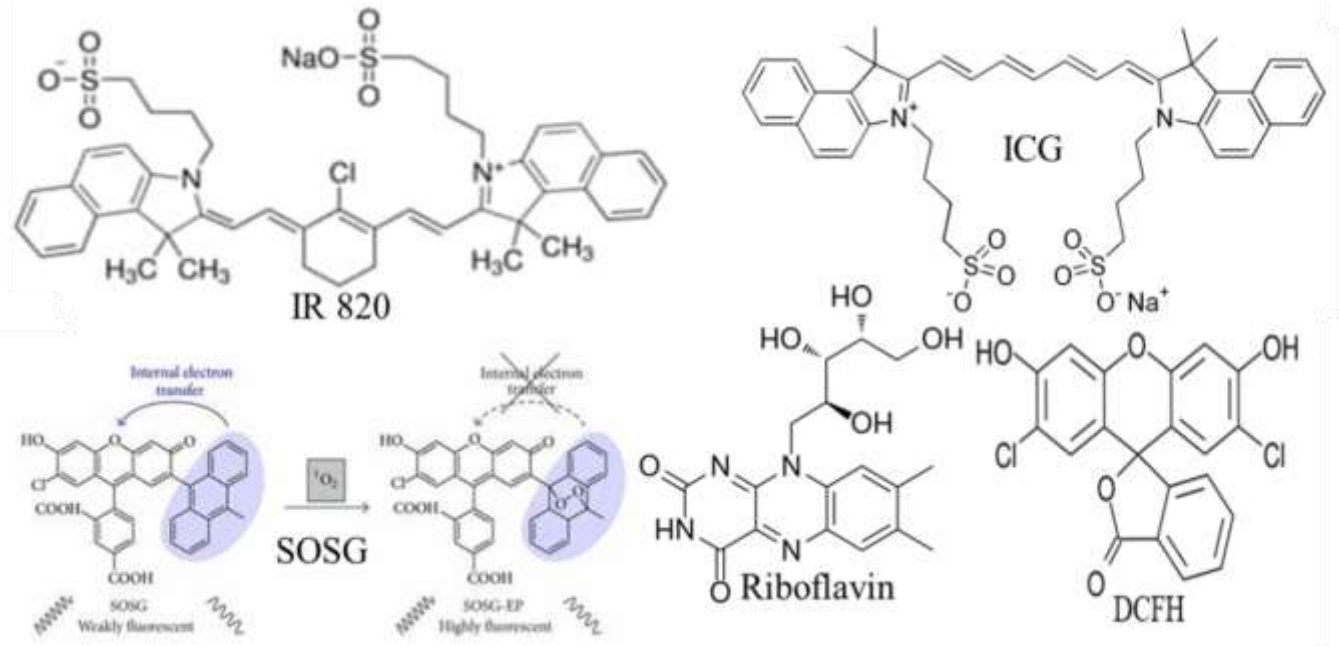


***Figure* 2.2.** *Schematic representation of the molecular probes used.*

**2.2.5. Singlet Oxygen Sensor Sensor Green (SOSG):** Singlet Oxygen Sensor Green is a detection reagent that is highly selective for singlet oxygen Unlike other available fluorescent and chemiluminescent singlet oxygen detection reagents Singlet Oxygen Sensor Green does not show any appreciable response to hydroxyl radical or superoxide This indicator initially exhibits weak blue fluorescence but in the presence of singlet oxygen it emits a green fluorescence excitation emission maxima.

## References


[1] Y. Shirota, H. Kageyama, Charge carrier transporting molecular materials and their applications in devices, *Chem. Rev.* 107 (2007) 953.

[2] H.B. Gray, J.R. Winkler, Electron tunneling through proteins, *Q. Rev. Biophys.* 36 (2003) 341.

[3] G. McLendon, R. Hake, Interprotein electron transfer, *Chem. Rev.* 92 (1992) 481.

[4] V. Kenkre, J.D. Andersen, D. Dunlap, C. Duke, Unified theory of the mobilities of photoinjected electrons in naphthalene, *Phys. Rev. Lett.* 62 (1989) 1165.

[5] L. Stryer, Fluorescence energy transfer as a spectroscopic ruler, *Annu. Rev. Biochem.* 47 (1978) 819.

[6] J.R. Lakowicz, Principles of fluorescence spectroscopy, *Springer Science & Business Media* 2013.

[7] D. Banerjee, S.K. Pal, Simultaneous binding of minor groove binder and intercalator to dodecamer DNA: Importance of relative orientation of donor and acceptor in FRET, *J. Phys. Chem. B* 111 (2007) 5047.

[8] S. Batabyal, T. Mondol, S.K. Pal, Picosecond-resolved solvent reorganization and energy transfer in biological and model cavities, *Biochimie* 95 (2013) 1127.

[9] S. Sardar, S. Chaudhuri, P. Kar, S. Sarkar, P. Lemmens, S.K. Pal, Direct observation of key photoinduced dynamics in a potential nano-delivery vehicle of cancer drugs, *Phys. Chem. Chem. Phys.* 17 (2015) 166.

# Chapter 3

# Instrumentation and Sample Preparation

In this chapter, the details of instrumental setup and sample preparation techniques used in the thesis work have been described.

## 3.1. Instrumental Setups:

**3.1.1. Steady-State UV-Vis Absorption and Emission Measurement:** Steady-state UV-Vis absorption and emission spectra were measured with Shimadzu UV-2600 spectrophotometer and Horiba Fluorolog, respectively. Schematic ray diagrams of these two instruments are shown in Figures 3.1 and 3.2.

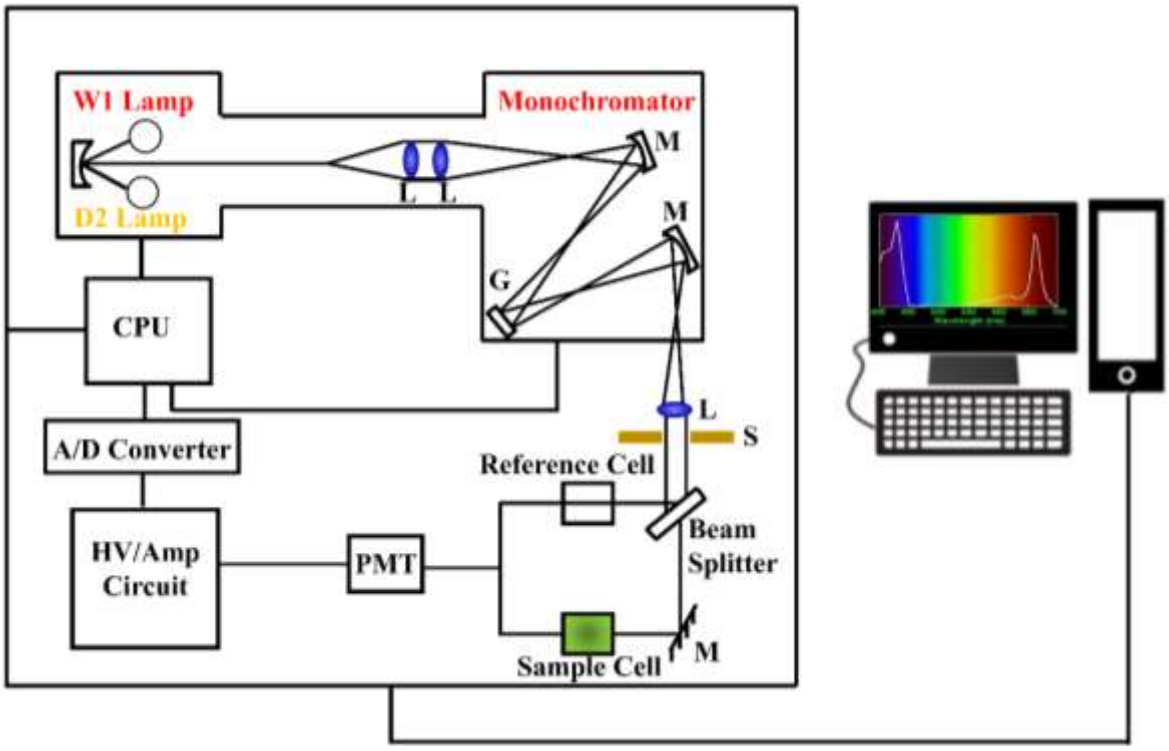


***Figure 3.1.*** *Schematic ray diagram of an absorption spectrophotometer. Tungsten halogen (W1) and deuterium lamps (D2) are used as light sources in the visible and UV regions, respectively. M, G, L, S, PMT designate mirror, grating, lens, shutter and photomultiplier tube, respectively. CPU, A/D converter and HV/amp indicate central processing unit, analog to digital converter and high-voltage/amplifier circuit, respectively.*

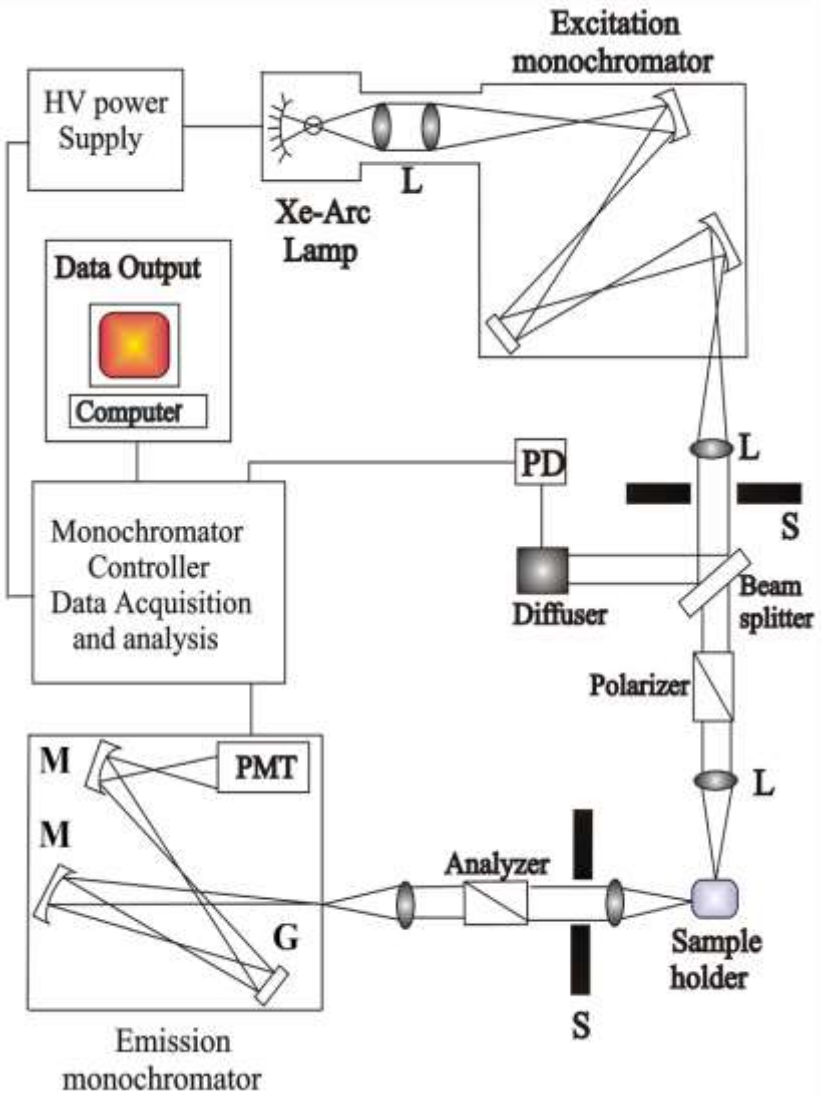


***Figure 3.2.*** *Schematic ray diagram of an emission spectrofluorometer. M, G, L, S, PMT and PD represent mirror, grating, lens, shutter, and photomultiplier tube and reference photodiode, respectively.*

**3.1.2. Time-Correlated Single Photon Counting (TCSPC) Technique:** All the picosecond-resolved fluorescence transients were recorded using TCSPC technique. The schematic block diagram of a TCSPC system is shown in Figure 3.3. TCSPC setup from Edinburgh instruments, U.K., was used during fluorescence decay acquisitions. The instrument response functions (IRFs) of the laser sources at different excitation wavelengths varied between 70 ps to 80 ps. The fluorescence from the sample was detected by a photomultiplier after dispersion through a grating monochromator [1].

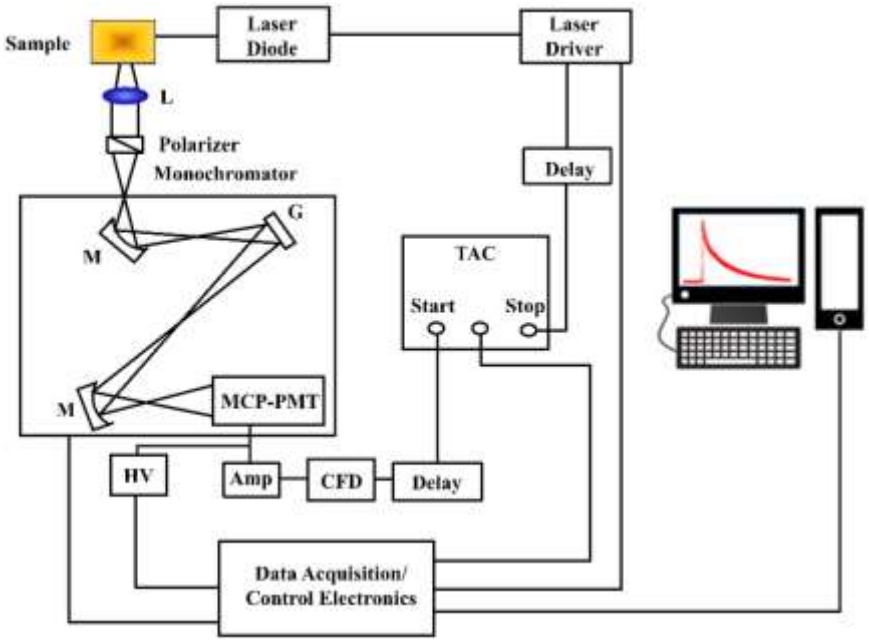


***Figure 3.3.*** *Schematic ray diagram of a time correlated single photon counting (TCSPC) spectrophotometer. A signal from microchannel plate photomultiplier tube (MCP-PMT) is amplified (Amp) and connected to start channel of time to amplitude converter (TAC) via constant fraction discriminator (CFD) and delay. The stop channel of the TAC is connected to the laser driver via a delay line. L, M, G and HV represent lens, mirror, grating and high voltage source, respectively.*

**3.1.3. Femtosecond Resolved Fluorescence Upconversion Technique:** The femtosecond-resolved fluorescence spectroscopy was carried out using a femtosecond upconversion setup (FOG 100, CDP, Figure 3.4) in which the sample was excited at 400 nm, using the second harmonic of a mode-locked Ti-sapphire laser with 80 MHz repetition rate (Tsunami, Spectra Physics), pumped by 10 W Millennia (Spectra Physics). The fundamental beam was passed through a periscopic arrangement (P) (Figure 3.4) before getting frequency doubled in a nonlinear crystal, NC1 (1 mm BBO, $\theta = 25°$, $\phi = 90°$). This beam was then sent into a rotating circular cell of 1 mm thickness containing the sample *via* a dichroic mirror (DM), a polarizer and a mirror (M6). The resulting fluorescence emission was collected, refocused with a pair of lenses (L4 and L5) and mixed with the fundamental beam (770 nm) coming through a delay line to yield an upconverted photon signal in a nonlinear crystal, NC2 (0.5 mm BBO ($\beta$-barium borate), $\theta = 10°$, $\phi = 90°$). The upconverted light was dispersed in a double monochromator and

detected using photon counting electronics. A cross-correlation function obtained using the Raman scattering from water displayed a full width at half maximum (FWHM) of 195 fs. The femtosecond fluorescence decays were fitted using a Gaussian shape for the exciting pulse.

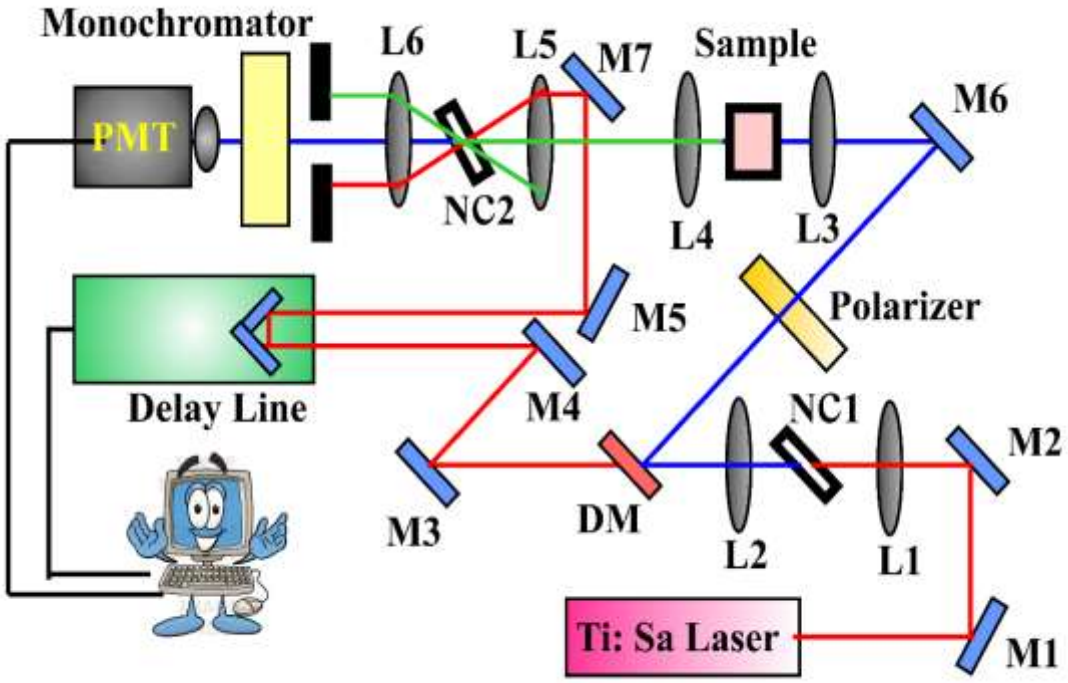


***Figure 3.4.*** *Schematic diagram of a femtosecond fluorescence upconversion experimental setup. A BBO crystal (NC1) is used for second harmonic generation, which provides a pump beam in the UV region. Another BBO crystal (NC2) generates the upconversion signal of pump and probe beams. L and M indicate lenses and mirrors, respectively. M1, M2, M3, M4, M5, and M7 are IR mirrors whereas M6 is a UV mirror. DM is dichroic mirror, and P is periscope.*

**3.1.4. Transmission Electron Microscopy (TEM):** A FEI TecnaiTF-20 field-emission high-resolution TEM (Figure 3.5) equipped with energy dispersive X-ray (EDAX) spectrometer was used to characterize the microscopic structures of samples and to analyze their elemental composition. The sizes of the nanostructures were determined from the TEM images obtained at 200 kV acceleration voltage of the microscope. Samples for TEM were prepared by placing a drop of the colloidal solution on a carbon-coated copper grid and

allowing the film to evaporate overnight at room-temperature.

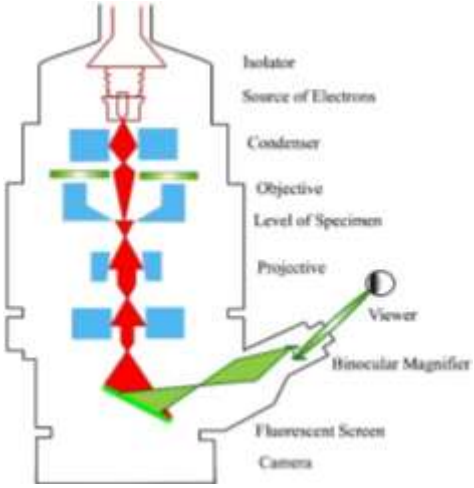


***Figure 3.5.*** *Schematic diagram of a typical transmission electron microscope (TEM). After the transmission of electron beam through a specimen, the magnified image is formed either in the fluorescent screen or can be detected by a CCD camera.*

**3.1.5. Scanning Electron Microscopy (SEM):** Surface characterization of nanomaterials were done by scanning electron microscope FE (field emission)-SEM; JEOL. Ltd., JSM-6500F. An electron-gun is attached to SEM and the electrons from filament triggered by 0 KV to 30 KV voltages. These electrons go first through a condenser lens and then through an objective lens, then through an aperture and finally reach to the specimen. The high energy electrons go a bit in the sample and back again give secondary electrons. The signal from secondary electrons are detected by detector and amplified. The ray diagram of the SEM setup is shown in Figure 3.6.

**3.1.6. Dynamic Light Scattering (DLS)**: Dynamic light scattering (DLS), also known as Photon Correlation Spectroscopy (PCS) or Quasi-Elastic Light Scattering (QELS), is one of the most popular techniques used to determine the hydrodynamic size of the particle. DLS measurements were performed on a Nano S Malvern instruments, U.K. employing a 4 mW He-Ne laser (λ= 632.8 nm) and equipped with a thermostatic sample chamber. The instrument allows DLS

measurements in which all the scattered photons are collected at 173˚ scattering angle (Figure 3.7). The instrument measures the time-dependent fluctuation in intensity of light scattered from the particles in solution at a fixed scattering angle. The ray diagram of the DLS setup is shown in Figure 3.7.

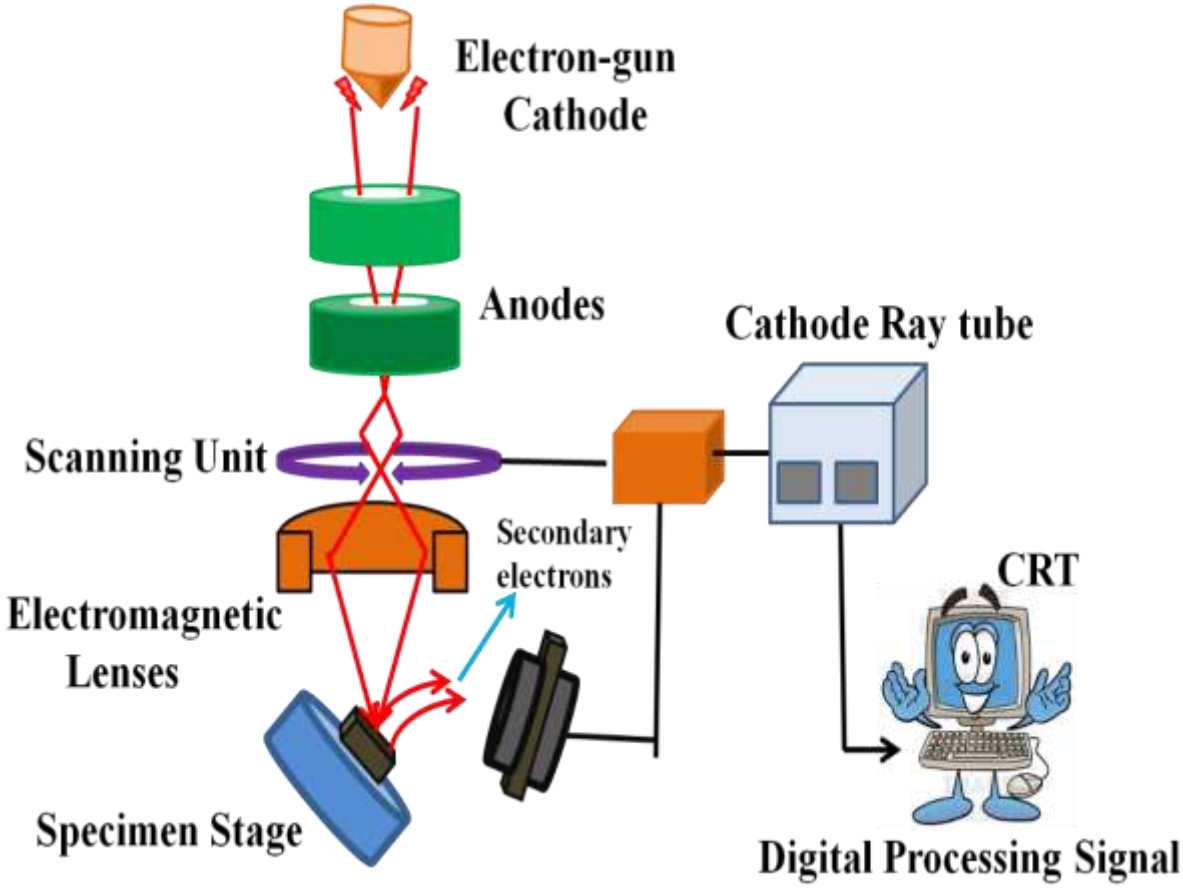


***Figure 3.6.*** *Schematic diagram of typical scanning electron microscope (SEM).*

It has been seen that particles in dispersion are in a constant, random Brownian motion and this causes the intensity of scattered light to fluctuate as a function of time. The correlator used in a DLS instrument constructs the intensity autocorrelation function G(τ) of the scattered intensity,

$$G(\tau) = \langle I(t)I(t+\tau)\rangle$$

(3.1)where τ is the time difference (the sample time) of the correlator. For a large number of monodisperse particles in Brownian motion, the correlation function

(given the symbol G) is an exponential decay function of the correlator time delay τ,

$$G(\tau) = A[1 + B\exp(-2\Gamma\tau)] \tag{3.2}$$

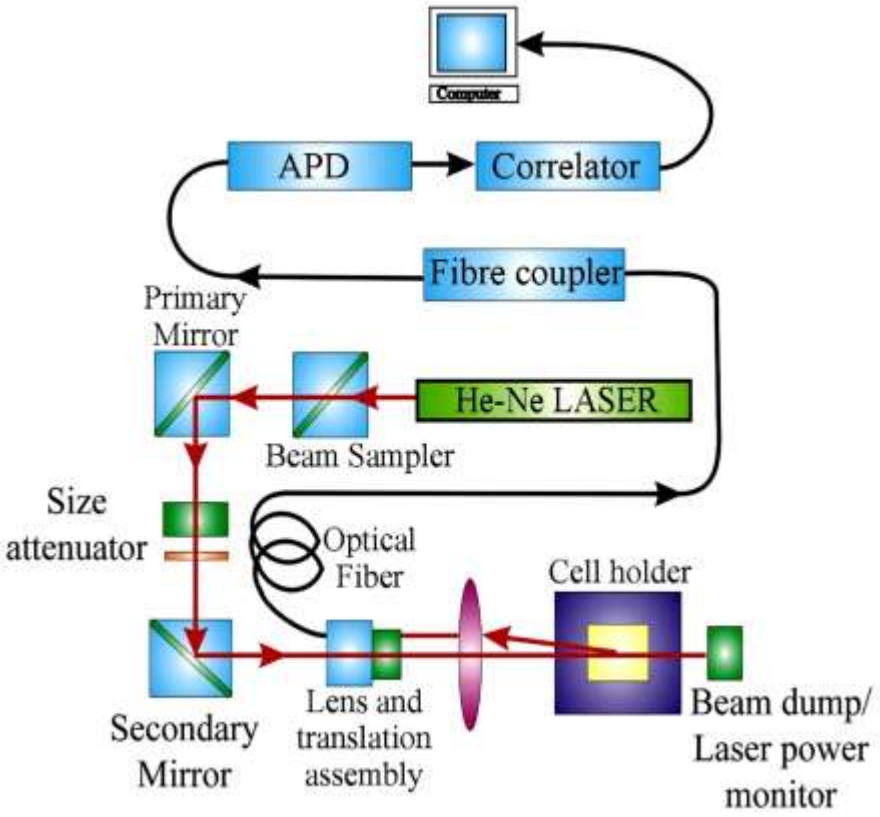


***Figure 3.7.*** *Schematic ray diagram of dynamic light scattering (DLS) instrument. The avalanche photo diode (APD) is connected to preamplifier/amplifier assembly and finally to correlator. It has to be noted that lens and translational assembly, laser power monitor, size attenuator, laser are controlled by the computer.*

where A is the baseline of the correlation function, B is the intercept of the correlation function. Γ is the first cumulant and is related to the translational diffusion coefficient as, $\Gamma = Dq^2$, where q is the scattering vector and its magnitude is defined as,

$$q = \left(\frac{4\pi n}{\lambda_0}\right)\sin\left(\frac{\theta}{2}\right) \tag{3.3}$$

where n is the refractive index of dispersant, $\lambda_0$ is the wavelength of the laser and $\theta$, the scattering angle. For polydisperse samples, the equation can be written as,

$$G(\tau) = A\left[1 + B\left|g^{(1)}(\tau)\right|^2\right] \tag{3.4}$$

where the correlation function $g^{(1)}(\tau)$ is no longer a single exponential decay and can be written as the Laplace transform of a continuous distribution $G(\Gamma)$ of decay times,

$$g^{(1)}(\tau) = \int_0^\infty G(\Gamma)\exp(-\Gamma\tau)d\Gamma \tag{3.5}$$

The scattering intensity data in DLS are processed using the instrumental software to obtain the hydrodynamic diameter ($d_H$) and the size distribution of the scatterer in each sample. In a typical size distribution graph from the DLS measurement, X-axis shows a distribution of size classes in nm, while the Y-axis shows the relative intensity of the scattered light. The diffusion coefficient (D) can be calculated using the hydrodynamic diameter ($d_H$) of the particle by using the Stoke-Einstein relation,

$$D = \frac{k_B T}{3\pi\eta d_H} \tag{3.6}$$

where $k_B$, T, $d_H$, $\eta$ are Boltzmann constant, temperature in Kelvin, hydrodynamic diameter and viscosity, respectively.

**3.1.7. X-Ray Diffraction (XRD) Measurement:** XRD is a popular and a powerful technique for determining crystal structure of crystalline materials. By examining the diffraction pattern, one can identify the crystalline phase of the material. Small angle scattering is useful for evaluating the average interparticle distance while wide-angle diffraction is useful for refining the atomic structure of nanoclusters.

The widths of the diffraction lines are closely related to strain and defect size and distribution in nanocrystals. As the size of the nanocrystals decreases, the line width is broadened due to loss of long-range order relative to the bulk. This XRD line width can be used to estimate the size of the particle by using the Debye-Scherrer formula,

$$D = \frac{0.9\lambda}{\beta \cos\theta} \tag{3.7}$$

where, $D$ is the nanocrystal diameter, $\lambda$ is the wavelength of light, $\beta$ is the full-width half-maximum (FWHM) of the peak in radians, and $\theta$ is the Bragg angle. XRD measurements were performed on a PANalytical XPERT-PRO diffractometer (Figure 3.8) equipped with CuKα radiation ($\lambda$ = 1.5418 Å at 40 mA, 40 kV). XRD patterns were obtained by employing a scanning rate of 0.02° $s^{-1}$ in the $2\theta$ range from 15° to 75°.

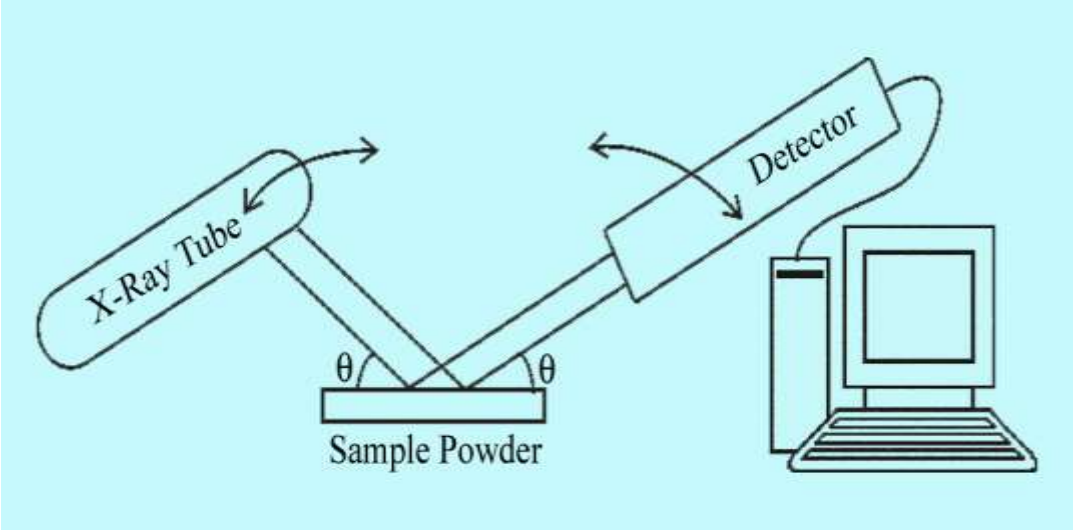


***Figure 3.8.*** *Schematic diagram of X-ray Diffraction (XRD) instrument. By varying the angle θ, the Bragg's Law conditions, nλ=2dsinθ are satisfied by different d-spacings in polycrystalline materials. Plotting the angular positions and intensities of the resultant diffracted peaks of radiation produces a pattern, which is characteristic of the sample.*

**3.1.8. Thermogravimetric-Differential Thermal Analyzer (TG-DTA) Setup:** The thermogravimetric (TG) analysis was carried out using Diamond thermogravimetric (TG)-differential thermal analyzer (DTA) from Perkin Elmer.

The TG determines the weight change of a sample whereas the DTA measures the change in temperature between a sample and the reference as a function of temperature and/or time. The schematic of the TG-DTA setup is shown in Figure 3.9. When a weight change occurs on the sample side, the beam holding the platinum pans is displaced. This movement is detected optically and the driving coil current is changed to return the displacement to zero. The detected driving coil current change is proportional to the sample weight change and the output is the TG signal. The DTA detects the temperature difference between the sample holder and the reference holder using the electromotive force of thermocouples, which are attached to the holders. This difference is measured as the DTA signal.

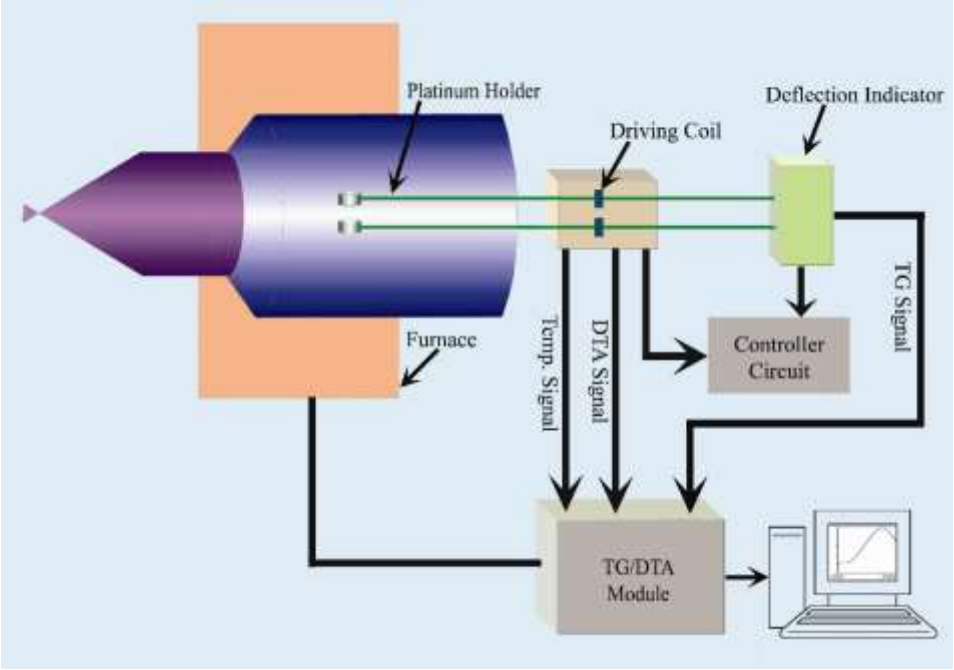


***Figure 3.9.*** *The schematic representation of TG-DTA setup.*

**3.1.9. Fourier Transform Infrared (FTIR) Measurement:** FTIR spectroscopy is a technique that can provide very useful information about functional groups in a sample. An infrared spectrum represents the fingerprint of a sample with absorption peaks which correspond to the frequencies of vibrations between the bonds of the atoms making up the material. Because each different material is a unique combination of atoms, no two compounds produce the exact same infrared

spectrum. Therefore, infrared spectroscopy can result in a positive identification (qualitative analysis) of every different kind of material. In addition, the size of the peaks in the spectrum is a direct indication of the amount of material present. The two-beam Michelson interferometer is the heart of FTIR spectrometer. It consists of a fixed mirror (M4), a moving mirror (M5) and a beam-splitter (BS1), as illustrated in Figure 3.10. The beam-splitter is a laminate material that reflects and transmits light equally. The collimated IR beam from the source is partially transmitted to the moving mirror and partially reflected to the fixed mirror by the beam-splitter. The two IR beams are then reflected back to the beam-splitter by the mirrors. The detector then sees the transmitted beam from the fixed mirror and reflected beam from the moving mirror, simultaneously. The two combined beams interfere constructively or destructively depending on the wavelength of the light (or frequency in wavenumbers) and the optical path difference introduced by the moving mirror. The resulting signal is called an interferogram which has the unique property that every data point (a function of the moving mirror position) which makes up the signal has information about every infrared frequency which comes from the source. Because the analyst requires a frequency spectrum (a plot of the intensity at each individual frequency) in order to make identification, the measured interferogram signal cannot be interpreted directly. A means of "decoding" the individual frequencies is required. This can be accomplished *via* a well-known mathematical technique called the Fourier transformation. This transformation is performed by the computer which then presents the user with the desired spectral information for analysis. FTIR measurements were performed on a JASCO FTIR-6300 spectrometer (transmission mode). For the FTIR measurements, powdered samples were mixed with KBr powder and pelletized. The background correction was made using a reference blank of KBr pellet.

**3.1.10. Fluorescence Microscope:** Commercially available fluorescence microscope (Leica digital inverted microscopes DMI8.) was used in our study. The light source

is usually a mercury-vapor lamp. For bright field, Tungsten-halogen lamp was used. In particular, an inverted setup with a mercury-vapor lamp as light source is shown in Figure 3.11.

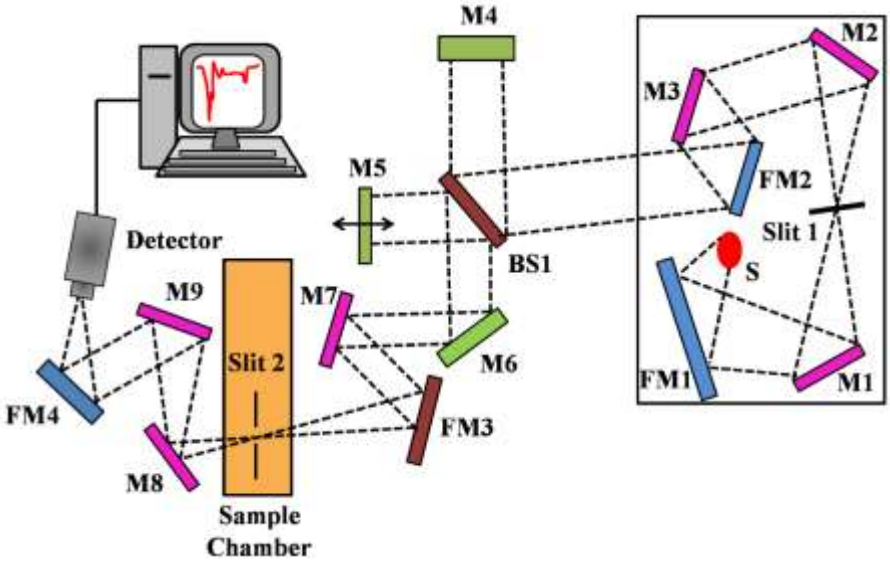


***Figure 3.10.*** *Schematic of Fourier Transform Infrared (FTIR) spectrometer. It is basically a Michelson interferometer in which one of the two fully-reflecting mirrors is movable, allowing a variable delay (in the travel-time of the light) to be included in one of the beams. M, FM and BS1 represent the mirror, focussing mirror and beam splitter, respectively. M5 is a moving mirror.*

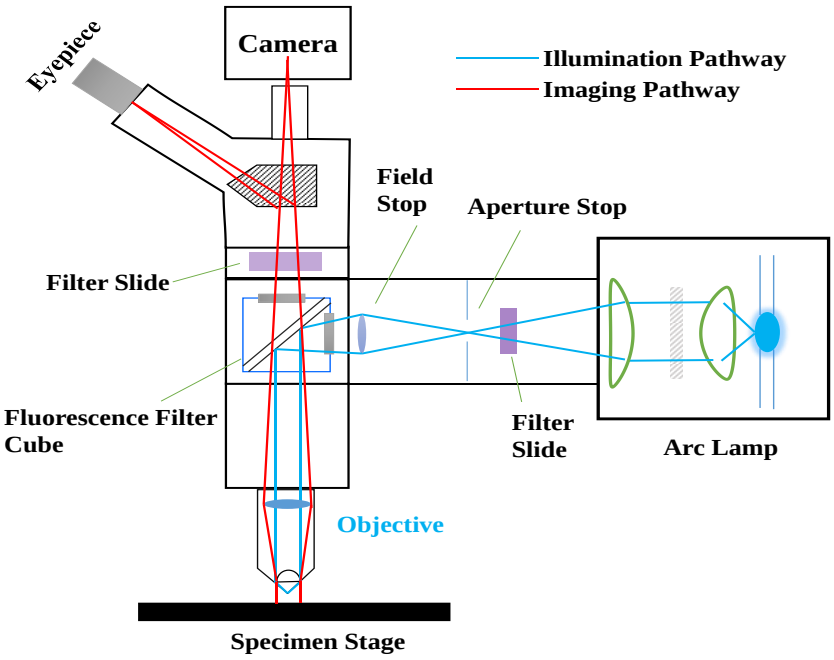


***Figure 3.11.*** *Schematic presentation of the fluorescence microscope.*

The dichroic mirror, excitation and emission filter are joined together within the filter cube (Figure 3.11). Due to the Stokes shift, it is possible to separate excitation and emission light in the same light path optically *via* a dichroic mirror. This way, only the emission light is collected by the objective. An emission filter helps to suppress unwanted background light.

**3.1.11. Light Source Used for Irradiation**: For red light activated experiments, a red light-emitting diode (LED) source ($\lambda_{max}$ = 640 nm, 409 nm and power = 3 mW/cm$^2$) was used. A UV light source (LED) of 390 nm – 400 nm was used to irradiate samples under UV-blue light source.

**3.2. Sample Preparation:** In this section the different sample preparation methods have been discussed.

**3.2.1. Chemicals Used:** The chemicals and spectroscopic probes were procured from the following sources. Analytical-grade chemicals were used for synthesis without further purification. Deionized (DI) water, obtained from Millipore, was used to prepare all aqueous solutions. The probes dichloro-fuorescin diacetate (Calbiochem), singlet oxygen sensor green (Sigma Aldrich) and the dyes IR820 (Sigma Aldrich), ICG (Sigma Aldrich), Riboflavin (Sigma Aldrich), were used without any further purification. ZnO NPs (~ 30 nm) was purchased from Sigma Aldrich. Manganese acetate ($C_4H_6MnO_4$), hydrazine ($H_4N_2$), ammonium chloride ($NH_4Cl$), thioacetamide ($C_2H_5NS$) and ethylenediaminetetraaceticacid (EDTA) were purchased from Sigma Aldrich. Chloroauric acid [$HAuCl_4$. $H_2O$]were purchased from Sigma. Dimethyl sulfoxide (DMSO) was purchased from Merck. Sodium azide ($NaN_3$) and t-butyl alcohol (TBA) were obtained from Sigma-Aldrich.

**3.2.2. Synthesis of IR820-ZnO Nanohybrid:** The surface of ZnO NPs were functionalised by IR820 dye by adding 12 mg of ZnO NPs into 10 ml of IR820 solution (1 μM solution in DMSO) with continuous stirring at room temperature,

for 12 h. After 12 h, the solution was centrifuged for 25 min and the clear supernatants containing the free dyes were discarded. Then, the nanohybrids were washed with DMSO for three times to remove free dyes. After washing, the nanohybrid was dried in the oven for 5 hr under 150 $^{o}$C.

**3.2.3. Synthesis of ICG-ZnO Nanohybrid:** ICG-ZnO nanohybrid was synthesized by adding 12 mg of ZnO NPs into 10 ml of ICG solution (1 μM solution in DMSO) followed by continuous stirring at room temperature, for 12 h. After 12 h, the solution was centrifuged for 25 min and washed with DMSO three times to remove any free dyes. The nanohybrid was then dried in the oven for 4 hr at 150 $^{o}$C.

**3.2.4. Synthesis of Rf-ZnO Nanohybrids:** Rf-ZnO nanohybrid was synthesized by addition of ZnO NPs (10 mg) into 10 ml of Rf solution (0.5 mM solution in ethanol) under magnetic stirrer at room temperature, for 12 h. After that, the solution was centrifuged for 30 min and washed with ethanol four times to wash out free dyes. The nanohybrid was then dried in the oven for 4 hr at 70 $^{o}$C.

**3.2.5. Synthesis of Au-ZnO Nanohybrid:** 12 mg of ZnO NPs was slowly added to the 5 ml of 1 mM aqueous solution of chloroauric acid [$HAuCl_4. H_2O$] under continuous stirring for 15 minutes at room temperature. Then aqueous solution of 5 mM of sodium borohydride ($NaBH_4$) was added drop-wise to the solution for the reduction of the gold chloride to Au NPs. Immediately the solution turns red from pale yellow colour indicating the decoration of the Au NPs on the surface of ZnO NPs.

**3.2.6. Synthesis of Rf-ZnO-Au Nanohybrid:** The Rf-ZnO-Au nanohybrid was synthesized upon addition of 10 mg of Au-ZnO nanohybrid into 10 ml of Rf solution (0.5 mM solution in ethanol) at room temperature under continuous stirring for 14 h. The solution was then centrifuged for 20 min and washed with

ethanol four times to remove any free Rf. The synthesized Rf-ZnO-Au nanohybrid was then dried in the oven for 4 hr at 70 $^{o}$C.

**3.2.7. Synthesis Rf-$Al_2O_3$-Au Nanohybrid:** Rf-$Al_2O_3$-Au nanohybrid was synthesized by adding 10 mg of synthesized $Al_2O_3$-Rf nanohybrid (simler with Rf-ZnO) to the Rf solution in ethanol (0.5 mM) followed by continuous stirring at room temperature for 14 h. The solution was then centrifuged for 30 min and the prepared Rf-$Al_2O_3$-Au nanohybrid was dried in the oven for 4 hr at 70 $^{o}$C.

**3.2.8. Synthesis of Bulk MnS NPs:** For the synthesis of MnS NPs, manganese acetate ($C_4H_6MnO_4$) is the source for manganese ($Mn^{2+}$) ions, thioacetamide ($C_2H_5NS$) was used as a source for sulfide ($S^{-2}$) ions, ethylenediaminetetraaceticacid (EDTA) was used as a capping agent, ammonium chloride ($NH_4Cl$) was utilized to maintain the pH of the solution and hydrazine ($H_4N_2$) was used as a reducing agent. At first, 5 ml of 2 M ethylenediaminetetraaceticacid (EDTA) solution was added to 10 ml of 1 M manganese acetate ($C_4H_6MnO_4$) solution in a 100 ml glass beaker and then the mixture was stirred for 5 minutes. After that, 10 ml of 1.4 M $NH_4Cl$ was added and stirred the mixture for 10 minutes. Then, 0.2 ml of hydrazine ($H_4N_2$) was added into the solution in the beaker and stirring was continued for 10 minutes. Finally 10 ml of 1 M thioacetamide ($C_2H_5NS$) solution was added to the solution and stirred for 15 minutes. Immediately, the solution turns pink because of formulation of pink particles. The pink particles were separated through filtration. The filtered particles were washed in multiple times with absolute methanol and double distilled water. The particles were then dried in oven at 70 $^{o}$C for 3 hrs.

**3.2.9. Functionalization of As-Prepared MnS NPs by Citrate Ligand:** At first, we have prepared 10 ml of 0.5 M sodium citrate solutions in Millipore water. After that, we have added 152 mg of as-prepared MnS NPs under magnetic stirring for 12 hours. Finally, a syringe filter of 0.22 μm diameter was used to filtered out the

non-functionalized NPs and the resulting filtered solutions is pure citrate capped MnS NPs.

**3.2.9. Functionalization of ZnO NPs by Citrate and Humic acid (HA):** 100 mg ZnO and 1.5 g sodium citrate were mixed with 10 ml DI water and the mixture was vortexed overnight. The resultant opaque solution was centrifuged and washed several times using DI water. The excess citrate was removed by dialysis method using the buffered media as the bulk solution for diffusion of citrate. Two different buffer solutions were used, namely, acetate (pH 5), phosphate (pH 7.4) and alkaline glycine buffer (pH 12). Specifically, 10 mg HA was added in 10 ml water and stirred for 24 hours in dark condition. The solution was centrifuged to separate the particulate matter and pH was adjusted to 6.5 using diluted HCl. Surface functionalization with HA was achieved by mixing 50 mg ZnO with 10 ml 0.1 $gL^{-1}$ HA solutions and shaking for 48 hours in dark condition. The nanoparticles were centrifuged (3500 rpm), washed 5 times using Milli-Q water, re-suspended in 10 ml water and stored in refrigerator until further use.

**3.2.10. Preparation of Dichlorofluorescein and ROS Measurements:** DCFH was prepared from DCFH-DA (dichlorofluorescin diacetate obtained from Calbiochem) by mixing 0.5 mL of 1.0 mM DCFH-DA in methanol with 2.0 mL of 0.01 N NaOH. This deesterification of DCFH-DA proceeded at room temperature for 30 min and the mixture was then neutralized with 10 mL of 25 mM $NaH_2PO_4$, pH 7.4. This solution was kept on ice in the dark until use. All the measurements were performed in a total volume of 2.0 mL water that contained 10 µL of DCFH solution, dye, ZnO dye-ZnO and dye-ZnO-Au (individual concentrations of dye and ZnO in the nanohybrid are same).

**3.2.11. Bacterial Strain and Culture Conditions:** The strain of *E. coli* was used for the bacteriological assays for the treatment of ICG-ZnO nanohybrid. The cells were incubated with 0.3 mg/ml nanohybrids (concentration of ICG is used on the

basis of ICG loading on ZnO surface) for 3 hrs and the red-light illumination ($\lambda_{max}$ = 640 nm) time was 30 min. Luria−Bertani (LB) agar-based colony formation assay was used to measure photodynamic action. The strain of methicillin-resistant *S. aureus* (MRSA) was used for the another bacteriological assay. The MRSA cells were incubated with 0.20 mg/ml Rf-ZnO-Au nanohybrid, Rf-ZnO nanohybrid and others control (the concentration of Rf was used on the basis of Rf loading on ZnO surface and the concentration of ZnO and Au-ZnO were equivalent with the concentration presence in the Rf-ZnO-Au nanohybrid) for 3 hrs. The experiments were performed in absence as well as presence of blue-light ($\lambda_{max}$ = 409 nm) for 30 min. The colony forming unit (CFU) of *S. aureus* were counted to quantify the antibacterial activity. The antimicrobial activity of citrate-MnS was checked against *S. hominis* bacteria. *S. hominis* were cultured in Luria−Bertani (LB) medium under an incubator shaker of temperature at 37 °C for 24 h. The experiments were performed by the colony forming unit (CFU) assays method. The cells were incubated with 10 μL as-prepared citrate-MnS NPs at pH 5 and pH 8 separately for 3 hrs without any photo-activation. Then cultures were uniformly spread on LB agar plates and the plates were incubated at 37 °C for 24 h to get the CFU.

**3.2.12. Hemolysis Assay:** The hemolysis assay was performed on human RBCs. Ethylenediaminetetraacetate stabilized human whole blood was centrifuged five times and redispersed in 10 mL of phosphate-buffered saline (PBS) buffer. Then, 0.1 mL of RBC solution was mixed with variable concentrations of nanohybrids [16]. The samples were incubated at 37 °C and 100 rpm for 30 min, and then the mixture was centrifuged at 5000 rpm for 5 min. The absorption of the supernatant solution was measured at 570 nm. RBCs incubated with PBS and 1% Triton X-100 were used as negative and positive controls, respectively. All sets were prepared in triplicate. The hemolysis percentage was calculated following the reported equation.

# References

[1] D. O'Connor, Time-correlated single photon counting, *Academic Press* 2012.

[2] S. Wanninger, V. Lorenz, A. Subhan, F.T. Edelmann, Metal complexes of curcumin–synthetic strategies, structures and medicinal applications, *Chem. Soc. Rev.* 44 (2015) 4986.

[3] D. Bagchi, S. Chaudhuri, S. Sardar, S. Choudhury, N. Polley, P. Lemmens, S.K. Pal, Modulation of stability and functionality of a phyto-antioxidant by weakly interacting metal ions: Curcumin in aqueous solution, *RSC Adv.* 5 (2015) 102516.

[4] A. Schejn, A. Aboulaich, L. Balan, V. Falk, J. Lalevée, G. Medjahdi, L. Aranda, K. Mozet, R. Schneider, $Cu^{2+}$-doped zeolitic imidazolate frameworks (ZIF-8): Efficient and stable catalysts for cycloadditions and condensation reactions, *Catal. Sci. Technol.* 5 (2015) 1829.

[5] J. Cravillon, S. Mu¨nzer, S.J. Lohmeier, A. Feldhoff, K. Huber, M. Wiebcke, Rapid room-temperature synthesis and characterization of nanocrystals of a prototypical zeolitic imidazolate framework, *Chem. Mater.* 21 (2009) 1410.

[6] S. Baruah, J. Dutta, pH-dependent growth of zinc oxide nanorods, *J. Cryst. Growth.* 311 (2009) 2549.

[7] S. Baruah, J. Dutta, Effect of seeded substrates on hydrothermally grown ZnO nanorods, *J. Sol-Gel Sci. Technol.* 50 (2009) 456.

[8] D. Bagchi, T.K. Maji, S. Sardar, P. Lemmens, C. Bhattacharya, D. Karmakar, S.K. Pal, Sensitized ZnO nanorod assemblies to detect heavy metal contaminated phytomedicines: Spectroscopic and simulation studies, *Phys. Chem. Chem. Phys.* 19 (2017) 2503.

[9] H. Dürr, Perspectives in photochromism: A novel system based on the 1, 5-electrocyclization of heteroanalogous pentadienyl anions, *Angew. Chem.* 28 (1989) 413.

[10] T.B. Shrestha, J. Melin, Y. Liu, O. Dolgounitcheva, V.G. Zakrzewski, M.R. Pokhrel, E. Gogritchiani, J.V. Ortiz, C. Turró, S.H. Bossmann, New insights in the

photochromic spiro-dihydroindolizine/betaine-system, *Photochem. Photobiol. Sci.* 7 (2008) 1449.

[11] D. Banerjee, S.K. Srivastava, S.K. Pal, Spectroscopic studies on ligand−enzyme interactions: Complexation of α-chymotrypsin with 4,6-diamidino-2-phenylindole (DAPI), *J. Phys. Chem. B* 112 (2008) 1828.

[12] K.S. Park, Z. Ni, A.P. Côté, J.Y. Choi, R. Huang, F.J. Uribe-Romo, H.K. Chae, M. O'Keeffe, O.M. Yaghi, Exceptional chemical and thermal stability of zeolitic imidazolate frameworks, *Proc. Natl. Acad. Sci. U.S.A.* 103 (2006) 10186.

[13] S. Chaudhuri, S. Sardar, D. Bagchi, S. Dutta, S. Debnath, P. Saha, P. Lemmens, S.K. Pal, Photoinduced dynamics and toxicity of a cancer drug in proximity of inorganic nanoparticles under visible light, *ChemPhysChem* 17 (2016) 270.

[14] D. Bagchi, S. Dutta, P. Singh, S. Chaudhuri, S.K. Pal, Essential dynamics of an effective phototherapeutic drug in a nanoscopic delivery vehicle: Psoralen in ethosomes for biofilm treatment, *ACS Omega* 2 (2017) 1850.

[15] T.L. Riss, R.A. Moravec, A.L. Niles, S. Duellman, H.A. Benink, T.J. Worzella, L. Minor, Cell viability assays, *Eli Lilly & Company and the National Center for Advancing Translational Sciences* 2016.

[16] B. Duncan, X. Li, R.F. Landis, S.T. Kim, A. Gupta, L.-S. Wang, R. Ramanathan, R. Tang, J.A. Boerth, V.M. Rotello, Nanoparticle-stabilized capsules for the treatment of bacterial biofilms, *ACS Nano* 9 (2015) 7775.

[17] M.F. Sanner, Python: A programming language for software integration and development, *J. Mol. Graph. Model* 17 (1999) 57.

[18] S. Grimme, Semiempirical GGA-type density functional constructed with a long-range dispersion correction, *J. Comput. Chem.* 27 (2006) 1787.

# Chapter 4

# Spectroscopic Studies on NIR Active Nanohybrids for Potential Enhaced Biological Activity

**4.1. Introduction:** Light harvesting materials that capture solar photons and convert them for light mediated applications are considered to be one of the ground breaking research topics of the present day. Light harvesting assemblies provide wide range of applications as in dye sensitized solar cells, photodynamic therapy (PDT), photocatalysis, bio-imaging, hydrogen evolution, toxic elements sensing etc. [1]. Moreover, near infrared (NIR) light harvesting from solar spectrum is particularly significant for photocatalysis, bio-imaging and photodynamic therapy [2, 3]. NIR (range from 650 to 1350 nm) radiation is more promising for photodynamic therapy because of its large penetration depth in tissue [4]. Light harvesting systems can be classified into organic dyes, metal-ligand complexes, inorganic semiconductors, quantum dots, organic-inorganic nanohybrids, bio-molecular assemblies etc. [5, 6]. $TiO_2$ and ZnO are the most promising semiconductors which have been used in different way of light harvesting for many years [7, 8]. Among the long list of light harvesting materials, dyes are the most widely used system to date. Basically, dyes are less toxic than inorganic materials and they are capable of efficient light harvesting as they have very high molar extinction co-efficient. Many NIR dyes have been used as therapeutics because of their photodynamic action, photo thermal effect and suitable efficiency of singlet oxygen generation that can kill infected cells [9, 10]. Recently, in case of dye sensitized solar cells (DSSC) also, there is a growing interest in NIR sensitization [11, 12]. Also, some dyes have been used in photocatalytic hydrogen evolution and organic pollutant degradation [13].

In the last few years, cyanine dyes have been one of the most important NIR dye for DSSC and PDT applications [14, 15]. Some reports on their photocatalytic activity are also present [16]. They show different photo-physical properties depending on their

various structures [17]. One of the disabilities of these NIR dyes is poor photostability under NIR radiation [18, 19]. The photostability of cyanine dyes is not suitable for their potential use. The photobleaching pathway of cyanine dyes is initiated by their first triplet excited ($T_1$) state. Upon photon absorption, electrons transit from ground state ($S_0$) to first singlet excited ($S_1$) state. Besides fluorescence mediated relaxation, electrons can shift to $T_1$ state through intersystem crossing (ISC). This long lived $T_1$ state is quenched by molecular oxygen to generate singlet oxygen [20]. Basically, production of efficient singlet oxygen [21, 22] by cyanine dyes leads to oxidation of the dye ($^1O_2$, being low lying LUMO is a very strong oxidising agent [23-25]) that is responsible for its photo-degradation [20, 26]. Moreover, cyanine dyes contains exo-cyclic C-C double bonds. The singlet oxygen causes 1, 4-addition reaction to cis-diene or 1, 2-addition reaction to alkene to form a dioxene structure or 1, 2-dioxitane structure respectively [27]. Therefore, improvement of photostability is required for potential application of cyanine dyes. Besides low photostability, thermal degradation of cyanine dyes has been considered an issue for its real applications [28].

To solve the problem of low photostability of these cyanine dyes, few methods have been reported including encapsulation in the negatively charged copolymer [19], non-covalent encapsulation inside silica nanoparticles [29] or doping with silica nanoparticles [30] and cucurbituril encapsulation [31]. Another efficient strategy to improve the photostability of cyanine dye is the introduction of some electron deficient substituent, which can reduce the reactivity of dye towards singlet oxygen [20, 26, 32]. The most general way for the enhancement of photostability is conjugation with triplet state quencher such as cyclooctatetraene (COT) [33]. However, to employ all these methods complicated expensive synthetic strategies are required.

In our present study, we report a new approach that focuses on the photostability of a very well-known cyanine dye IR820. IR820 has been widely used in photodynamic therapy because of its ability of singlet oxygen generation [21] under NIR radiation. It has been used in near infrared room temperature photovoltaic photon detectors

[34] and to enhance up-conversion luminescence [35, 36]. Also, like other cyanine dyes, it has an issue of photobleaching [37]. We have chosen semiconductor zinc oxide nanoparticles (ZnO NPs, band gap ~3.3 eV) and developed IR820 functionalised nanohybrid IR820-ZnO. We specifically select ZnO NPs due to their biocompatibility, low cost and ease of synthesis [38]. IR820 dye has been attached on ZnO surface, which has been confirmed by optical spectroscopy tools. We have explored a significant enhancement of photostability of IR820 dye on ZnO surface as compared to free IR820. We have monitored the generation of ROS (reactive oxygen species) under red light using DCFH (dichlorofluorescin) indicator. The rate of ROS generation is enhanced for IR820-ZnO as compared to that of IR820. To study the nature of ROS, we have performed SOSGR (singlet oxygen sensor green reagent) assay for singlet oxygen detection and luminol chemiluminescence for superoxide detection. We have also explored the photoinduced excited-state electron transfer process from dye to ZnO in the nanohybrid under red light excitation, which can result from the molecular-level interaction between two moieties. A singlet oxygen quencher ($NaN_3$) was used to analyze the singlet oxygen mediated photodegradation of IR820 dye and its improvement of photostability on the surface of ZnO. In order to check the thermal stability of IR820-ZnO nanohybrid, we have done thermogravimetric analysis (TGA) of IR820-ZnO, IR820 and ZnO. Furthermore, we have checked pH responsive dissolution and precipitation of nanohybrid to verify the capability of potential biological application. Overall, our present study is an attempt for the improvement of photostability and activity of NIR cyanine dye.

## 4.2. Results and Discussion:

**4.2.1. Improvement of Photostability and NIR Activity of Cyanine Dye Through Nanohybrid Formation: Key Information From Ultrafast Dynamical Studies [39]:** High-resolution transmission electron microscopic image of ZnO nanoparticles is depicted in Figure 4.1.a. An interplanar distance of 0.28 nm has been observed from the lattice fringes of ZnO nanoparticles, which corresponds to the (100) crystal planes [40]. The average diameter of ZnO nanoparticles is ~20 nm. Figure 4.1.b

represents the chemical structure of IR820 dye. Figure 4.1.c schematically represents the formation of the IR820-ZnO nanohybrid. The conjugation between IR820 dye and defect sites of ZnO crystal leads to formation of nanohybrid. To check the crystal structural stability of the nanohybrid, we have performed the XRD analysis. Figure 4.1.d delineates the characteristic X-ray diffraction of ZnO nanoparticles (pink) and IR820-ZnO nanohybrid (blue). The diffraction pattern of ZnO depicts wurtzite [41] crystal structure that remains unaltered after conjugation with IR820 dye. Thus, we infer that the crystal structure of ZnO remains intact upon functionalization with IR820. Figure 4.2.a represents the absorption spectra of IR820 dye and IR820-ZnO nanohybrids in methanol.

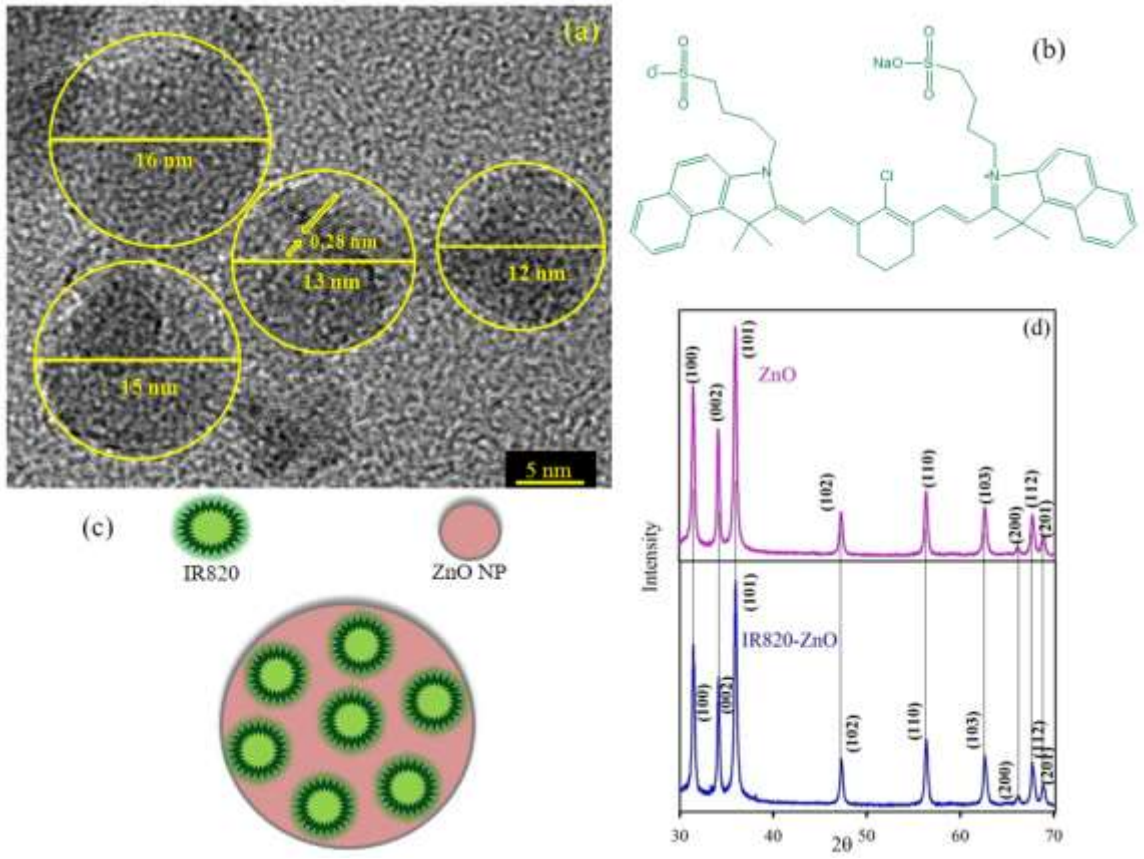


***Figure 4.1.*** *(a) HRTEM image of ZnO nanoparticles. (b) Structure of IR820. (c) Scheme of formation of IR820-ZnO nanohybrid. (d) Powder XRD pattern of ZnO and IR820-ZnO nanohybrid.*

The characteristic peak of IR820 is observed at 820 nm with a shoulder at 752 nm. The main peak at 820 nm corresponds to the 0→0 transition with a shoulder at 752 nm due to the 0→1 vibronic sub-band [42, 43]. In case of IR820-ZnO nanohybrids,

the characteristic peaks of both IR820 and ZnO are observed. However, no significant shift of absorption maxima of IR820 is observed in the nanohybrid. To check the solvent dependent absorption characteristics of IR820 dye, we have checked absorbance of IR820 in water in a concentration dependent manner.

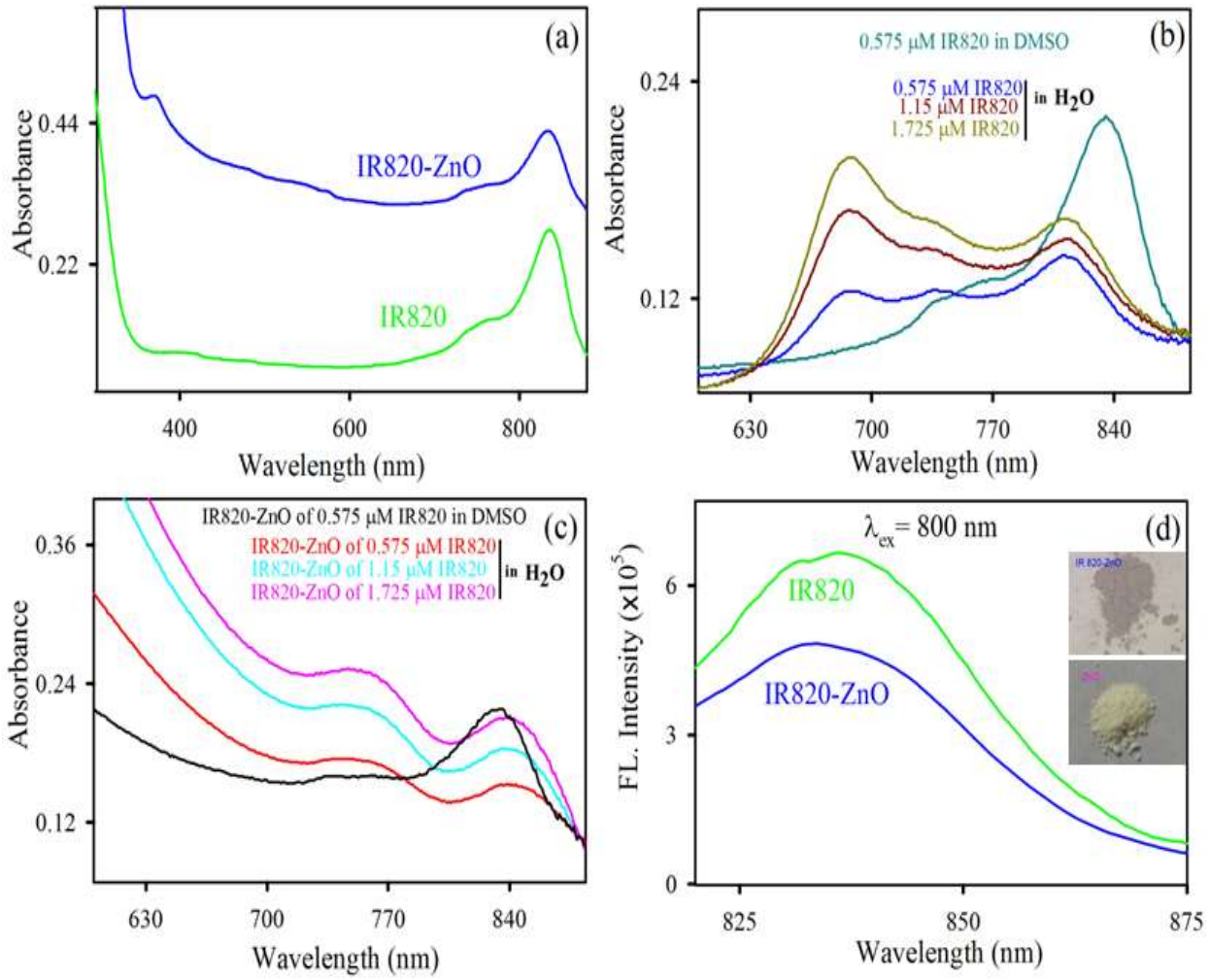


***Figure 4.2.*** *(a) UV-VIS absorption spectra of IR820 and IR820-ZnO nanohybrid in methanol. (b) The absorption spectra of IR820 in $H_2O$ at different concentration. (c) The absorption spectra of IR820-ZnO in $H_2O$ at different concentration. (d) Room temperature emission spectra of IR820 and IR820-ZnO in methanol. Inset shows photographs of ZnO and IR820-ZnO.*

As shown in Figure 4.2.b, an extra peak at 686 nm is observed in the presence of water and it enhances upon increase in concentration of IR820 in $H_2O$. This peak inversion indicates H-aggregation and the peak at 686 nm represents the higher order H-aggregation form of IR820 [44]. The H-aggregation of IR820 in water is restricted on ZnO surface when concentration is increased. The extra peak at 686 nm (which designates the H-aggregation of the dye) of IR820 in water is not clearly observed in the nanohybrid at the same concentration of IR820 (Figure 4.2.c). The

attachment of dye on ZnO surface enhances the rigidity of IR820 dye, which might be responsible to protect the dye structure from H-aggregation [45]. There is a visible colour change after functionalization of ZnO, as shown in the inset of Figure 4.2.d that depicts the colour of ZnO nanoparticles changes from white to grey upon dye attachment. In steady state emission spectra (Figure 4.2.d), the peak near 834 nm is clearly observed for both dye and nanohybrid ($\lambda_{ex}$ = 800 nm) in methanol. The significant quenching in emission intensity for IR820-ZnO nanohybrid indicates the presence of excited state non-radiative process.

After optical characterization, we have studied the thermal stability of the nanohybrid by TGA. Figure 4.3.a depicts the TG curves of IR820, ZnO and IR820-ZnO. The weight loss of IR820 dye within 30-700 $^{o}$C is approximately 58% and the pure ZnO NPs shows negligible degradation within this temperature range. IR820-ZnO nanohybrid shows negligible weight loss within the range of 30-700 $^{o}$C of approximately 5%. As, the IR820 dye has melting point greater than 300 $^{o}$C, the maximum weight loss of IR820 is observed within the range of 300-500 $^{o}$C. Hence, the mass loss of the nanohybrid as compared to that of ZnO within 375-500 $^{o}$C implies the presence of IR820 dye. This analysis shows that IR820 retains thermal stability at temperature range 30-700 $^{o}$C after the formation of the nanohybrid. Further, we have checked the photo-stability of the dye upon hybrid formation. Figure 4.3.b represents the time dependent photodegradation of IR820 and IR820-ZnO nanohybrid. The experiment was performed in DMSO under red light and the change in absorption peak of IR820 at 834 nm is monitored with variable time window. The rate of degradation of IR820 is higher as compared to that of IR820-ZnO nanohybrid under red light irradiation. We have estimated the degradation percentage to be 26.5% in the case of IR820 and 15.8% for nanohybrid after 20 minutes of experimental time window.

After evaluating the improvement in the thermal stability and photo stability of IR820 dye upon hybrid formation using ZnO NPs, we illustrate *in vitro* photo-induced ROS generation using well-known marker DCFH. DCFH is oxidised to fluorescent DCF in presence of ROS and exhibits a strong emission near 522 nm

upon 488 nm excitation [38]. Thus, the enhancement of emission intensity at 522 nm signifies presence of greater ROS level. The experiment was done under dark for 10 minutes and under irradiation of red light for 30 minutes. In dark, there is no change in emission intensity at 522 nm.

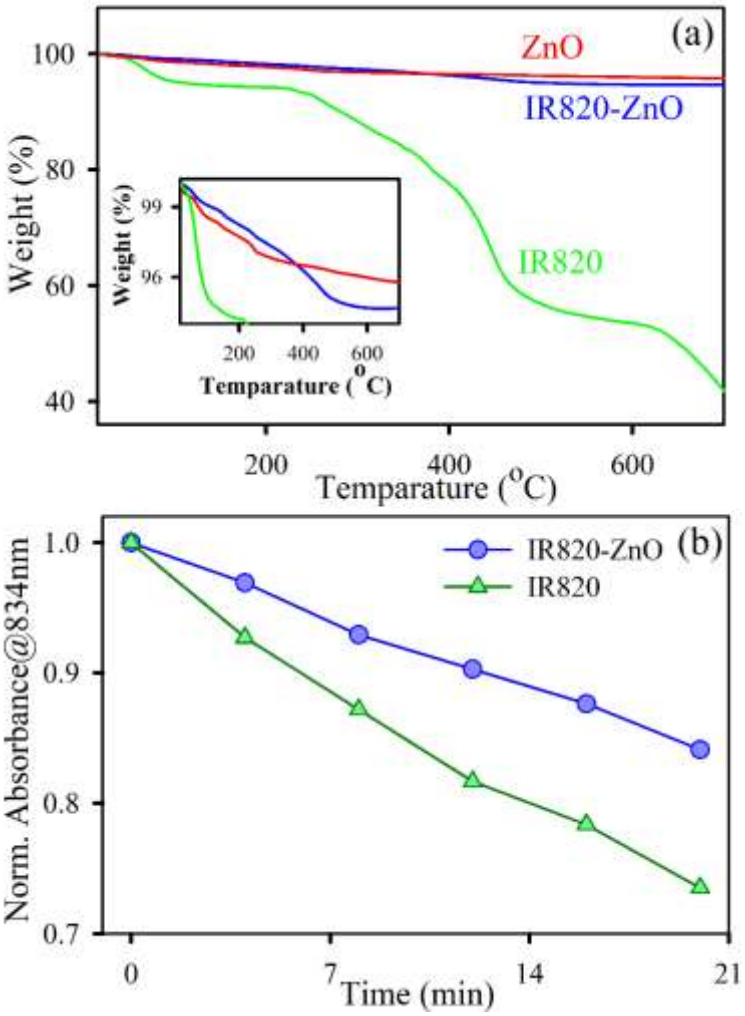


***Figure 4.3.*** *(a) TGA profile of IR820, IR820-ZnO and ZnO. Inset shows the enlarge graph of IR820-ZnO and ZnO degradation. (b) Time dependent photodegradation of IR820-ZnO and IR820.*

This suggests no activity of the nanohybrid under dark condition. With increase in light exposure time, the greater enhancement of emission intensity (@522 nm) was observed for IR820-ZnO as compared to that of IR820 and ZnO. Thus, the red light triggers the efficient generation of ROS for IR820-ZnO nanohybrid (Figure 4.4.a). The trend suggests improved applicability of nanohybrid compared to dye systems. To investigate the nature of generated ROS, we have further done SOSGR assay for

singlet oxygen detection and luminol chemiluminescence reaction for super oxide detection.

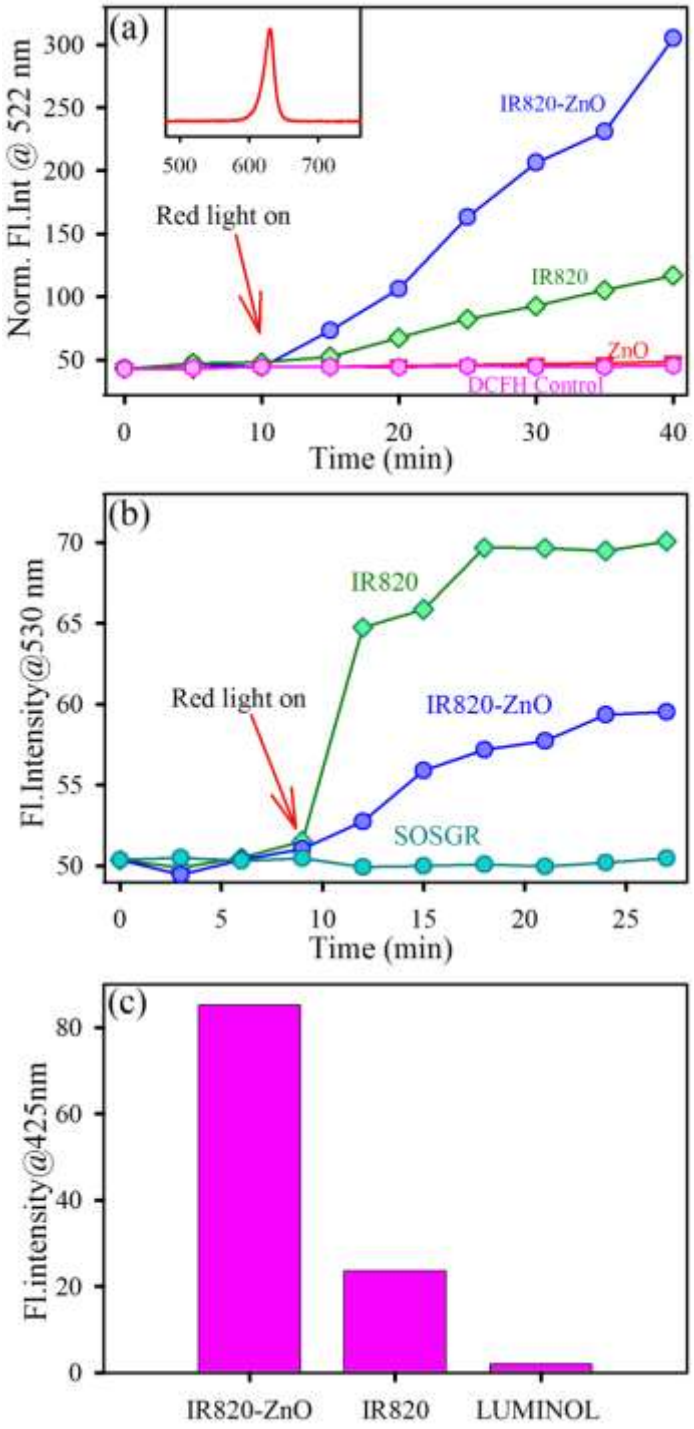


***Figure 4.4.*** *(a) DCFH oxidation (monitored at 522 nm) with time in presence of IR820-ZnO, IR820, ZnO and DCFH only under dark (10 min) and red light (30 min). Inset shows the spectra of red LED. (b) The kinetics of SOSGR (monitored at 530 nm) oxidation in presence of IR820-ZnO, IR820 and SOSGR only under dark (9 min) and red light (18 min). (c) Chemiluminescence of luminol after red light irradiation for 15 minutes in the presence of IR820-ZnO, IR820 and control luminol only.*

Singlet oxygen sensor green reagent (SOSGR) is a well-known singlet oxygen marker which is selectively oxidised by singlet oxygen and converted to SOSGR endoperoxide (SOSGR-EP). SOSGR-EP provides green fluorescence in the range of 525-536 nm [38]. The enhancement of singlet oxygen during our experiment was monitored at 530 nm. After red light illumination for 18 minutes, greater enhancement of emission intensity (@530 nm) was observed for IR820 as compared to that of IR820-ZnO (Figure 4.4.b). To detect superoxide, we have further done luminol chemiluminescence. More specifically, luminol is oxidised by superoxide ($O_2^{\cdot-}$) to produce chemiluminescence [46]. The rate of superoxide generation was studied by monitoring the emission peak of chemiluminescence at 425 nm [47]. As shown in Figure 4.4.c, chemiluminescence is observed for IR820-ZnO nanohybrid after red light irradiation for 15 minutes. For IR820-ZnO, the higher emission intensity at 425 nm as compared to that of IR820 indicates the greater generation of superoxide generation than IR820. We have observed from Figures 4.4.a, 4.4.b and 4.4.c that attachment of IR820 dye on ZnO nanoparticles, increases overall ROS production with reduction of singlet oxygen formation as compared to bare dye system. The fabricated nanohybrid is more photostable and more capable in producing overall reactive oxygen species but less in terms of singlet oxygen generation. We anticipate some relationship between these two aspects and further perform picosecond resolved studies to check excited state charge transfer dynamics. Figure 4.5.a represents the fluorescence decay profile of IR820 and IR820-ZnO nanohybrid monitored at 842 nm upon excitation 633 nm in DMSO. The excited state lifetime of IR820 quenches in nanohybrid as compared to that of free IR820 dye. The decay curve of IR820 is fitted with bi-exponential functions with the lifetime of 148 ps and 533.65 ps respectively. Being a NIR dye, IR820 is able to generate heat when it is exposed to NIR light [48]. Besides this, it generates singlet oxygen through energy transfer to triplet oxygen from its $T_1$ state [20, 21]. Because of this phenomenon, the average lifetime of the singlet excited state of IR820 is quite faster. The average lifetime is 456.52 ps. In case of IR820-ZnO nanohybrid, the emission decay curve is deviated from bi-exponential to tri-exponential which exhibits one ultrafast decay component of 39 ps (have a considerable contribution of 67.3%), which we attribute

the electron transfer from LUMO (lowest unoccupied molecular orbital) of IR820 to the conduction band of ZnO [49].

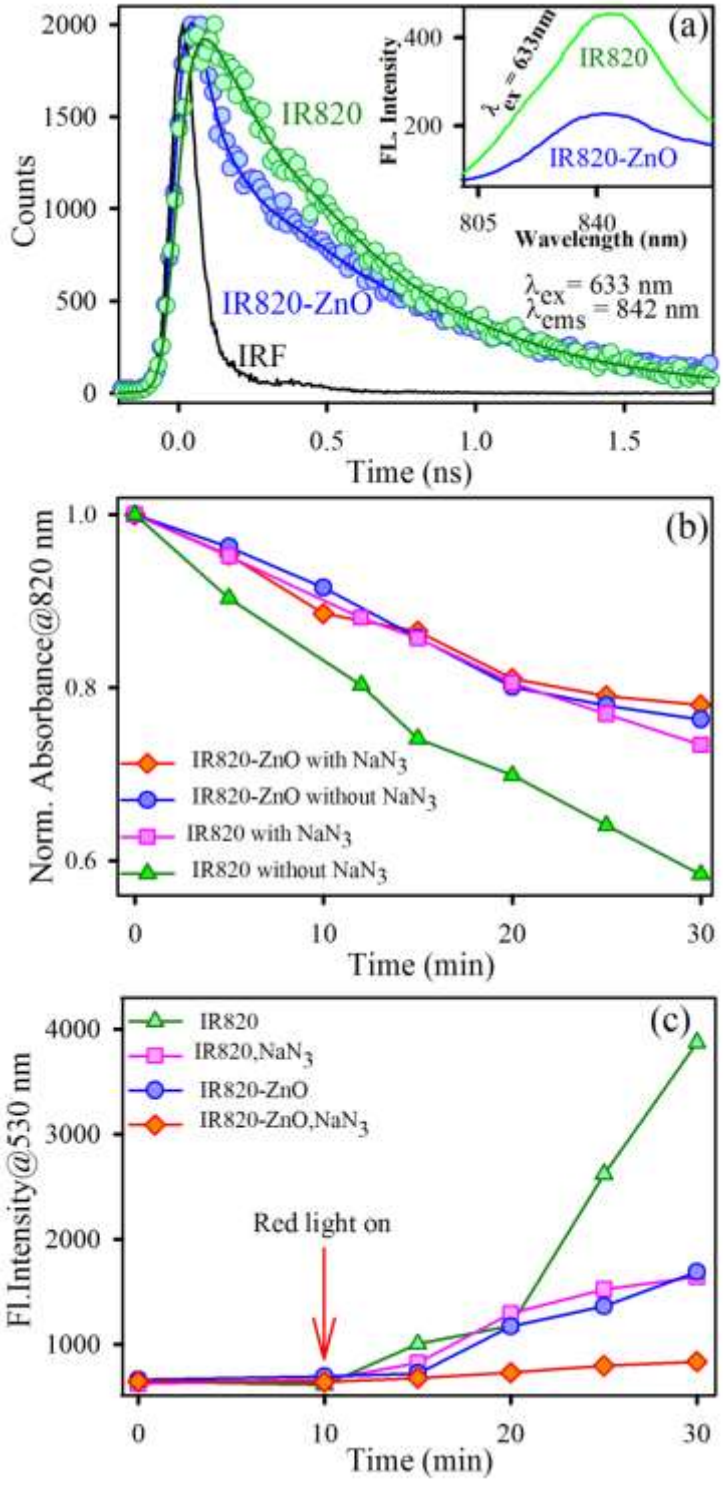


***Figure 4.5.*** *(a) Picosecond resolved fluorescence transients of IR820 and IR820-ZnO in DMSO. Inset shows steady state emission spectra of IR820 and IR820-ZnO in DMSO. (b) Time dependent photodegradation of IR820-ZnO and IR820 in presence of $NaN_3$. (c) SOSGR oxidation kinetics in presence of IR820-ZnO and IR820 in addition of $NaN_3$.*

The electron injection process from dye to semiconductor is due to the interaction between lower-density of sp orbital of $Zn^{+2}$ in ZnO with LUMO of IR820 [50]. The details of fitting parameters of fluorescence decays are provided in Table 4.1.

***Table 4.1.*** *Lifetime of picosecond time-resolved fluorescence transients of IR820 and IR820-ZnO nanohybrid, detected at 842 nm PL maxima upon excitation at 633 nm wavelength*

| System | $\tau_1$ (ps) | $\tau_2$ (ps) | $\tau_3$ (ps) | $\tau_{avg}$ (ps) |
|---|---|---|---|---|
| IR820 | 148 (20%) | 533.65 (80%) | | 456.52 |
| IR820-ZnO | 39 (67.27%) | 530 (22.73%) | 1264 (10%) | 273.10 |

This excited state photoelectron transfer from IR820 to ZnO also confirms the attachment of IR820 dye on ZnO surface. In principle, during the electron transfer process in the nanohybrid, electrons can flow towards the semiconductor either from the singlet and triplet excited states of IR820 [51, 52]. In our case, the finding of a very fast 39 ps time component strongly suggests that electron transfer occurs from the $S_1$ state [47]. To further confirm that this short living fluorescence component is connected to the occurrence of photoinduced electron transfer, we have repeated the measurement of time dependent fluorescence in the absence of oxygen, to restrict the possibility of other non−radiative decay processes [53, 54]. We found no significant changes in time scale in inert condition (data not shown). This observation firmly indicates that the fast time component present in IR820-ZnO is predominantly related to the electron transfer process from LUMO of IR820 to conduction band of ZnO. This in turn decreases the rate of ISC process and prevents the formation of triplet excited state in the photosensitizer dye [55], which reduces the triplet quantum yield [56]. Thus, the process of energy transfer from $T_1$ state of IR820 to triplet state of oxygen [57] (the overall dynamics is represented in the scheme 4.1) is reduced by electron transfer process. Hence, the singlet oxygen generation ability of IR820 on ZnO surface is reduced and the photoinduced excited state electron transfer process enhances overall generation of ROS (including superoxide) by the nanohybrid. In order to investigate the singlet

oxygen mediated photodegradation, a scavenger of singlet oxygen [58] ($NaN_3$) was added with IR820 and IR820-ZnO (in this case both IR820 and IR820-ZnO nanohybrid was in the mixture of DMSO and water and water and monitoring the absorption peak of IR820 at 820 nm) under red light irradiation for 30 min. In presence of $NaN_3$, the photodegradation of IR820 decreases from 42% to 27%. This is comparable with the IR820 degradation in the IR820-ZnO nanohybrid (the photodegradation of IR820-ZnO nanohybrid in DMSO and water mixture after 30 min is 24%). Whether, the degradation of the nanohybrid does not change significantly upon $NaN_3$ addition (Figure 4.5.b). The details of degradation percentage are reported in Table 4.2.

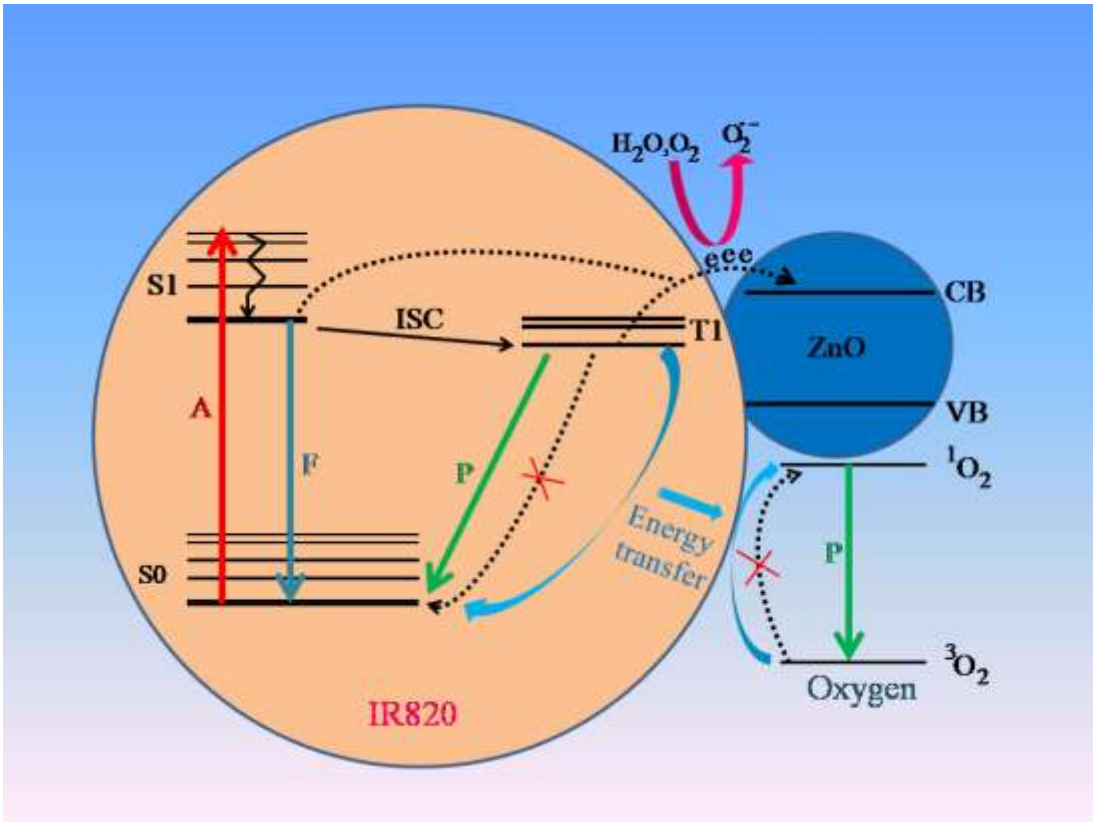


***Scheme 4.1.*** *Schematic representation of electron transfer and ROS generation dynamics.*

We have further performed the singlet oxygen sensor green reagent (SOSGR) assay in presence of $NaN_3$ under red light illumination for 20 minutes (Figure 4.5.c). In case of IR820, the fluorescence intensity at 530 nm reduces significantly in presence of $NaN_3$. For IR820-ZnO nanohybrid, the decrease in intensity at 530 nm is lower than

IR820. These results imply that, the greater generation of red-light-induced singlet oxygen species by IR820 reduces its photostability as compared to that of IR820-ZnO. Basically, the singlet oxygen attacks the polymethine chain of IR820 and produces fragmentation of the IR820 moiety [59].

***Table 4.2.*** *Percentage of photodegradation of IR820 and IR820-ZnO in water-DMSO mixture in presence and absence of* $NaN_3$

| System | Photodegradation |
|---|---|
| IR820 | 41.583% |
| IR820-ZnO | 23.649% |
| IR820, $NaN_3$ | 26.587% |
| IR820-ZnO,$NaN_3$ | 21.955% |

In case of IR820-ZnO nanohybrid, the electron capture process (from LUMO of IR820 to CB of ZnO) quenches the electron recombination process from triplet state to ground state ($S_0$) in IR820. Thus, it prevents the singlet generation as well as photobleaching of IR820. Also, due to excited state electron transfer from IR820 to ZnO, the electron deficiency in IR820 protects the dye from the singlet oxygen. Finally, we can conclude that we are able to enhance the photostability and activity of a NIR cyanine dye upon attachment with ZnO nanoparticles through a very easy synthesis pathway. We believe that the enhancement of photostability of IR820 in the nanohybrid and the enhancement of overall ROS generation ability by the nanohybrid. In view of application in targeted therapy, we have checked the dissolution and time dependent precipitation of IR820-ZnO nanohybrids in water at different pH values. For precipitation experiment, the decrease of stability of IR820-ZnO was monitored at 370 nm (the absorption peak for ZnO in nanohybrid). At pH 5, 40% IR820-ZnO nanohybrids are precipitated after 1 hr, whereas, 17% precipitation occurs at pH7 (Figure 4.6.a). Thus, the dispersion of IR820-ZnO nanohybrid is less stable in acidic solution as compared to that in neutral solution. Thus, the nanohybrids are expected to be deposited more in cancer cell (cancer cells are acidic in nature) as compared to that of others cell. The dissolution of IR820-ZnO

nanohybrid was monitored at 370 nm in neutral (pH 7) and acidic (pH 5) aqueous solutions. At pH 5, 42% IR820-ZnO nanohybrids are dissolved after 24 hr, whereas, 10% dissolution occurs at pH 7 (Figure 4.6.b). These results show that the IR820−ZnO nanohybrid has the ability to deliver the IR820 dye selectively in cancer cells.

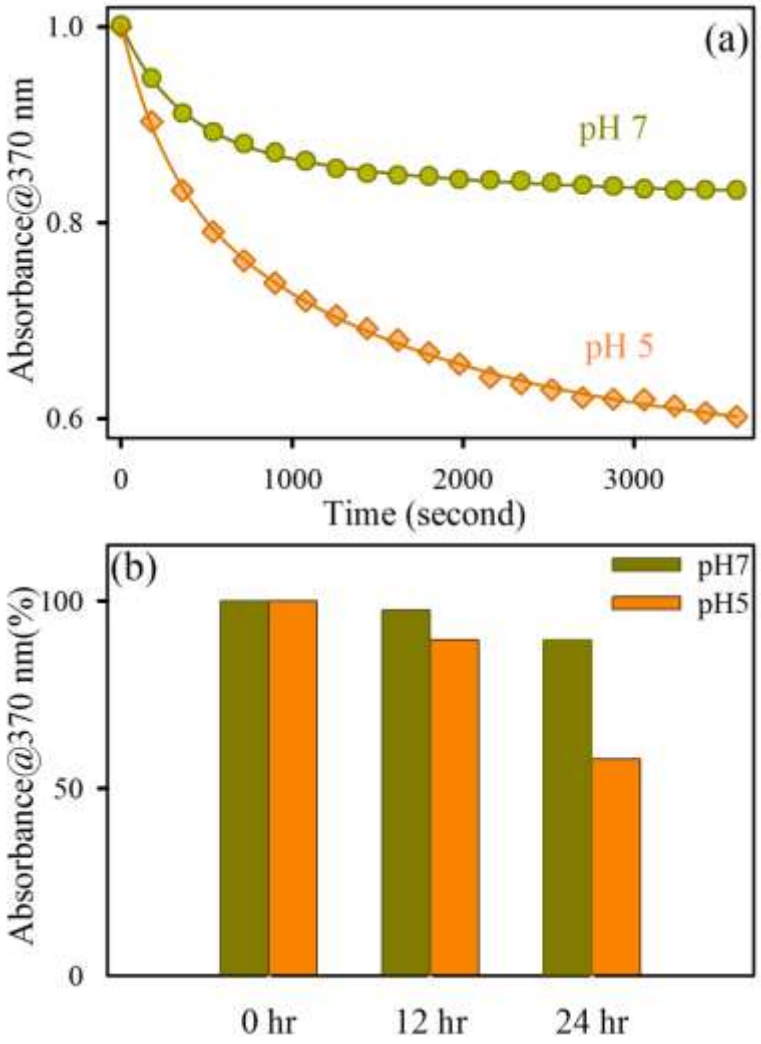


***Figure 4.6.*** *(a) Stability of nanohybrid from absorbance at 370 nm of IR820-ZnO dispersed in water at pH 5 and pH 7. (b) The dissolution of IR820-ZnO nanohybrid in water at pH 5 and pH 7.*

**4.3. Conclusion:** In summary, we have explored the advantages and improved effectiveness of IR820-ZnO nanohybrid over free IR820 dye which could be translated to its potential applications in various fields. The attachment of IR820 on ZnO surface was characterised using optical spectroscopic tools. Nanohybrid provides greater photostability with a large enhancement of photoinduced ROS.

Picosecond resolved fluorescence study explains the excited state electron transfer dynamics in the nanohybrid. The photoinduced excited state charge migration from IR820 to ZnO in the nanohybrid is responsible for the generation of overall ROS over free IR820 dye. This photo-induced electron transfer process is also responsible to generate singlet oxygen deficiency in nanohybrid which subsequently improves the photostability of the nanohybrid. Our findings reveal that, for a well-known NIR cyanine dye IR820, the photostability and the ability of overall ROS generation enhances upon attachment on ZnO surface. The key advantages of IR820 attachment on ZnO surface are enhancement of photostability, restriction in thermal degradation, efficiency in ROS generation and targeted delivery towards cancer cells. The developed strategy could be applied to other NIR cyanine dyes that will improve their potential applications in light-harvesting fields.

# References


[1] I. Robel, V. Subramanian, M. Kuno, P.V. Kamat, Quantum dot solar cells. Harvesting light energy with CdSe nanocrystals molecularly linked to mesoscopic $TiO_2$ films, *J. Am. Chem. Soc.* 128 (2006) 2385.

[2] Q. Tian, W. Yao, W. Wu, C. Jiang, NIR light-activated upconversion semiconductor photocatalysts, *Nanoscale Horiz.* 4 (2019) 10.

[3] J. Zhao, D. Zhong, S. Zhou, NIR-I-to-NIR-II fluorescent nanomaterials for biomedical imaging and cancer therapy, *J. Mater. Chem. B* 6 (2018) 349.

[4] C. Wang, H. Tao, L. Cheng, Z. Liu, Near-infrared light induced *in vivo* photodynamic therapy of cancer based on upconversion nanoparticles, *Biomaterials* 32 (2011) 6145.

[5] O. Stroyuk, A. Raevskaya, N. Gaponik, Solar light harvesting with multinary metal chalcogenide nanocrystals, *Chem. Soc. Rev.* 47 (2018) 5354.

[6] T. Mahmood, C. Chuncheng, L. Lili, Z. Dan, M. Wanghong, L. Jun, Z. Jincai, Effect of dye-metal complexation on photocatalytic decomposition of the dyes on $TiO_2$ under visible irradiation, *J. Environ. Sci.* 21 (2009) 263.

[7] M. Wang, J. Ioccozia, L. Sun, C. Lin, Z. Lin, Inorganic-modified semiconductor $TiO_2$ nanotube arrays for photocatalysis., *Energy Environ. Sci.* 7 (2014) 2182.

[8] Y. Zheng, C. Chen, Y. Zhan, X. Lin, Q. Zheng, K. Wei, J. Zhu, Y. Zhu, Luminescence and photocatalytic activity of ZnO nanocrystals: Correlation between structure and property, *Inorg. Chem.* 46 (2007) 6675.

[9] B. Zhou, Y. Li, G. Niu, M. Lan, Q. Jia, Q. Liang, Near-infrared organic dye-based nanoagent for the photothermal therapy of cancer, *ACS Appl. Mater. Interfaces* 8 (2016) 29899.

[10] R.L. Watley, S.G. Awuah, M. Bio, R. Cantu, H.B. Gobeze, V.N. Nesterov, S.K. Das, F. D'Souza, Y. You, Dual functioning thieno-pyrrole fused BODIPY dyes for NIR optical imaging and photodynamic therapy: Singlet oxygen generation without heavy halogen atom assistance, *Chem. Asian J.* 10 (2015) 1335.

[11] A. Burke, L. Schmidt-Mende, S. Ito, M. Grätzel, A novel blue dye for near-IR dye-sensitised solar cell applications, *ChemComm* 17 (2007) 234.

[12] S. Hao, Y. Shang, D. Li, H. Ågren, C. Yang, G. Chen, Enhancing dye-sensitized solar cell efficiency through broadband near-infrared upconverting nanoparticles, *Nanoscal*e, 9 (2017) 6711.

[13] O. Suryani, Y. Higashino, H. Sato, Y. Kubo, Visible-to-near-infrared light-driven photocatalytic hydrogen production using dibenzo-BODIPY and phenothiazine conjugate as organic photosensitizer, *ACS Appl. Energy Mat*er. 2 (2018) 448.

[14] W. Wu, F. Meng, J. Li, X. Teng, J. Hua, Co-sensitization with near-IR absorbing cyanine dye to improve photoelectric conversion of dye-sensitized solar cells, *Synth. Met.* 159 (2009) 1028.

[15] A.P. Thomas, L. Palanikumar, M. Jeena, K. Kim, J.-H. Ryu, Cancer-mitochondria-targeted photodynamic therapy with supramolecular assembly of HA and a water soluble NIR cyanine dye, *Chem. Sci.* 8 (2017) 8351.

[16] I. Kobasa, N. Gusyak, L. Odosii, Titanium dioxide sensitization with a biscyanine dye in the photocatalytic reduction of methylene blue, *Kinet. Catal.* 56 (2015) 158.

[17] J. Atchison, S. Kamila, H. Nesbitt, K.A. Logan, D.M. Nicholas, C. Fowley, J. Davis, B. Callan, A.P. McHale, J.F. Callan, Iodinated cyanine dyes: A new class of sensitisers for use in NIR activated photodynamic therapy (PDT), *ChemComm* 53 (2017) 2009.

[18] A. Fernandez-Fernandez, R. Manchanda, T. Lei, D.A. Carvajal, Y. Tang, S.Z.R. Kazmi, A.J. McGoron, Comparative study of the optical and heat generation properties of IR820 and indocyanine green, *Mol. Imaging* 11 (2012) 7290.

[19] N. Shao, Y. Qi, H. Lu, D. He, B. Li, Y. Huang, Photostability Highly Improved Nanoparticles Based on IR-780 and Negative charged copolymer for enhanced photothermal therapy, *ACS Biomater. Sci. Eng*. 5 (2018) 795.

[20] Q. Zheng, L.D. Lavis, Development of photostable fluorophores for molecular imaging, *Curr. Opin. Chem. Biol.* 39 (2017) 32.

[21] B. Fückel, D.A. Roberts, Y.Y. Cheng, R.G. Clady, R.B. Piper, N. Ekins-Daukes, M.J. Crossley, T.W. Schmidt, Singlet oxygen mediated photochemical upconversion of NIR light, *J. Phys. Chem. Lett.* 2 (2011) 966.

[22] S.G. Awuah, J. Polreis, V. Biradar, Y. You, Singlet oxygen generation by novel NIR BODIPY dyes, *Org. Lett.* 13 (2011) 3884.

[23] A. Pajares, J. Gianotti, E. Haggi, G. Stettler, F. Amat-Guerri, S. Criado, S. Miskoski, N.A. García, Kinetic study of the singlet molecular oxygen-mediated photodegradation of monohydroxylated N-heteroaromatic compounds, *J. Photochem. Photobiol. A* 119 (1998) 9.

[24] A. Gorman, M. Rodgers, Singlet molecular oxygen, *Chem. Soc. Rev.* 10 (1981) 205.

[25] A.A. Earp, T. Rawling, J.B. Franklin, G.B. Smith, Perylene dye photodegradation due to ketones and singlet oxygen, *Dyes Pigm.* 84 (2010) 59.

[26] B.R. Renikuntla, H.C. Rose, J. Eldo, A.S. Waggoner, B.A. Armitage, Improved photostability and fluorescence properties through polyfluorination of a cyanine dye, *Org. Lett.* 6 (2004) 909.

[27] Y. Matsuzawa, S.-i. Tamura, N. Matsuzawa, M. Ata, Light stability of a β-cyclodextrin inclusion complex of a cyanine dye, *J. Chem. Soc. Faraday Trans.* 90 (1994) 3517.

[28] K. Funabiki, K. Yagi, M. Nomoto, Y. Kubota, M. Matsui, Improvement of the thermal stability of near-infrared-absorbing heptamethinecyanine dyes by anion-exchange from an iodide to fluorine-containing anions, J. Fluor. Chem. 174 (2015) 132.

[29] L. Jiao, F. Song, B. Zhang, H. Ning, J. Cui, X. Peng, Improving the brightness and photostability of NIR fluorescent silica nanoparticles through rational fine-tuning of the covalent encapsulation methods, *J. Mater. Chem. B* 5 (2017) 5278.

[30] B. Quan, K. Choi, Y.-H. Kim, K.W. Kang, D.S. Chung, Near infrared dye indocyanine green doped silica nanoparticles for biological imaging, *Talanta* 99 (2012) 387.

[31] H. Zhang, L. Liu, C. Gao, R. Sun, Q. Wang, Enhancing photostability of cyanine dye by cucurbituril encapsulation, *Dyes Pigm.* 94 (2012) 266.

[32] N.I. Shank, K.J. Zanotti, F. Lanni, P.B. Berget, B.A. Armitage, Enhanced photostability of genetically encodable fluoromodules based on fluorogenic cyanine dyes and a promiscuous protein partner, *J. Am. Chem. Soc.* 131 (2009) 12960.

[33] Q. Zheng, S. Jockusch, G.G. Rodríguez-Calero, Z. Zhou, H. Zhao, R.B. Altman, H.D. Abruña, S.C. Blanchard, Intra-molecular triplet energy transfer is a general approach to improve organic fluorophore photostability, *Photochem. Photobiol. Sci.* 15 (2016) 196.

[34] P. Jayaweera, A. Perera, M. Senevirathna, P. Pitigala, K. Tennakone, Dye-sensitized near-infrared room-temperature photovoltaic photon detectors, *Appl. Phys. Lett.* 85 (2004) 5754.

[35] D. Yin, Y. Liu, J. Tang, F. Zhao, Z. Chen, T. Zhang, X. Zhang, N. Chang, C. Wu, D. Chen, Huge enhancement of upconversion luminescence by broadband dye sensitization of core/shell nanocrystals, *Dalton Trans.* 45 (2016) 13392.

[36] G. Chen, J. Damasco, H. Qiu, W. Shao, T.Y. Ohulchanskyy, R.R. Valiev, X. Wu, G. Han, Y. Wang, C. Yang, Energy-cascaded upconversion in an organic dye-sensitized core/shell fluoride nanocrystal, *Nano Lett.* 15 (2015) 7400.

[37] A. Fernandez-Fernandez, R. Manchanda, D.A. Carvajal, T. Lei, S. Srinivasan, A.J. McGoron, Covalent IR820-PEG-diamine nanoconjugates for theranostic applications in cancer, *Int. J. Nanomed.* 9 (2014) 4631.

[38] D. Bagchi, V.S. Rathnam, P. Lemmens, I. Banerjee, S.K. Pal, NIR-light-active ZnO-based nanohybrids for bacterial biofilm treatment, *ACS omega* 3 (2018) 10877.

[39] A. Bera, D. Bagchi, S.K. Pal, Improvement of photostability and NIR activity of cyanine dye through nanohybrid formation: Key information from ultrafast dynamical studies, *J. Phys. Chem. A* 123 (2019) 7550.

[40] D.L. Golić, G. Branković, M.P. Nešić, K. Vojisavljević, A. Rečnik, N. Daneu, S. Bernik, M. Šćepanović, D. Poleti, Z. Branković, Structural characterization of self-assembled ZnO nanoparticles obtained by the sol–gel method from Zn $(CH_3COO)_2 \cdot 2H_2O$, *Nanotechnology* 22 (2011) 395603.

[41] S.S. Kumar, P. Venkateswarlu, V.R. Rao, G.N. Rao, Synthesis, characterization and optical properties of zinc oxide nanoparticles, *Int. Nano Lett.* 3 (2013) 30.

[42] H. Mustroph, K. Reiner, J. Mistol, S. Ernst, D. Keil, L. Hennig, Relationship between the molecular structure of cyanine dyes and the vibrational fine structure of their electronic absorption spectra, *ChemPhysChem* 10 (2009) 835.

[43] H. v. Berlepsch, C. Bo̎ttcher, H-aggregates of an indocyanine Cy5 dye: Transition from strong to weak molecular coupling, *J. Phys. Chem. B* 119 (2015) 11900.
[44] K. Vus, U. Tarabara, A. Kurutos, O. Ryzhova, G. Gorbenko, V. Trusova, N. Gadjev, T. Deligeorgiev, Aggregation behavior of novel heptamethine cyanine dyes upon their binding to native and fibrillar lysozyme, *Mol. BioSyst.* 13 (2017) 970.
[45] D. Bagchi, A. Halder, S. Debnath, P. Saha, S.K. Pal, Exploration of interfacial dynamics in squaraine based nanohybrids for potential photodynamic action, *J. Photochem. Photobiol. A* 380 (2019) 111842.
[46] A.L. Rose, T.D. Waite, Chemiluminescence of luminol in the presence of iron (II) and oxygen: Oxidation mechanism and implications for its analytical use, *Anal. Chem.* 73 (2001) 5909.
[47] S. Sardar, S. Chaudhuri, P. Kar, S. Sarkar, P. Lemmens, S.K. Pal, Direct observation of key photoinduced dynamics in a potential nano-delivery vehicle of cancer drugs, *Phys. Chem. Chem. Phys.* 17 (2015) 166.
[48] P. Kumar, R. Srivastava, IR 820 stabilized multifunctional polycaprolactone glycol chitosan composite nanoparticles for cancer therapy, *RSC Adv.* 5 (2015) 56162.
[49] J. Patwari, A. Chatterjee, S. Sardar, P. Lemmens, S.K. Pal, Ultrafast dynamics in co-sensitized photocatalysts under visible and NIR light irradiation, *Phys. Chem. Chem. Phys.* 20 (2018) 10418.
[50] N.A. Anderson, T. Lian, Ultrafast electron transfer at the molecule-semiconductor nanoparticle interface, *Annu. Rev. Phys. Chem.* 56 (2005) 491.
[51] B. Patrick, P. Kamat, Photosensitization of large-bandgap semiconductors. Charge injection from triplet excited thionine into ZnO colloids, *J. Phys. Chem.* 96 (1992) 1423.
[52] L. Jiao, F. Song, J. Cui, X. Peng, A near infrared heptamethine aminocyanine dye with a long-living excited triplet state for photodynamic therapy, *ChemComm* 78 (2018) 1713.
[53] C. Parmenter, J. Rau, Fluorescence quenching in aromatic hydrocarbons by oxygen, *J. Chem. Phys.* 51 (1969) 2242.

[54] F.M. Cabrerizo, J. Arnbjerg, M.P. Denofrio, R. Erra-Balsells, P.R. Ogilby, Fluorescence quenching by oxygen:"Debunking" a classic rule, *ChemPhysChem* 11 (2010) 796.

[55] D. Liu, P.V. Kamat, K.G. Thomas, K. Thomas, S. Das, M. George, Picosecond dynamics of an IR sensitive squaraine dye: Role of singlet and triplet excited states in the photosensitization of $TiO_2$ nanoclusters, *J. Chem. Phys.* 106 (1997) 6404.

[56] M.O. Lenz, J. Wachtveitl, Quenching of triplet state formation by electron transfer for merocyanine/$TiO_2$ systems, *J. Phys. Chem. C* 112 (2008) 11973.

[57] J. Herman, Y. Zhang, V. Castranova, S.L. Neal, Emerging technologies for optical spectral detection of reactive oxygen species, *Anal. Bioanal. Chem*. 235 (2018) 1.

[58] R. Huang, E. Choe, D. Min, Kinetics for singlet oxygen formation by riboflavin photosensitization and the reaction between riboflavin and singlet oxygen, *J. Food Sci.* 69 (2004) C726.

[59] N. James, R. Cheruku, J. Missert, U. Sunar, R. Pandey, Measurement of cyanine dye photobleaching in photosensitizer cyanine dye conjugates could help in optimizing light dosimetry for improved photodynamic therapy of cancer, *Molecules* 23 (2018) 1842.

# Chapter 5

# Synthesis and Combined Spectroscopic Computational Studies on a NIR-Active Nanohybrid for Potential Biological Application

**5.1. Introduction:** Light-triggered therapeutic platforms constitute an elegant non-invasive medical tool to kill cancer cells [1], because, light can not only be easily tuned and focused but also causes less damage to the healthy tissues. Among such therapeutic platforms, photodynamic therapy (PDT) offers the advantage of having good specificity for treatment of cancer and tumours [2, 3] upon exposure to light of certain wavelengths (UV-vis to NIR) [4]. In PDT, photosensitizer molecules upon irradiation by light of a suitable wavelength transfer the absorbed photon energy to oxygen molecules in the surroundings, generating reactive oxygen species (ROS) to kill malignant cells [4]. It has been observed that the tissue penetration depth of light in the near-infrared (NIR) region (700-1350 nm) is about an order of magnitude greater than that of UV-visible light [5, 6] and so for biological applications, an optimal tissue penetration depth is achieved with irradiation of light in the NIR region, also called the "therapeutic window" causing minimal damage to the healthy tissues. Therefore, development of NIR-light triggered photosensitizers is of potential importance for clinical applications.

Recently, several NIR dyes have found application in PDT because of their better light absorptivity and ability in generating ROS. Among them, US food and drug administration (FDA) approved Indocyanine green (ICG, Figure 1a) possesses considerably low toxicity and very good biocompatibility compared to the other NIR dyes [7-9]. ICG mainly generates singlet oxygen as ROS [10]. Most of the NIR cyanine dyes aggregate easily in water, thereby reducing fluorescence quantum yields, triplet states and singlet oxygen generation [11]. The efficiency of overall ROS production by ICG is poor [12, 13] due to its aggregation in water [13, 14] which

affects its efficiency for use as a photodynamic drug. To circumvent this limitation we have fabricated a nanohybrid of ZnO nanoparticles (NP) and ICG which is capable of producing significantly large quantity of ROS relative to ICG, and hence emerges as a potential candidate for use as a PDT agent. We have chosen ZnO NPs because of their biocompatibility, negligible toxicity along with their size-dependent antimicrobial property [15] Photophysical studies indicate the presence of an excited state electron transfer from ICG to ZnO which likely contributes to significantly enhanced ROS generation by the ICG-ZnO nanohybrid compared to ICG. Molecular dynamics (MD) simulation shows the most probable way of binding ICG on the ZnO surface. Classical MD simulation shows the dimeric structure of ICG breakes down on ZnO surface which corroborates results from the aggregation study in water. Density functional theory (DFT) and time dependent-density functional theory (TD-DFT) studies elucidate possible major electronic transitions in ICG upon photoexcitation and have demonstrated excited state electron transfer from the lowest unoccupied molecular orbital (LUMO) of ICG to the conduction band of ZnO which corroborates results from the photophysical studies. Finally, the remarkable efficiency of the ICG-ZnO nanohybrid in generating ROS upon light irradiation is demonstrated by a dose-dependent inhibition of a gram-negative bacteria (*E. coli*) which is responsible for many types of infections in humans including urinary tract infections [16, 17]. The present study provides a potential strategy to significantly improve the therapeutic potential of ICG in terms of fabricating its nanohybrid for use as a photosensitizer in antibacterial photodynamic therapy as well as PDT.

## 5.2. Results and discussion:

**5.2.1. Improving Therapeutic Potential of a NIR photo-sensitizer via Fabrication of Nanohybrids: An Optical Spectroscopic and Computational Study [18]:** From the high-resolution transmission electron microscopic image (HRTEM, Figure 5.1.b), an average diameter of the ZnO nanoparticles is found to be ~20 nm. Figures 5.1.c and 5.1.d display characteristic X-ray diffraction patterns of ZnO nanoparticles (violet) and ICG-ZnO nanohybrid (blue), respectively. The diffraction pattern of the ZnO nanoparticles corresponds to hexagonal wurtzite [19] structure and remains

unchanged upon conjugation with ICG indicating that the crystal structure of ZnO remains unaltered following the attachment of ICG. To confirm the attachment of ICG to ZnO NP surfaces, the Fourier transform infrared (FTIR) technique has been used (Figure 5.2). The free ICG possesses stretching frequencies at 1221 $cm^{-1}$, which attributes to the SO stretching of a sulfonate group. The adjacent peak at 1061 $cm^{-1}$ corresponds to the C-C stretching. All the characteristic peaks of ICG and ZnO are visible in the ICG-ZnO nanohybrid. Later on, the computational study shows that ICG binds to the ZnO surface *via* the sulfonate groups by Coulomb interaction. The absorption spectrum of ICG in methanol (Figure 5.3.a) is characterized by the main peak at 780 nm along with a shoulder at 720 nm.

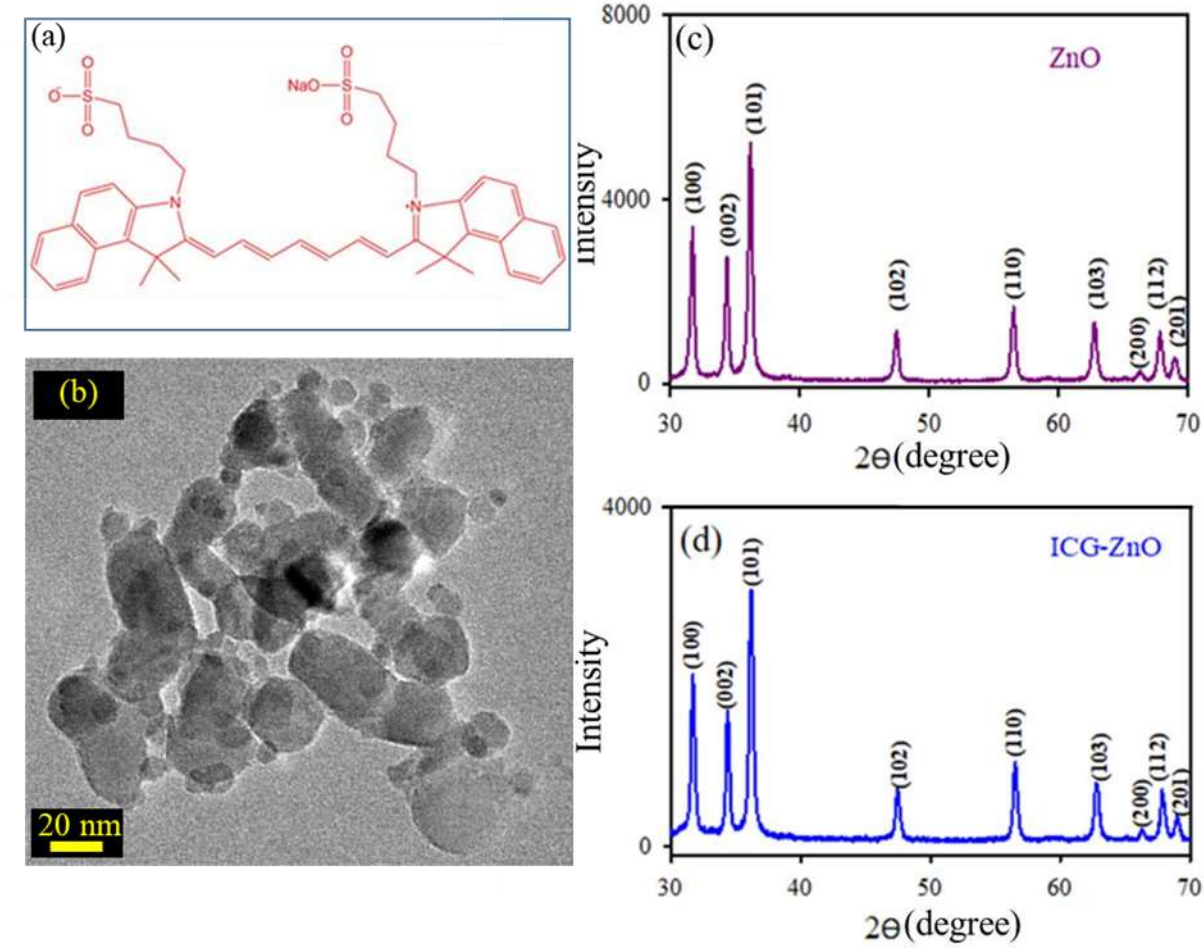


***Figure 5.1.*** *(a) Structure of ICG. (b) HRTEM image of ZnO nanoparticles. Powder XRD pattern of (c) ZnO (violet) and (d) ICG-ZnO (blue) nanohybrid respectively.*

The peak maximum at 780 nm is ascribed to the 0→0 transition whereas the shoulder at 720 nm corresponds to the 0→1 vibronic sub-band under S0→S1 electronic transition [20, 21] Steady state emission spectrum of ICG (the concentration of ICG

close to 3 μM) in methanol (Figure 5.3.b) shows two characteristic peaks at 700 nm and 810 nm, respectively. Upon monitoring the emission at 730 nm a main peak at 690 nm along with a shoulder at 630 nm is found (Figure 5.3.c). These observations indicate that the two emission peaks originate from two completely different forms of ICG. The emission peak at 810 nm is attributed to the monomer whereas the dimeric form of ICG emits ~700 nm [22-23].

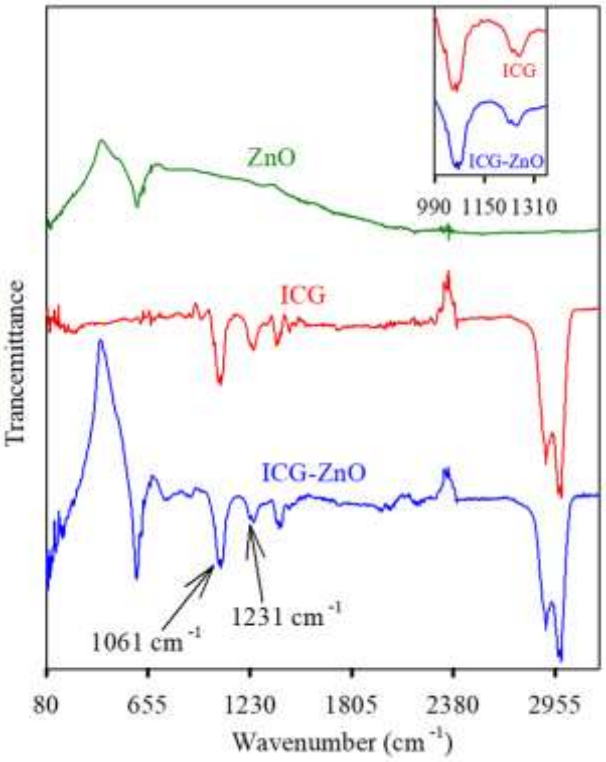


***Figure 5.2:*** *FTIR spectra of ICG (red), ICG-ZnO (blue) and ZnO (green).*

These observations indicate that the two emission peaks originate from two completely different forms of ICG. The emission peak at 810 nm is attributed to the monomer whereas the dimeric form of ICG emits ~700 nm [22-24]. The excitation spectrum of ICG monitored at 840 nm shows two peaks (Figure 5.3.d) that closely resembles the absorption spectrum. Picosecond-resolved fluorescence transients of ICG in methanol at 810 and 700 nm (Figure 5.4.a) could be satisfactorily fitted with a biexponential decay function characterized by two decay components (Table 5.1). The mean fluorescence lifetime of the monomeric excited state is 0.522 ns whereas that corresponding to the dimeric excited state is 0.821 ns. Time-resolved fluorescence anisotropy decays of ICG (Figure 5.4b. and 5.4.c) in methanol were

fitted by an impulse convolution model [25]. The anisotropy decay at 814 nm is characterized by two rotational correlation times of 298 ps (53%) and 1.47 ns (47%) with an average rotational time constant of 0.85 ns (Table 5.2) whereas that at 700 nm becomes much slower with an average rotational correlation time of 2.43 ns.

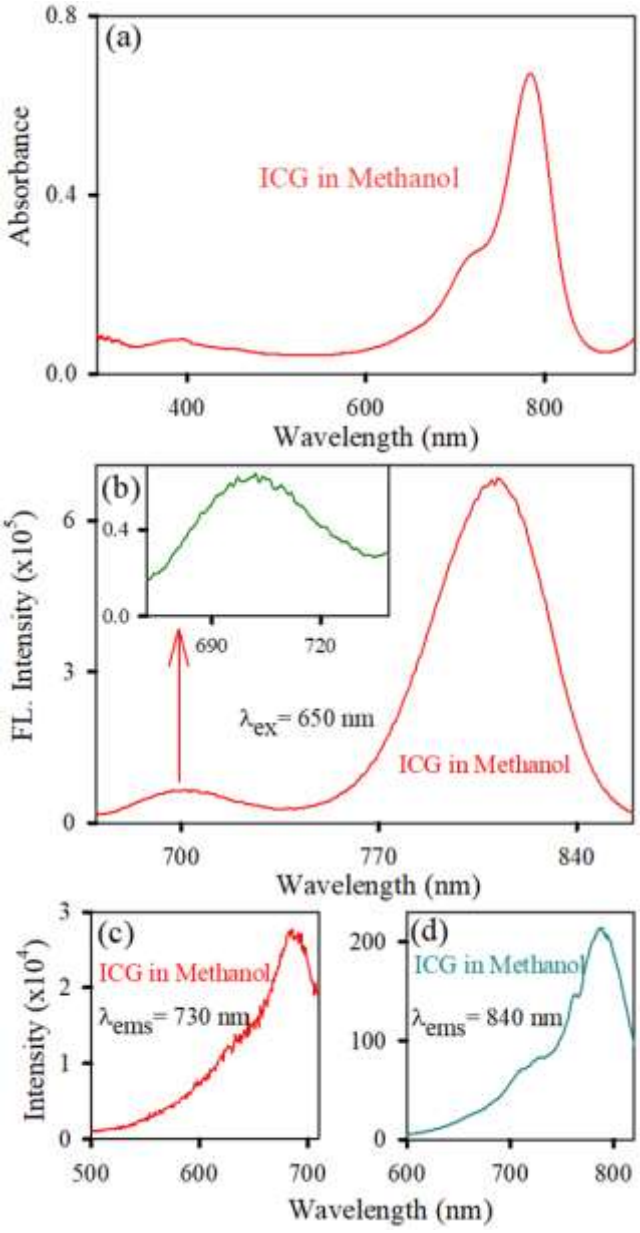


***Figure 5.3.*** *(a) UV-VIS absorption spectra of ICG (red) in methanol. (b) Room temperature emission spectra of ICG (red) in methanol. Inset shows magnified absorption spectra of ICG (green) from 672 nm to 739 nm. Excitation spectra of ICG in methanol at the emission peak of (c) 730 nm (red) and (d) 840 nm (dark cyan) respectively.*

The absorption spectrum of ICG-ZnO nanohybrid (Figure 5.5.a) is characterized by peaks of both ICG and ZnO. The white colour of ZnO nanoparticles changes to dark green (inset, Figure 5.4c) upon the formation of nanohybrid indicating functionalization of

the dye (ICG) with ZnO nanoparticles. Thus, both fluorescence lifetime and the rotational relaxation time of the monomer of ICG are different from that of the dimeric form.

***Table 5.1.*** *Fluorescence lifetime of ICG in methanol*

| System | Emission Wavelength (nm) | $\tau_1$ (ns) | $\tau_2$ (ns) | $\tau_{avg}$ (ns) |
|---|---|---|---|---|
| ICG | 810 | 0.117 ± 0.01 (17 %) | 0.603 ± 0.03 (83%) | 0.520 |
| ICG | 700 | 0.317 ± 0.02 (24%) | 0.982 ± 0.04 (76%) | 0.822 |

We have also recorded the absorbance of both ICG and ICG-ZnO nanohybrid in water (Figure 5.5.b) after 5 hours of storage to check the effect of nanohybrid formation on aggregation of the dye in aqueous medium.

***Table 5.2****. Time-resolved Fluorescence Anisotropy of ICG in methanol*

| *Emission wavelength (nm)* | $a_1$ | $\phi_1$/ns | $a_2$ | $\phi_2$/ns | k | $\langle\phi\rangle$/ns | $r_0$ |
|---|---|---|---|---|---|---|---|
| 814 | 0.12 | 0.298 | 0.10 | 1.47 | 0.17 | 0.85 | 0.39 |
| 700 | 0.13 | 0.355 | 0.07 | 5.96 | 0.18 | 2.43 | 0.38 |

*{Anisotropy decays, r(t), were fitted by an impulse reconvolution model as* $r(t) = a_1 exp(-t/\phi_1) + a_2 exp(-t/\phi_2) + k$ *where* $\phi_1$, $\phi_2$ *and* $a_1$, $a_2$ *are the rotational correlation times and their corresponding amplitudes, respectively. k is residual anisotropy,* $r_0$ *is intial anisotropy defined as* $r_0 = a_1 + a_2 + k$*. The average rotational relaxation time (*$\langle\phi\rangle$*) is calculated by* $\langle\phi\rangle = a_1\phi_1 + a_2\phi_2$ *where amplitudes are re-normalized as* $|\beta_1| + |\beta_2| = 1$*.}*

It becomes evident that the shoulder at ~700 nm becomes progressively more prominent for ICG in water, indicating the formation of H-like aggregates [20, 23, 24, 26]. As for the ICG-ZnO nanohybrid, the absorption peak at ~700 nm becomes reduced relative to ICG which shows that attachment of ICG on the ZnO surface protects the dye from H-like aggregation in aqueous medium. A comparison of the steady-state photoluminescence (PL) spectrum of ICG and ICG-ZnO in DMSO

(Figure 5.5.c) displays quenching of both the emission peaks of ICG at 818 nm (monomeric state) and 708 nm (dimeric state) upon nanohybrid formation.

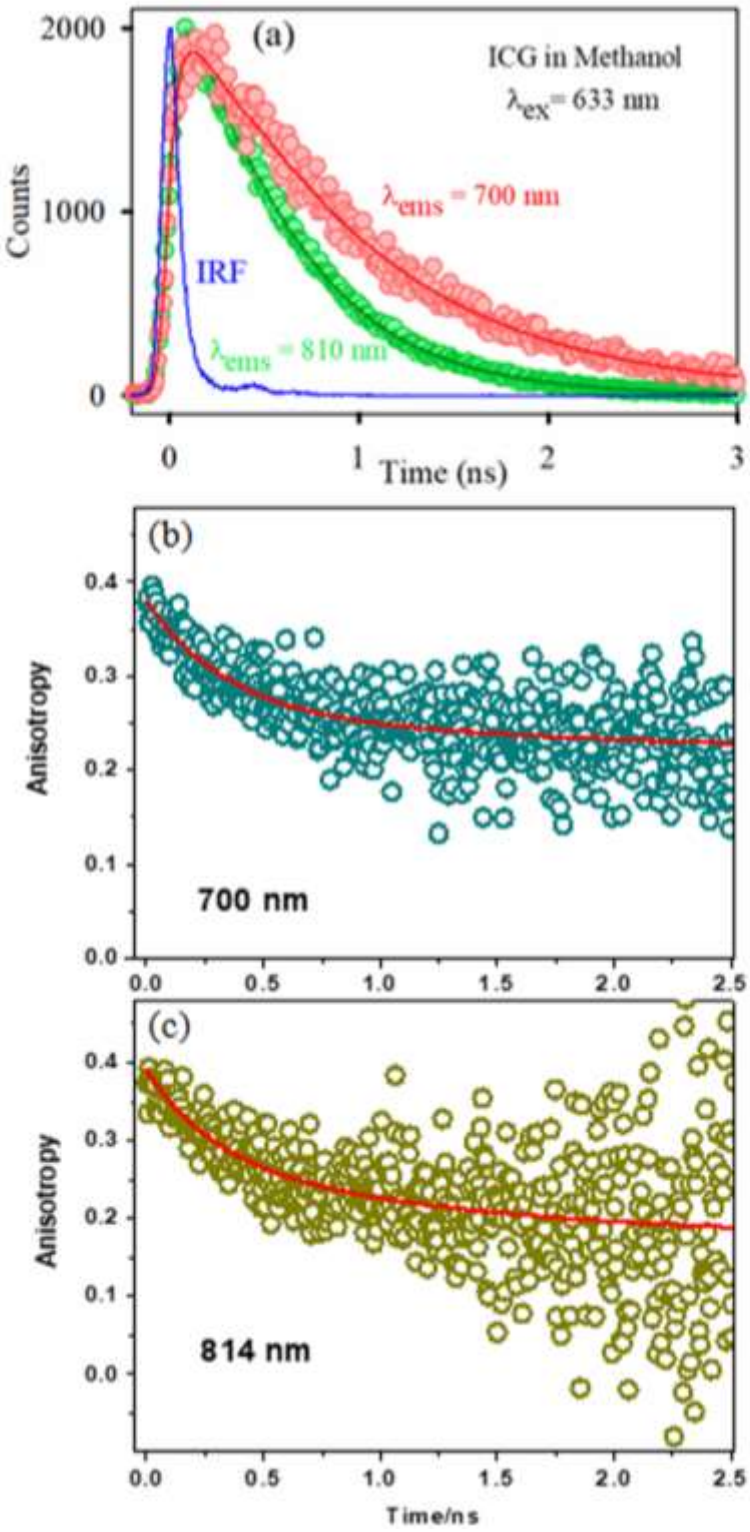


***Figure 5.4.*** *(a) Picosecond resolved fluorescence transients of ICG in methanol corresponding to 700 nm (red) and 810 nm (green). (b) and (c) Time-resolved Fluorescence Anisotropy of ICG in methanol at 700 nm and at 814 nm, respectively. Fitted decays are represented by solid lines (red).*

This is reflected further by faster fluorescence decays of the ICG-ZnO nanohybrid (Figure 5.6.a & 5.6.b) at both the wavelengths (818 nm and 708 nm) relative to the ICG dye. As for example, the fluorescence decay of ICG at 818 nm is characterized by two-time constants of 0.124 ns and 0.908 ns with an average fluorescence lifetime of 0.783 ns (Table 5.3) which decrease significantly for the nanohybrid (0.220 ns) due to the emergence of a much faster decay component (~38 ps).

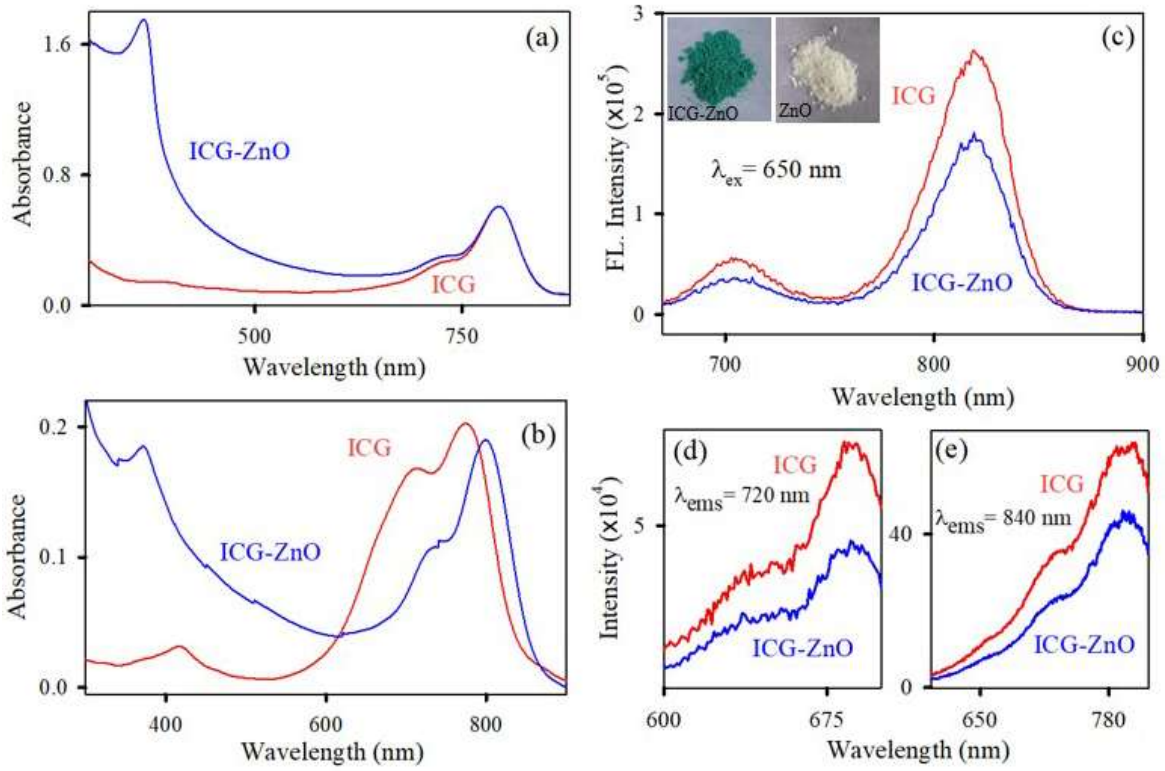


***Figure 5.5.*** *(a) UV-VIS absorption spectra of ICG (red) and ICG-ZnO (blue) nanohybrid in DMSO. (b) Absorption spectra of ICG (red) and ICG-ZnO (blue) nanohybrid in water. (c) Room temperature emission spectra of ICG (red) and ICG-ZnO (blue) in DMSO. Inset shows the photographs of ZnO and ICG-ZnO nanohybrid. (d) Excitation spectra of ICG (red) and ICG-ZnO (blue) in DMSO upon Emission 720 nm.(e) Excitation spectra of ICG (red) and ICG-ZnO (blue) in DMSO upon Emission 840 nm.*

Similarly, the fluorescence lifetime of ICG at 708 nm is reduced from 1.190 ns to 0.510 ns upon formation of the ICG-ZnO nanohybrid owing to an additional decay component of ~62 ps. The faster time constant ($\tau_1$ = 38-62 ps, Table 5.3) mainly contributes to faster fluorescence decays of the ICG-ZnO nanohybrid relative to ICG (Figure 5.6.a & 5.6.b) and is indicative of photoinduced interfacial excited state electron transfer process from the monomeric or the dimeric excited state of ICG to the conduction band (CB) of ZnO NPs [27-29]. The interaction between the lowest

unoccupied molecular orbital (LUMO) of ICG and the lower density sp orbital of $Zn^{2+}$ in ZnO likely constitutes this electron transfer process [30].

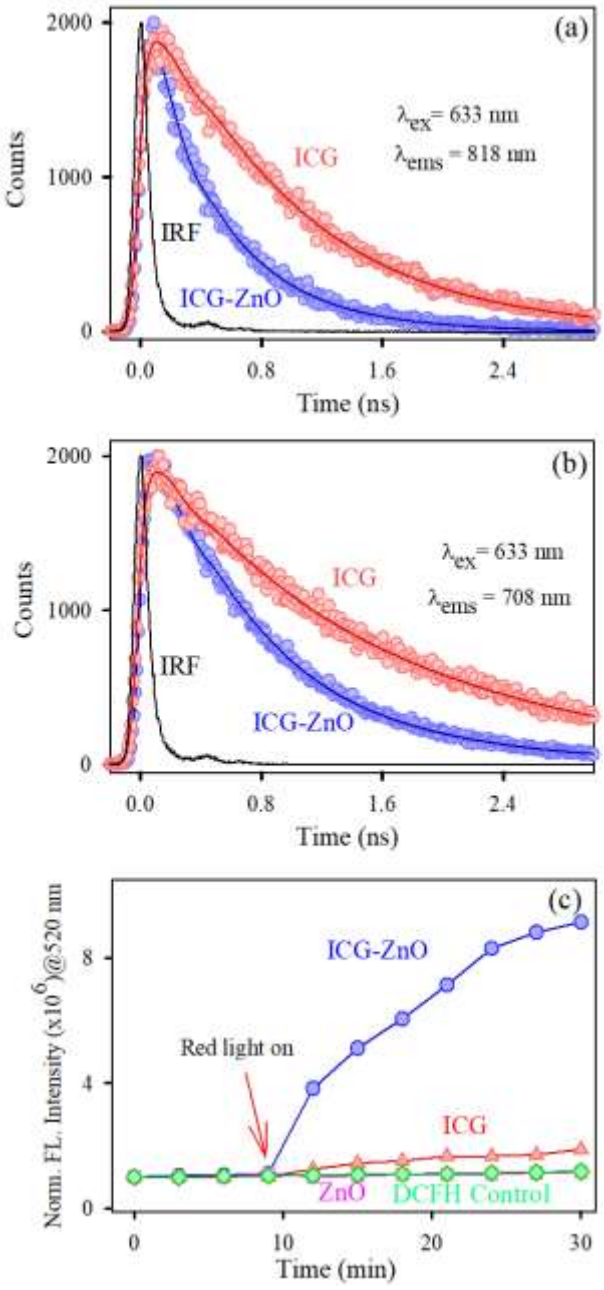


***Figure 5.6.*** *(a) Picosecond resolved fluorescence transients of ICG (red) and ICG-ZnO (blue) at 818 nm in DMSO. (b) Picosecond resolved fluorescence transients of ICG (red) and ICG-ZnO (blue) at 708 nm in DMSO. (c) DCFH oxidation (monitored at 520 nm) with time in presence of ICG-ZnO (blue), ICG (red), ZnO (pink) and DCFH (green) only under dark (9 min) and red light (21 min).*

From a comparison of amplitudes of the shortest time constant ($\tau_1$ = 38-62 ps, Table 5.3) it becomes evident that the efficiency of electron transfer from the monomeric state of ICG (emission wavelength 818 nm) to ZnO is significantly larger quantity

than that from the dimeric state (emission wavelength 708 nm) leading to significantly shortened average fluorescence lifetime of the ICG-ZnO nanohybrid relative to ICG.

***Table 5.3.*** *Fluorescence lifetime of ICG and ICG-ZnO nanohybrid in DMSO*

| System | Emission wavelength (nm) | $\tau_1$ (ns) | $\tau_2$ (ns) | $\tau_3$ (ns) | $\tau_{avg}$ (ns) |
|---|---|---|---|---|---|
| ICG | 818 | 0.124 ± 0.01 (16%) | 0.908 ± 0.04 (84%) | | 0.783 |
| ICG-ZnO | 818 | 0.038 ± 0.005 (51%) | 0.262 ± 0.02 (26%) | 0.576 ± 0.03 (23%) | 0.220 |
| ICG | 708 | 0.203 ± 0.02 (29%) | 1.593 ± 0.05 (71%) | | 1.190 |
| ICG-ZnO | 708 | 0.062 ± 0.01 (33%) | 0.494 ± 0.03 (38%) | 1.042 ± 0.04 (29%) | 0.510 |

*{$\tau_1$, $\tau_2$, and $\tau_3$ are decay components associated with fluorescence transients and their amplitudes are represented within parentheses next to them. $\tau_{avg}$ is mean fluorescence lifetime calculated by $\tau_{avg} = a_1\tau_1 + a_2\tau_2 + a_3\tau_3$ where $a_i$s are amplitudes corresponding to $\tau_i$s and $\sum a_i = 1$.}*

The existence of a highly efficient photo-induced electron transfer from the monomeric form of ICG to the conduction band of ZnO enhances the possibility of photoinduced ROS generation by the ICG-ZnO nanohybrid. ROS is monitored by a well-known non-fluorescent marker dichlorofluorescein (DCFH) which is oxidised to fluorescent dichlorofluorescein (DCF) by ROS exhibiting an emission near 520 nm upon excitation at 488 nm [31-33]. When oxidation of DCFH in the dark is monitored for 9 minutes separately in presence of the nanohybrid, ICG and ZnO no change in emission intensity at 520 nm is observed (Figure 5.6.c) indicating the absence of ROS. On exposure to red light for 21 minutes, the emission intensity at 520 nm is significantly enhanced by an order of magnitude for the nanohybrid relative to the controls (Figure 5.6.c). The significant enhancement in emission intensity at 520 nm due to formation of DCF is consistent with significant amount of ROS generation by the ICG-ZnO nanohybrid due to photo- induced interfacial charge transfer. During the charge transfer process, the separated free electrons and the holes generate a

large amount of ROS (free electron combat with oxygen molecule to generates superoxide and holes generates hydroxyl radical from water molecule) from neighbouring oxygen and water molecules [34-36].

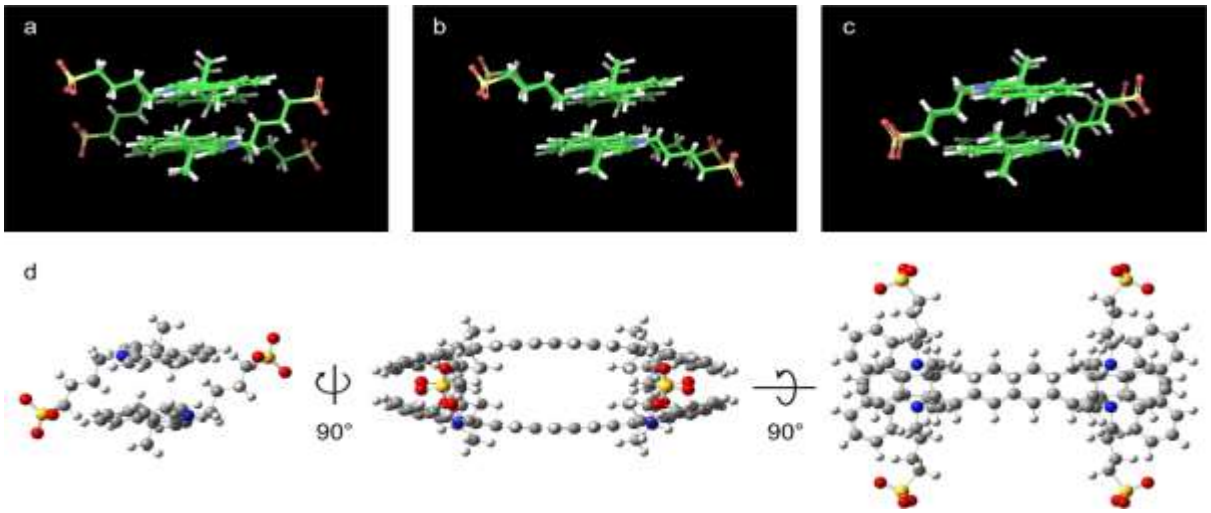


***Figure 5.7.*** *Possible conformations of ICG dimer optimized in classical OPLS forcefield (a, b, c). Lowest energy conformation of ICG dimer (c) further optimized with DFT (d).*

Thus, the limitation of ICG in producing negligible amount of ROS (Figure 5.6.c) is overcome by formulation of the ICG-ZnO nanohybrid which generates significant amount of ROS upon photoexcitation.

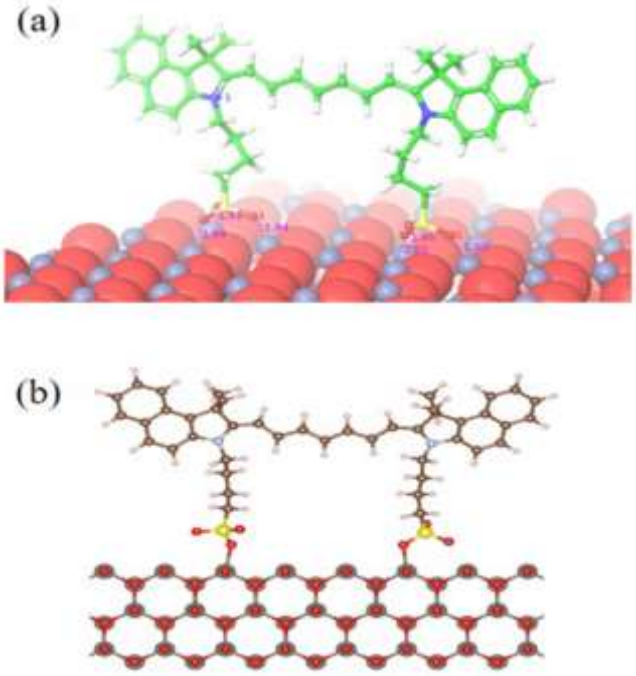


***Figure 5.8****. Lowest energy conformation of ICG on the nonpolar surface of ZnO as obtained by MD simulation (a) followed by DFT optimization (b).*

This observation manifests the scope of using the ICG-ZnO nanohybrid as a potential photodynamic agent for therapeutic action. Classical molecular dynamics (MD) simulations and quantum mechanical approaches were used to probe the dimerization of ICG, stability of the dimer on the ZnO surface, nature of binding of ICG to the ZnO surface, and the electronic transitions involved in the nanohybrid.

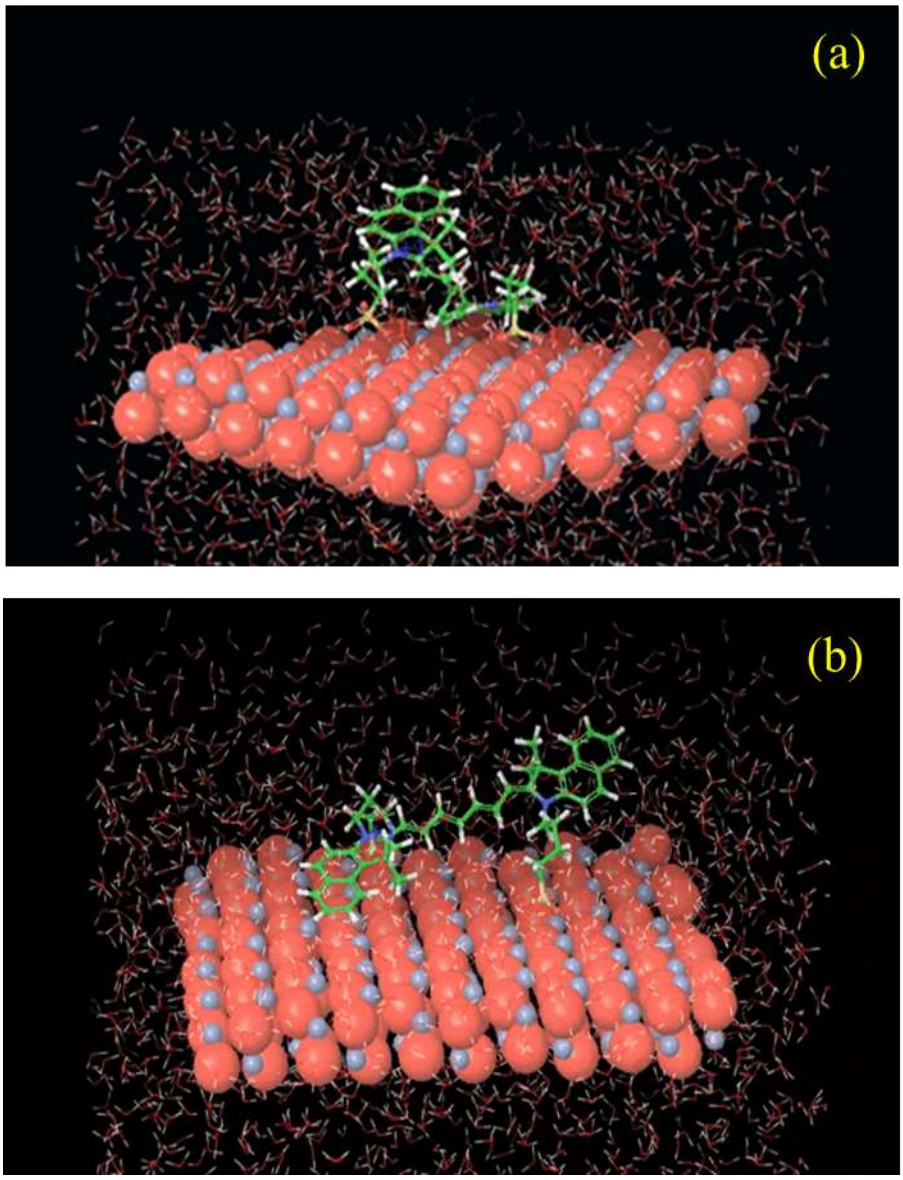


***Figure 5.9.*** *(a) MD simulation of cis-ICG on Zn terminated polar {0001} surface of ZnO. (b) MD simulation of trans-ICG on Zn terminated polar {0001} surface of ZnO.*

Among the three possible dimer conformations indicated by MD simulation (Figure 5.7.a-c) geometry of the lowest energy conformation (Figure 5.7.c) was optimized using DFT and is shown in Figure 5.7.d. The binding energies obtained from

molecular docking of ICG on different ZnO surfaces (Table 5.4) suggests that binding of ICG is more favourable on the non-polar zig-zag surface of ZnO {10-10}.

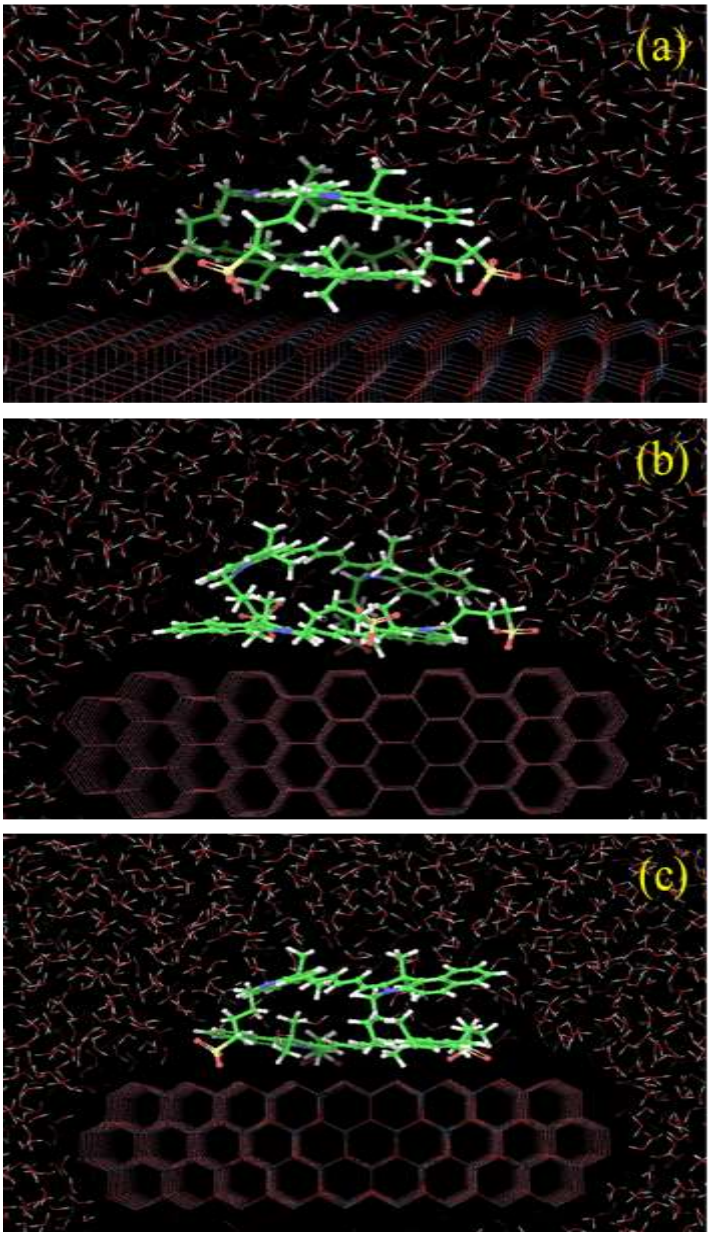


***Figure 5.10.*** *(a) ICG dimer breaks down on the polar ZnO surface.(b) ICG dimer remains longer on the non-polar armchair end of ZnO.(c) ICG dimer remains longer on non-polar zig-zag end of ZnO.*

ICG can also bind to the Zn terminated polar surface {0001}, however, binding is energetically less favourable on the O terminated polar surface. MD simulation shows that ICG binds to the ZnO surface *via* the sulfate groups (Figure 5.8) which is Columbic in nature. Further density functional studies show a covalent linkage between the Zn and the O atom of the sulfonate groups with a bond distance of 2.05 Å whereas Zn-O bond distances in the crystal are {2.04, 2.04, 2.04 and 1.80 Å}. On the

ZnO surface both the cis- and the trans- conformers (Figures 5.9.a and 5.9.b) converge to the lowest energy conformer on the nonpolar zigzag surface of ZnO with the aliphatic chain pointing in the same direction. Classical MD simulation further shows that the dimer readily breaks down to monomers on the polar ZnO surface (Figure 5.10.a).

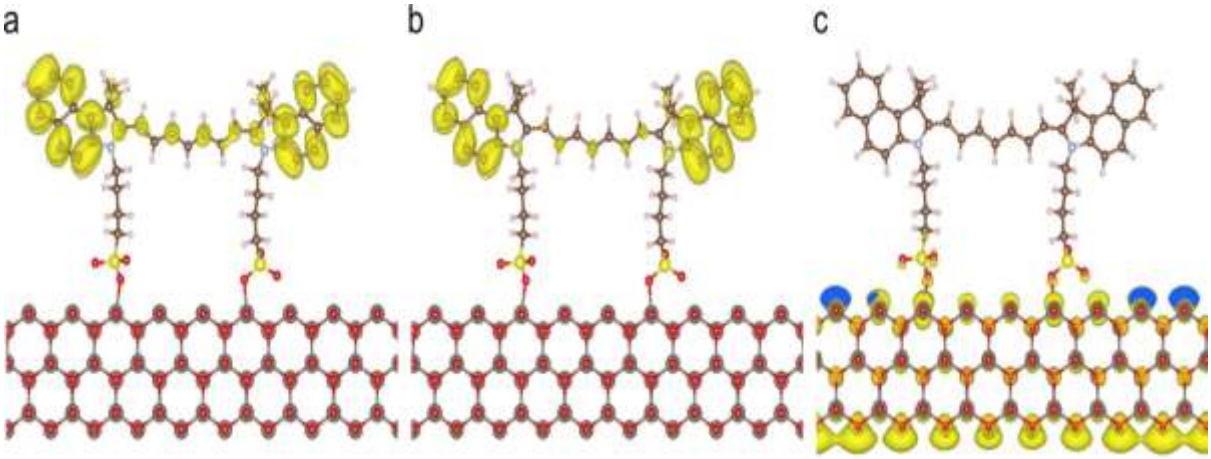


***Figure 5.11****. Band decomposed electron densities of the ICG-ZnO nanohybrid: Band 1006 (a) and 1007 (b) correspond to the LUMO+1 and LUMO+2 of ICG, respectively. Band 1005 (c) corresponds to conduction band of ZnO.*

Whereas, on the other non-polar surfaces, stacking interaction of two ICG monomers remains stable for a longer duration of time (Figure 5.10.b &5.10.c). This corroborates experimental observations showing decreased dimerization of ICG on the ZnO nanosurface.

***Table 5.4:*** *Binding energies as obtained by molecular docking. Units are in kcal/mol*

| ZnO Surface | cis-ICG | trans-ICG |
|---|---|---|
| Non-polar zig-zag end | -12.0 | -11.9 |
| Polar Zn terminated | -11.8 | -12.2 |
| Polar O terminated | -8.9 | -9.3 |

Electron densities of the ZnO bound ICG was further deduced (Figure 5.11) Comparison of the band decomposed electron densities of the nanohybrid to that of free ICG, suggests an excited state electron transfer from {LUMO+1, LUMO+2} of

ICG to the conduction band minimum (CBM) of ZnO which corroborates well with the significantly quenched fluorescence lifetime of the ICG-ZnO nanohybrid relative to the free dye (Table 5.4).

The effect of various concentrations of ICG-ZnO on the growth of *E. Coli* is examined using the colony-forming unit (CFU) assay under dark condition. At a concentration of 1 mg/ml, the inhibition in the bacterial growth is quite significant (Figure 5.12.a). To probe the photodynamic action a concentration of 0.3 mg/ml of the ICG-ZnO nanohybrid has been prepared for incubating the culture of *E. coli* for 3 h in the dark prior to 30 min irradiation of red light.

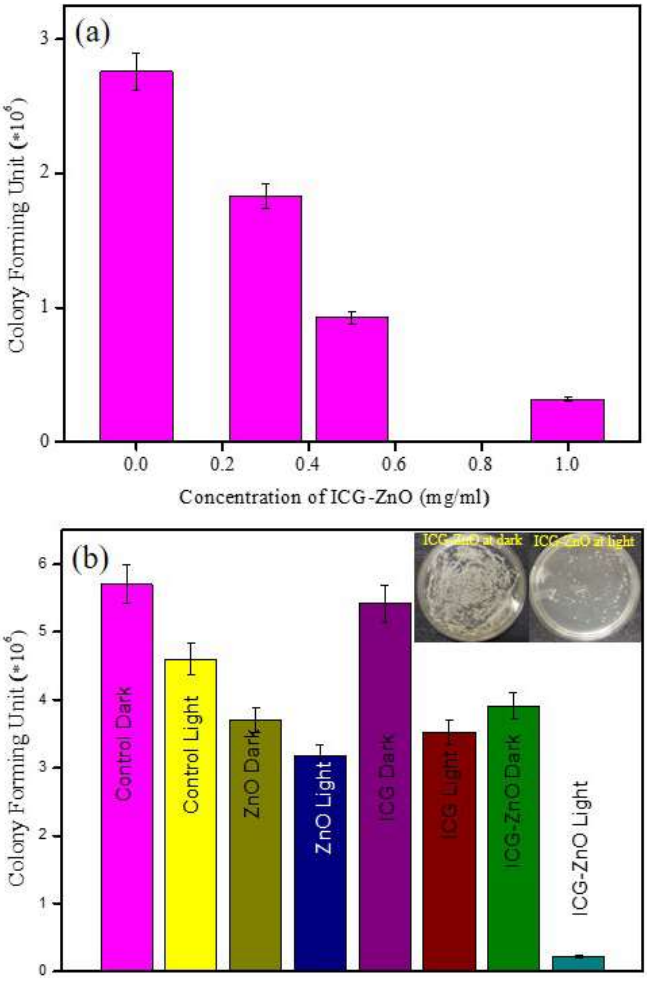


***Figure 5.12.*** *(a) Dose-dependent antibacterial effect of ICG-ZnO at concentrations ranging from 0 to 1 mg/ml on E. coli under dark conditions. (b) Bacterial viability after treatment with 0.3 mg/ml ICG-ZnO in the presence and absence of red-light irradiation (30 min). The inset shows images of E. coli plates treated with ICG-ZnO, before (left) and after (right) red-light irradiation.*

The upper panel of Figure 5.12.b shows the pictures of *E. coli* culture plates treated with the ICG-ZnO nanohybrid in absence and in presence of red-light illumination.

The pictures clearly illustrate the visible changes in the bacterial growth with significantly less number of colonies following photodynamic treatment. There is no antibacterial activity under dark and light-irradiated conditions for the control as well as the ZnO treated sample. In case of ICG-treated samples, the bacterial growth is observed to have decreased by 38% in CFU compared to 96% for the ICG-ZnO nanohybrid treated samples under irradiation with red light. Thus, the inhibition in growth of the bacterial culture for the nano-hybrid is highest (96%) relative to the other controls (Figure 5.12.b).

**5.3. Conclusion:** Target specific drug delivery and the penetration depth of light in biological tissues are key parameters for a superior antimicrobial photodynamic therapy. Herein, we have explored to improve therapeutic potential of ICG as a NIR photosensitizer by functionalization with ZnO nanoparticles (~20 nm, confirmed by TEM analysis). The functionalization of ZnO with ICG is confirmed by both optical spectroscopy tools as well as MD simulations which show binding of ICG on the ZnO surface to occur *via* its sulphate groups. The aggregation experiment of ICG in water and the classical MD simulation show that the dimerization of ICG is decreased on the surface of ZnO. The fluorescence of ICG, especially of the monomer (~818 nm) is significantly quenched in the nanohybrid due to an excited-state electron transfer from ICG to ZnO which is consistent with a significantly reduced fluorescence lifetime of the ICG-ZnO nanohybrid relative to ICG. DFT and TD-DFT studies show the occurrence of an excited state electron transfer from the higher energy orbitals of ICG to the conduction band of ZnO which gives rise to significantly higher efficiency of the ICG-ZnO nanohybrid in generating ROS than the dye itself (ICG). The photodynamic antibacterial activity of the ICG-ZnO nanohybrid is confirmed from the CFU assay on gram-negative bacteria *E. coli*. After incubation of *E. coli* with the nanohybrid, a significant reduction (96%) in CFU was observed upon light irradiation. Overall, the nanohybrid formation prevents the aggregation of ICG and produces a huge amount of ROS than ICG itself. Our studies demonstrate that the ICG-ZnO nanohybrid can be translated into developing NIR light triggered nano-antibiotics based on NIR sensitive cyanine dyes.

# References

[1] J. Dang, H. He, D. Chen, L. Yin, Manipulating tumor hypoxia toward enhanced photodynamic therapy (PDT), *Biomater. Sci.* 5 (2017) 1500.

[2] N. Maeding, T. Verwanger, B. Krammer, Boosting tumor-specific immunity using PDT, *Cancers* 8 (2016) 91.

[3] Y.g. Lu, Y.y. Wang, Y.d. Yang, X.c. Zhang, Y. Gao, Y. Yang, J.b. Zhang, G.l. Li, Efficacy of topical ALA-PDT combined with excision in the treatment of skin malignant tumor, *Photodiagnosis Photodyn Ther.* 11 (2014) 122.

[4] C. Wang, H. Tao, L. Cheng, Z. Liu, Near-infrared light induced *in vivo* photodynamic therapy of cancer based on upconversion nanoparticles, *Biomaterials* 32 (2011) 6145.

[5] L. Tan, A. Wan, X. Zhu, H. Li, Nitric oxide release triggered by two-photon excited photoluminescence of engineered nanomaterials, *ChemComm* 50 (2014) 5725.

[6] C.J. Carling, J.C. Boyer, N.R. Branda, Remote-control photoswitching using NIR light, *J. Am. Chem. Soc.* 131 (2009) 10838.

[7] S. George, M.R. Hamblin, A. Kishen, Uptake pathways of anionic and cationic photosensitizers into bacteria, *Photochem. Photobiol. Sci.* 8 (2009) 78.

[8] S. Mindt, I. Karampinis, M. John, M. Neumaier, K. Nowak, Stability and degradation of indocyanine green in plasma, aqueous solution and whole blood, *Photochem. Photobiol. Sci.* 17 (2018) 1189.

[9] C. Abels, Targeting of the vascular system of solid tumours by photodynamic therapy (PDT), *Photochem. Photobiol. Sci.* 3 (2004) 765.

[10] Z. Wan, H. Mao, M. Guo, Y. Li, A. Zhu, H. Yang, H. He, J. Shen, L. Zhou, Z. Jiang, Highly efficient hierarchical micelles integrating photothermal therapy and singlet oxygen-synergized chemotherapy for cancer eradication, *Theranostics* 4 (2014) 399.

[11] D.B. Tada, M.S. Baptista, Photosensitizing nanoparticles and the modulation of ROS generation, *Front. Chem.* 3 (2015) 33.

[12] W. Bäumler, C. Abels, S. Karrer, T. Weiss, H. Messmann, M. Landthaler, R. Szeimies, Photo-oxidative killing of human colonic cancer cells using indocyanine green and infrared light, *Br. J. Cancer* 80 (1999) 360.

[13] H. Fan, Y. Fan, W. Du, R. Cai, X. Gao, X. Liu, H. Wang, L. Wang, X. Wu, Enhanced type I photoreaction of indocyanine green via electrostatic-force-driven aggregation, *Nanoscale* 12 (2020) 9517.

[14] D.B. Tada, M.S. Baptista, Photosensitizing nanoparticles and the modulation of ROS generation, *Front. Chem.* 3 (2015) 33.

[15] K.R. Raghupathi, R.T. Koodali, A.C. Manna, Size-dependent bacterial growth inhibition and mechanism of antibacterial activity of zinc oxide nanoparticles, *Langmuir* 27 (2011) 4020.

[16] N.S. Blow, R.N. Salomon, K. Garrity, I. Reveillaud, A. Kopin, F.R. Jackson, P.I. Watnick, Vibrio cholerae infection of drosophila melanogaster mimics the human disease cholera, *PLOS Pathog*. 1 (2005) e8.

[17] Z. Daoud, E. Salem Sokhn, K. Masri, K. Cheaito, N. H. Ahmad, G.M. Matar, S. Doron, *Escherichia col*i isolated from urinary tract infections of Lebanese patients between 2005 and 2012: Epidemiology and profiles of resistance, *Front. Med*. 2 (2015) 26.

[18] A. Bera, M.N. Hasan, U. Pal, D. Bagchi, T.K. Maji, T. S. Dasgupta, R. Das, S.K. Pal, Fabrication of nanohybrids toward improving therapeutic potential of a NIR photo-sensitizer: An optical spectroscopic and computational study, *J. Photochem. Photobiol. A* 424 (2022) 113610.

[19] S. Desgreniers, High-density phases of ZnO: Structural and compressive parameters, *Phys. Rev. B* 58 (1998) 14102.

[20] H. V. Berlepsch, C. Böttcher, H-aggregates of an indocyanine Cy5 dye: Transition from strong to weak molecular coupling, *J. Phys. Chem. B* 119 (2015) 11900.

[21] H. Mustroph, K. Reiner, J. Mistol, S. Ernst, D. Keil, L. Hennig, Relationship between the molecular structure of cyanine dyes and the vibrational fine structure of their electronic absorption spectra, *ChemPhysChem* 10 (2009) 835.

[22] R. Philip, A. Penzkofer, W. Bäumler, R. Szeimies, C. Abels, Absorption and fluorescence spectroscopic investigation of indocyanine green, *J. Photochem. Photobiol. A* 96 (1996) 137.

[23] B. Bahmani, D. Bacon, B. Anvari, Erythrocyte-derived photo-theranostic agents: Hybrid nano-vesicles containing indocyanine green for near infrared imaging and therapeutic applications, *Sci. Rep.* 3 (2013) 2180.

[24] B. Jung, V.I. Vullev, B. Anvari, Revisiting indocyanine green: Effects of serum and physiological temperature on absorption and fluorescence characteristics, *IEEE J. Sel. Top. Quantum Electron.* 20 (2013) 149.

[25] G. Pistolis, I. Balomenou, Cyclodextrin cavity size effect on the complexation and rotational dynamics of the laser dye 2, 5-diphenyl-1, 3, 4-oxadiazole: From singly occupied complexes to their nanotubular self-assemblies, *J. Phys. Chem. B* 110 (2006) 164288.

[26] A. Bera, D. Bagchi, S.K. Pal, Improvement of Photostability and NIR Activity of cyanine dye through nanohybrid formation: Key information from ultrafast dynamical studies, *J. Phys. Chem. A* 123 (2019) 7550.

[27] J. Patwari, A. Chatterjee, S. Sardar, P. Lemmens, S.K. Pal, Ultrafast dynamics in co-sensitized photocatalysts under visible and NIR light irradiation, *Phys. Chem. Chem. Phys.* 20 (2018) 10418.

[28] D. Bagchi, V.S. Rathnam, P. Lemmens, I. Banerjee, S.K. Pal, NIR-Light-Active ZnO-Based Nanohybrids for Bacterial Biofilm Treatment, *ACS omega* 3 (2018) 10877.

[29] S.E. Koops, B.C. O'Regan, P.R. Barnes, J.R. Durrant, Parameters influencing the efficiency of electron injection in dye-sensitized solar cells, *J. Am. Chem. Soc.* 131 (2009) 4808.

[30] N.A. Anderson, T. Lian, Ultrafast electron transfer at the molecule-semiconductor nanoparticle interface, *Annu. Rev. Phys. Chem.* 56 (2005) 491.

[31] D. Bagchi, S. Chaudhuri, S. Sardar, S. Choudhury, N. Polley, P. Lemmens, S.K. Pal, Modulation of stability and functionality of a phyto-antioxidant by weakly interacting metal ions: Curcumin in aqueous solution, *RSC Adv.* 5 (2015) 102516.

[32] A. Chatterjee, P. Kar, D. Wulferding, P. Lemmens, S.K. Pal, Flower-Like BiOI Microspheres Decorated with Plasmonic Gold Nanoparticles for Dual Detoxification of Organic and Inorganic Water Pollutants, *ACS Appl. Nano Mater.* 3 (2020) 2733.

[33] S.A. Ahmed, M.N. Hasan, D. Bagchi, H.M. Altass, M. Morad, R.S. Jassas, A.M. Hameed, J. Patwari, H. Alessa, A. Alharbi, Combating essential metal toxicity: Key information from optical spectroscopy, *ACS omega* 5 (2020) 15666.

[34] W. He, H.-K. Kim, W.G. Wamer, D. Melka, J.H. Callahan, J.J. Yin, Photogenerated charge carriers and reactive oxygen species in ZnO/Au hybrid nanostructures with enhanced photocatalytic and antibacterial activity, *J. Am. Chem. Soc.* 136 (2014) 750.

[35] W. He, H. Wu, W.G. Wamer, H.-K. Kim, J. Zheng, H. Jia, Z. Zheng, J.J. Yin, Unraveling the enhanced photocatalytic activity and phototoxicity of ZnO/metal hybrid nanostructures from generation of reactive oxygen species and charge carriers, *ACS Appl. Mater. Interfaces* 6 (2014) 15527.

[36] Z. Kang, X. Yan, L. Zhao, Q. Liao, K. Zhao, H. Du, X. Zhang, X. Zhang, Y. Zhang, Gold nanoparticle/ZnO nanorod hybrids for enhanced reactive oxygen species generation and photodynamic therapy, *Nano Res.* 8 (2015) 2004.

# Chapter 6

# Synthesis and Characterization of a Nanohybrid Through Surface Sensitization of an Oxide Material with Agriculturally-Relevant Organic Ligand for Sustained Delivery of Micronutrient

**6.1. Introduction:** Zinc (Zn) is a plant micronutrient required only in small quantities for optimum plant yield [1]. Thus excess delivery of micronutrients leads to essential nutrient loss. Despite that, nearly all conventional micronutrient sources are used as water-soluble salts or chelated forms of micronutrients [2, 3]. Some of these formulations undergo fast dissolution and release of Zn which eventually leads to leaching-loss and run-off during high rainfall. The use of conventional Zn sources can therefore be seen as both economically and environmentally inefficient allocation of resources with far-reaching social implications since approximately 49% of the arable soils of the world are Zn deficient [4]. Intake of food grains grown in Zn-deficient soils is a major contributor to prevalence of Zn deficiency in humans which is among the top five micronutrient deficiencies affecting one-third of the world's population [5]. Zinc deficiency in crop (eg., wheat) plants poses a formidable challenge to global public health which has led to the development of biofortification [6] and ferti-forticitaion [7] methods of grain Zn enrichment. The effectiveness of Zn fertilizers in Zn deficient soils depends on the solubility of the Zn source in soil [4] apparently due to the significant correlation between water-soluble fractions of Zn and Zn bioavailability to plants. However, regardless of the total or water-soluble fractions of Zn micronutrient, sustained and slow release of Zn from the Zn source would be of utmost importance to achieve high nutrient-uptake efficiency in Zn-deficient soil systems [1, 8].

Aqueous colloidal dispersions of copper (Cu) and Zn nanoformulations have been utilized to stimulate crop yield [4, 9-11]. The solubility and dissolution (release)

kinetics of zinc oxide (ZnO) nanoparticles (NPs) have been utilized as a source of Zn in Zn-deficient environments [4]. Herein, the high surface to volume ratio of ZnO NPs (compared to bulk ZnO) was exploited in order to achieve high dissolution rate as according to the Noyes-Whitney equation, larger interface promotes dissolution *via* diffusion of dissolved ions away from the particle [4]. Furthermore, ZnO NP is an amphoteric oxide [12]; hence it reacts with both $H^+$ and $OH^-$ ions to form hydrated Zn(II) cation in acids and zincates ($[Zn(OH)_3]^-$, $Zn(OH)_4]^{2-}$ ) in alkalis. At neutral pH, ZnO NPs become more stable and sparingly soluble in water. This unique solubility feature of ZnO NPs has been exploited by applying as Zn nanoformulation typically by incorporating it into or coating onto macronutrient fertilizers for cost-effective delivery and uniform distribution of the small amount of Zn in soil [4]. However, the outcome was not promising due to inhibitive effect of macronutrient fertilizer on the dissolution rate of ZnO NP. Consequently, ZnO NPs led to similar plant growth as bulk ZnO. In other cases, it led to slower development of (soybean) plants [13]. Thus an urgent requirement for smart micronutrient delivery systems exists which requires convergence of ideas on NP surface engineering, interface and colloid science and sustainable natural resources [14]. To control ZnO NP dissolution, particle size reduction is a pathway that has been explored previously [15] and it was found that the rate of dissolution increases with decrease in NP size. Nonetheless, NP size reduction may enhance the surface reactivity and hence the toxicity of NPs [16]. The other plausible mechanism is NP surface engineering with surface functional groups [17]. This pathway could be environmentally more sustainable as it may help gain better control over NP dissolution without significantly increasing the toxicity of the system. But, despite having enormous potential to improve micronutrient formulations [4], experimental evidence of the impact of ZnO NP surface modifications is scarce. Surface chemistry of NPs can be modified by top down (physical) and bottom up (chemical) methods using surface coatings or functional groups. Previous research has demonstrated that a solubilizing layer with multiple functional (hydroxyl (–OH ) and carboxylic ($–COO^-$ )) groups can modify the interaction of NPs with water (and biological macromolecules) [18]. For example, functionalization with biocompatible citrate

ligand forms a bi-dentate conjugation between two $COO^-$ oxygen and $Mn^{3+}$ developing a thin solubilizing shell around manganite NP [18].

When released into the environment, nanomaterials (NMs) can acquire a natural coating of organic substances. In aquatic ecosystems, dissolved organic material (DOM) is present at concentrations ranging from 0.1 to 10 $mgL^{-1}$ depending on the biogeochemical conditions and climate [19]. Humic substances, including humic acids (HA) and fulvic acids (FA), constitute one of the most important components of DOM. DOM concentrations are typically orders of magnitude higher than NMs and so are likely to substantially reform the surface properties and behaviors of NMs. Adsorbed macromolecules can significantly alter aggregation, NM-bio interactions, biological uptake, fate, transport, and distribution of NPs in the environment [20]. For example, adsorption of polymeric coatings of HA or FA can lead to the formation of heterogeneous polymer-NOM (natural organic matter) layers [20]. Such coatings generally decrease the attachment of NMs to clay surfaces, resulting in greater mobility in the environment [21]. Additionally, humic acids are regarded as supramolecular assemblies of several thousand molecules of high diversity and complexities [22]. Humic acid acts like an extended π-conjugated multi-chromophoric system in which the delocalized π-electrons of chromophores undergo light-induced electronic transition from ground to excited state. Interactions of HA with sunlight are important drivers for various reactions that control metal speciation and surface chemistry of colloids [23]. Amalgamation with semiconductor nanoparticles can cause significant shifts in electronic delocalization through inter and intra molecular cross-talking. Apart from light, external stimuli such as pH, presence of ions can affect HA-functionalized NPs much differently compared to the typical functionalizing agents deployed for engineering NP surfaces [24]. It is noteworthy in this context that natural organics strongly influence, and in some cases govern the behavior of engineered NPs by means of replacement of capping agent and/or overcoating the NP surface with HA [25]. Such alteration in the behavior of NPs in natural systems has brought about a new appreciation of the roles these natural organics play in fundamental processes at the water-mineral-

microbe interface [23]. This study reports the development of a sustained Zn micronutrient delivery system by adopting a bottom-up fabrication methodology (Scheme 6.1) to engineer the surface of ZnO NPs in a facile route at room temperature.


***Scheme 6.1.*** *Surface modification of ZnO NPs for sustained release of Zn (II).*

Large-sized naturally occurring HA ligand and a relatively smaller biologically relevant citrate ligand representing a subunit of the large macromolecule were chosen for molecular functionalization of ZnO NP. Humic substances are heterogeneous mixtures of high molecular weight aliphatic and aromatic organic compounds that are rich in oxygen containing functional groups (e.g., -COOH, phenolic and/or enolic –OH, and quinolic C=O) [26]. On the other hand, citrate is a biocompatible ligand comprising of –COOH and -OH groups [27]. Surface modification is expected to occur through linkages between the reactive functional groups of organic ligands and surface defect states of ZnO NP. The as-synthesized nanohybrids were characterized using electron microscopic and diffraction methods. Steady and time-resolved fluorescence spectroscopy methods were employed to confirm molecular cross-interaction at the NP-ligand interface. The water-stability and dissolution of nanohybrids were evaluated under various environmentally relevant conditions using UV-Visible spectroscopy. Finally, the bioavailability of Zn is validated by investigating the effects of nanoformulations on the seed germination and growth of seedlings of wheat (*Triticum aestivum*) plant**.**

## 6.2. Results and Discussion:

**6.2.1. Surface Engineered ZnO-Humic/Citrate Interfaces: Photoinduced Charge Carrier Dynamics and Potential Application for Smart and Sustained Delivery of Zn Micronutrient [28]:** Transmission electron microscopy (TEM) images were recorded for the characterization of ZnO NPs along with the citrate capped ZnO NPs, and HA capped ZnO nanocrystals prepared by functionalizing ZnO NP surface. Results of TEM analysis revealed the size and morphology of ZnO NP, citrate capped ZnO NP, and HA capped ZnO nanocrystals with an average diameter of 30, 16, and 25 nm (Figure 6.1.a, 6.1.b and 6.1.c). The reduction of particle diameter from 30 to 16 nm due to surface functionalization using citrate ligand can be attributed to ligand 'core etching'[29]. The particle size distribution of uncapped ZnO NP, citrate, and humic-capped NPs are shown in the insets of Figure 6.1.d, 6.1.e and 6.1.f, which clearly indicates the effect of ligands on NP size. This trend in the size of NP after ligand attachment might be due to small size of citrate resulting in greater coverage of NP surface. XRD (X-ray diffraction) patterns of the powdered samples of ZnO recorded pre-and post-functionalization (Figure 6.1.d, 6.1.e and 6.1.f), depicted no significant change in the diffraction patterns. The crystal structure of ZnO (uncapped and capped) is found to be wurtzite in nature. Moreover, the recorded PXRD patterns demonstrate that the products are single phase materials with sharp diffraction peaks indicative of high crystallinity of ZnO NP [30]. A visible color change of ZnO NP (from white to greyish white) was observed after capping with HA. UV-Visible absorption spectra of pure HA, HA capped ZnO NP, and citrate capped ZnO NP are presented in Figure 6.2.a. The UV-Visible absorption spectra of ZnO NP and citrate capped ZnO NP in aqueous media comprise one absorption band centered at 375 nm which corresponds to the characteristic band gap excitation of ZnO NP ($E_g$ = 3.37 eV) [31]. Humic acid shows a broad absorption in the UV and visible region while the spectrum of HA capped ZnO NP displays the characteristics of both ZnO NP and HA. Steady state and picosecond resolved fluorescence emission studies were used to monitor photoinduced carrier dynamics at the nanoheterojunction interfaces.

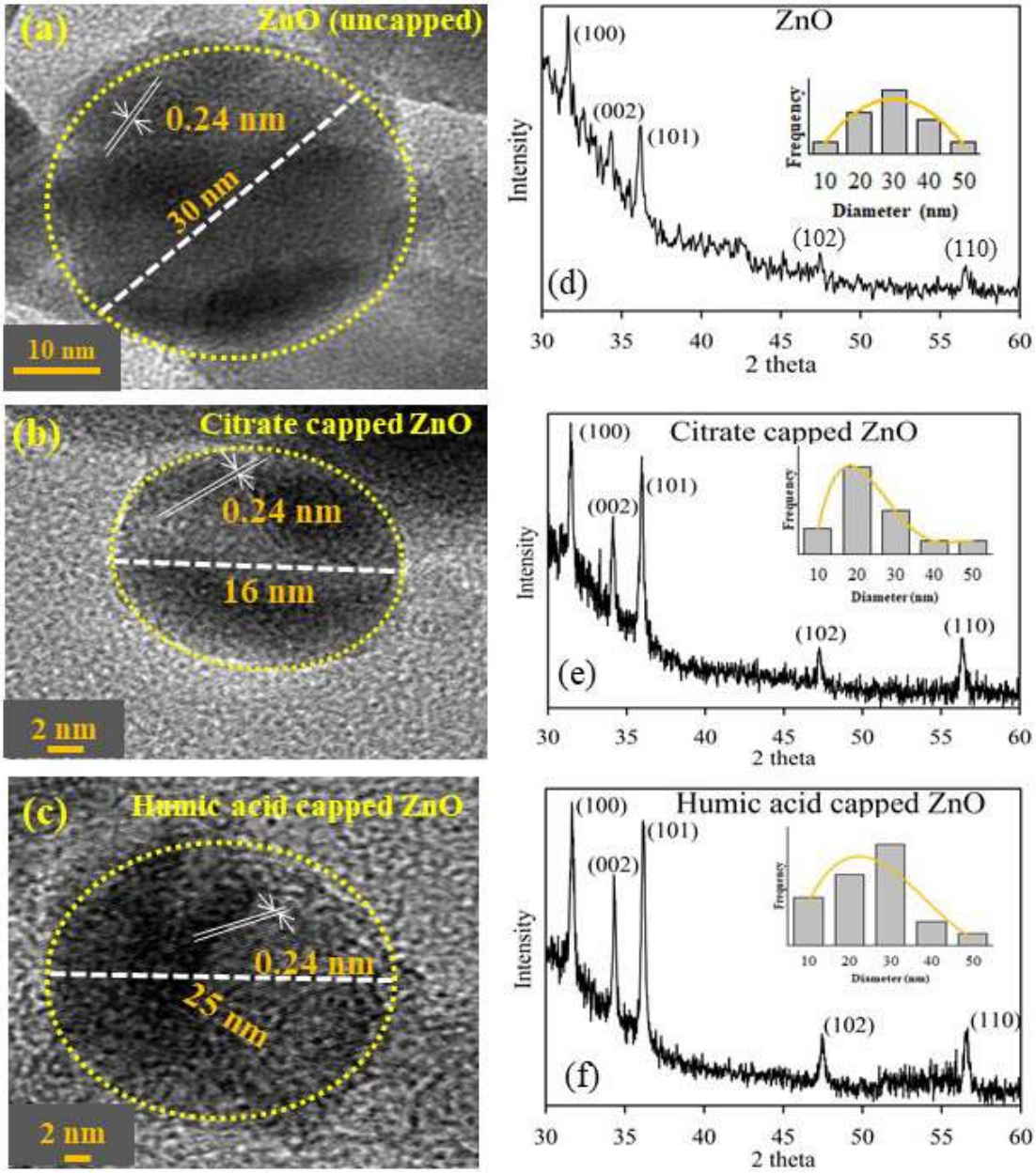


***Figure 6.1.*** *HRTEM images of (a) 30 nm ZnO (uncapped), (b) Citrate-capped ZnO, and (c) Humic acid-capped ZnO. PXRD patterns of (d) 30 nm ZnO (uncapped), (e) Citrate-capped ZnO, and (f) Humic acid-capped ZnO. Insets of Figure 6.1d, 6.1e and 6.1f depict nanoparticle size distribution pattern as obtained from TEM for ZnO (d), citrate capped ZnO (e), and humic capped ZnO (f).*

Room temperature PL spectra of citrate capped ZnO NP reveals a sharp emission peak at 375 nm upon excitation at 270 nm (Figure 6.2.b) representing band gap emission. Additionally, two relatively weaker emission peaks are observed at 495 nm and 550 nm upon excitation at 370 nm (Figure 6.2.c). The latter two peaks are likely due to the recombination of electron from the conduction band with a deep electron trapping center of $V_o^{++}$, termed as an oxygen vacancy state [31]. The emission band around 550 nm occurs from defect states near the surface layer while

the shorter wavelength 495 nm emission occurs from defects near the bulk of the nanoparticles [31]. Inset of Figure 6.2.c shows the excitation spectra at the detection wavelength of 550 nm.

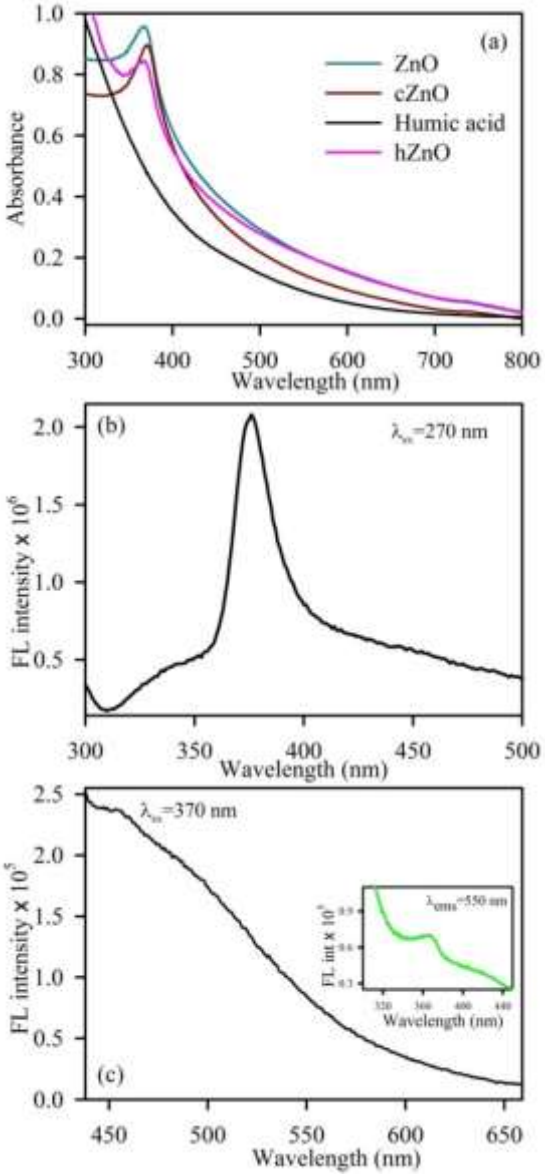


***Figure 6.2.*** *(a) UV-Visible absorption spectra of ZnO (cyan), citrate-capped ZnO (brown), humic acid (black), and humic acid-capped ZnO (pink) (b) Fluorescence spectra of citrate-capped ZnO at day 0 at excitation wavelength of 270 nm (c) Fluorescence spectra of citrate-capped ZnO at day 0 at the excitation wavelength was at 370 nm. Inset shows the excitation spectra ($\lambda_{em}$ = 550 nm).*

PL emission spectra of HA depicts a strong dependence on the excitation wavelength as shown in Figure 6.3.a. The emission peak gets red shifted from 440 nm to 550 nm as excitation wavelength changes from 250 nm to 500 nm. This indicates the presence of multiple emitting states associated with the wide variety of

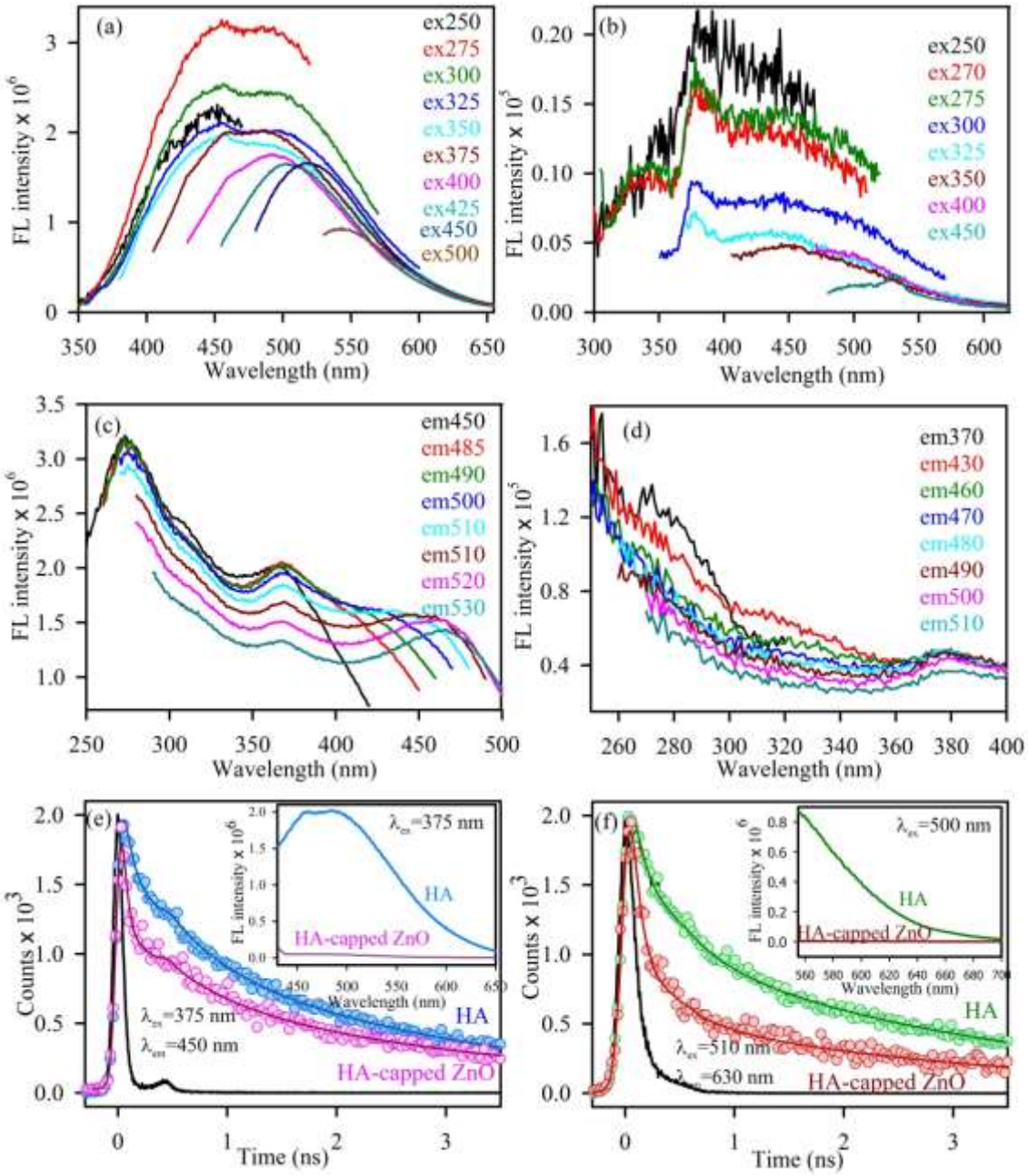


***Figure 6.3.*** *(a) Fluorescence emission spectra of humic acid taken at the interval of 25 nm excitation wavelength from 250 to 550 nm. (b) Fluorescence emission spectra of humic acid-capped ZnO at excitation wavelengths ranging from 250 to 450 nm. (c) Fluorescence excitation spectra ($\lambda_{em}$ = 450 to 530 nm) of humic acid, (d) Fluorescence excitation spectra ($\lambda_{em}$ = 370 to 510 nm) of humic acid-capped ZnO. (e) Picosecond-resolved fluorescence transients (excited at 375 nm) of humic acid (blue) and humic acid-capped ZnO (pink) collected at 450 nm, (f) Picosecond-resolved fluorescence transients (excited at 510 nm) of humic acid (blue) and humic acid-capped ZnO (pink) collected at 630 nm. Inset of (e) shows fluorescence spectra of humic acid (blue), humic acid capped ZnO (pink). The excitation wavelength was at 375 nm. Inset of (f) shows fluorescence spectra of humic acid (green), humic acid capped ZnO (red). The excitation wavelength was at 500 nm.*

conjugation in different segments of oligomeric and polymeric chains of HA molecule [32, 33]. Previous literature reporting excitation-emission matrix of DOM

samples collected from various aquatic environments revealed co-presence of more than ten fluorophores representing multiple redox states and degree of conjugation [34]. In contrast, the emission spectrum of HA capped ZnO NP depict a quenching phenomenon and excitation-independent emission (Figure 6.3.b). The excitation spectra of HA at different detection wavelengths reveal a maximum at 320 nm and 375 nm which is consistent with the absorption spectra of HA (Figure 6.3.c). Additionally, the intensity of the emission peak of HA decreases considerably post-attachment to NP surface, which clearly depicts strong electronic interaction between HA and ZnO NP. Moreover, the emission spectrum of HA capped ZnO illustrates a peak at 530 nm upon excitation at 450 nm likely due to extended conjugation in the polymeric chain [33]. Previous report suggests that HA can sensitize photoredox transformation of toxic chromium (Cr(VI)) to Cr(III)) [35] but the detailed mechanism of photo-initiated interfacial electron transfer has not been reported. The excitation spectrum of HA capped ZnO NP (Figure 6.3.d) depicts quenching behavior and comprises the characteristics of both HA and ZnO NP.

Picosecond-resolved fluorescence decay of HA and HA capped ZnO NP were measured upon excitation with 375 nm and 510 nm laser, and monitored at wavelengths of 450 nm and 630 nm respectively. The decay curve of HA capped ZnO NP shows significant shorter lifetime as compared to HA (Figure 6.3.e and 6.3.f). The observed decrease in lifetime can be accredited to the electron transfer process from HA to ZnO NPs. Inset of Figure 6.3.e and 6.3.f shows the room temperature PL spectrum of HA alone and HA capped ZnO NP upon excitation at 375 nm and 510 nm which clearly depicts that the intensity of the emission of HA decreases markedly post-attachment to NP surface. The fitting parameters after exponential fitting of the decay curves (listed in Table 6.1) shows the presence of faster components (40 ps and 30 ps at excitation wavelength of 375 nm) in HA-capped ZnO NP system than HA (100 ps and 85 ps at excitation wavelength of 510 nm). Thus we anticipate that electronic interaction and energy level rearrangement takes place at the nanoheterojunctions, signifying a unique interfacial phenomenon at NP-organic interface.

***Table 6.1.*** *Picosecond-resolved fluorescence transient lifetime*

| **Systems (ex-375-ems-450)** | **$\tau_1$ (ps)** | **$\tau_2$ (ps)** | **$\tau_3$ (ps)** | **$\tau_{avg}$ (ps)** |
|---|---|---|---|---|
| HA | 100 (39.9) | 882 (33.8) | 3773 (26.2) | 1327.5 |
| ZnO-HA | 40 (70.8) | 550 (15.0) | 3047 (14.2) | 644.0 |
| **Systems (ex-510-ems-630)** | | | | |
| HA | 85 (67.4) | 900 (16.2) | 4273 (16.3) | 900.6 |
| ZnO-HA | 30 (90.7) | 655 (4.7) | 3965 (4.5) | 238.7 |

Having examined the key surface attributes and interfacial charge dynamics, we evaluated the dissolution characteristics of nanohybrids under physiologically relevant pH levels. Comparison of the water-stability kinetics of ZnO NP and nanohybrids was carried out by monitoring the UV-Vis absorption maxima at 375 nm, as shown in Figure 6.4.

***Table 6.2.*** *Fitting parameters of dissolution of the nanoparticles*

| **System** | **pH** | **Decay constant* ($sec^{-1}$)** | **Conc. of humic acid ($mgL^{-1}$)** | **Decay constant* ($sec^{-1}$)** |
|---|---|---|---|---|
| **ZnO** | 4 | 0.052 | 1 | 0.005 |
| | 7 | 0.012 | 5 | 0.005 |
| | 12 | 0.107 | 10 | 0.001 |
| **Citrate capped ZnO** | 4 | 0.015 | 1 | 0.002 |
| | 7 | 0.021 | 5 | 0.001 |
| | 12 | 0.063 | 10 | 0.0006 |
| **Humic capped ZnO** | 4 | 0.003 | - | - |
| | 7 | 0.003 | - | - |
| | 12 | 0.014 | - | - |

*{Experimental curves are fitted with single exponential decay with a standard error of less than 10%. *Decay constant is defined as –A/t of the exponential fitting $y = y_0 + Aexp(-x/t)$.}*

Our results revealed distinct effects of surface modification on the dissolution rate of ZnO NP (Figure 6.4.a, 6.4.b and 6.4.c). At pH 4 and 12, citrate functionalized ZnO NP dissolved at a slower rate than ZnO NPs whereas it dissolved faster at pH 7 (Figure 6.4.d, 6.4.e and 6.4.f). The fitting parameters after exponential fitting of dissolution rate curves are listed in Table 6.2. The decrease in the rate of dissolution at acidic and alkaline pH could be attributed to the protection of the NPs by ligand functional

groups which restrict surface amphoteric reactions between the oxide surface and $H^+$ and $OH^-$ ions. The NP surface protection effects are counterbalanced to a certain extent by the reduction of particle size due to 'core etching' by citrate ligand which might have led to the sustained release.

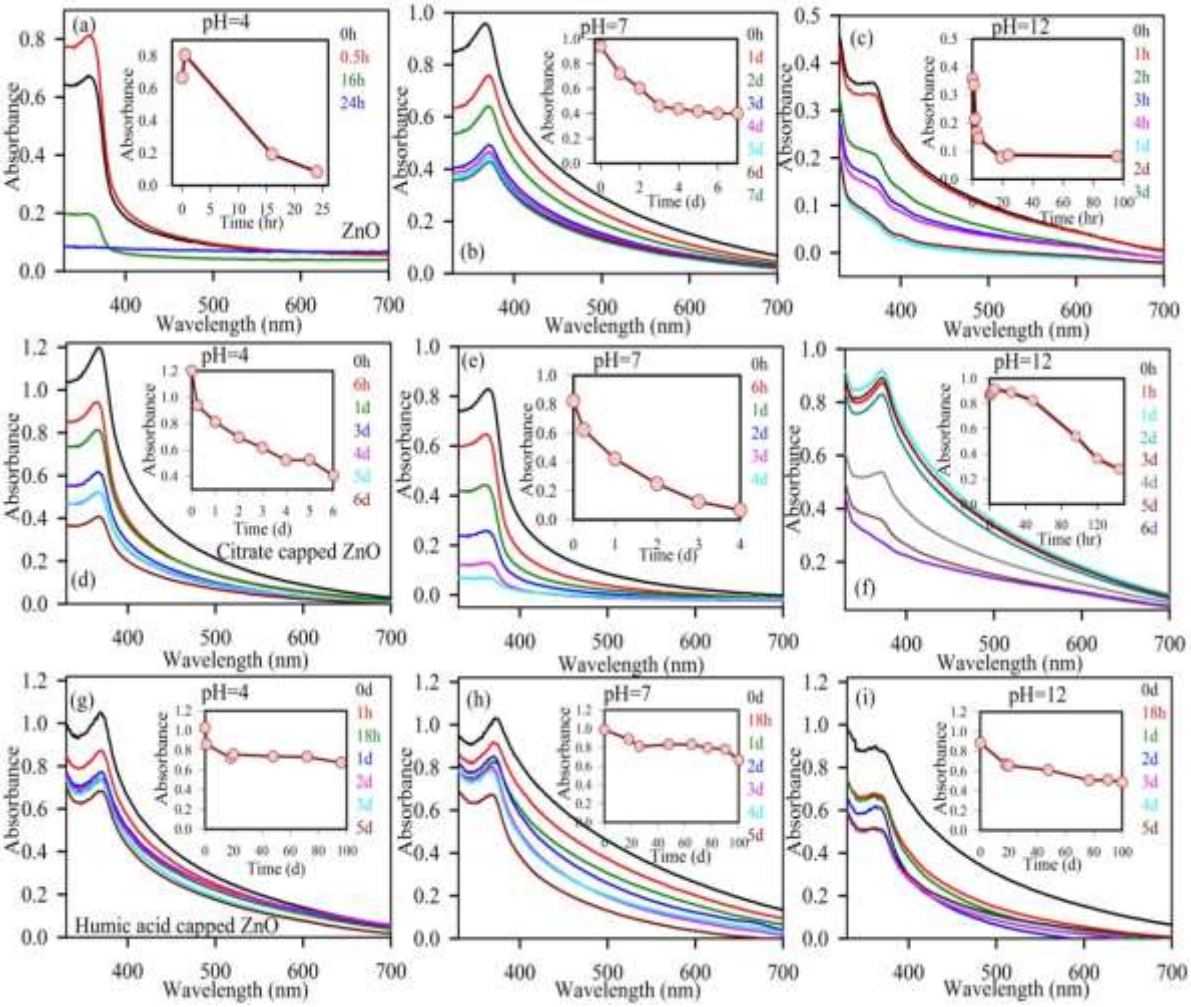


***Figure 6.4.*** *Dissolution characteristics (UV-Visible absorption spectra) of ZnO (top panel), citrate-capped ZnO (middle pannel) and humic acid-capped ZnO (bottom) at (a), (d), and (g) pH 4 (b), (e) and (h) pH 7 and (c), (f), & (i) pH 12. Insets of all figures are representing change in absorbance at 370 nm with variable time window.*

At neutral pH, the enhancement of the dissolution rate is ascribable solely to the reduction of particle size. HA-coated ZnO NP formed relatively stable colloidal suspensions at all pH values (Figure 6.4.g, 6.4.h, and 6.4.i) due to combined surface protection and electrostatic repulsion effects of surface functional groups [36]. The effect of HA coating can be ascribed to the negatively charged adsorbed HA molecules on the NP surface [15]. To better understand the effect of HA on the

dissolution and aggregation of nanohybrids, dissolution characteristics of ZnO NP and citrate capped ZnO were determined at using 1, 5, and 10 ppm HA solution. Figure 6.5 shows the patterns of dissolution depicting greater stability of colloidal suspensions at high concentrations of HA (~10 ppm). The decay constants listed in Table 6.2 depict that HA decreases the dissolution rate and imparts greater stability to the colloids.

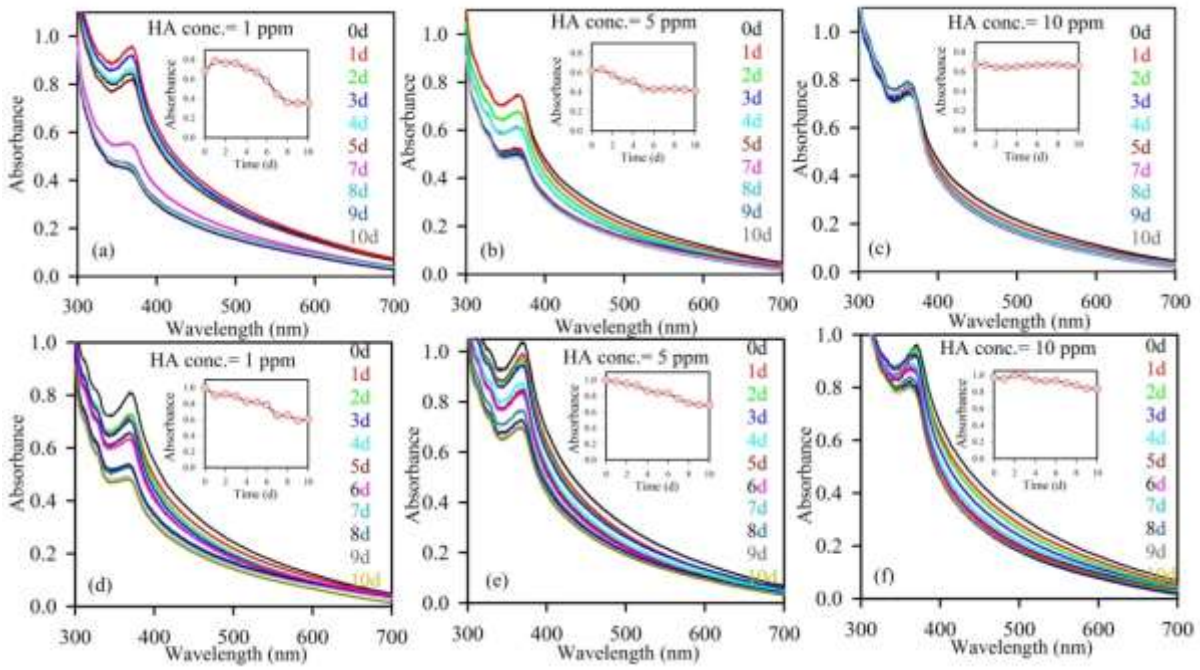


***Figure 6.5.*** *Dissolution characteristics (UV-Visible absorption spectra) of ZnO (top panel) and citrate-capped ZnO (bottom panel) in presence of humic acid at concentrations (a) and (d) 1 ppm (b) and (e) 5 ppm and (c) and (f) 10 ppm. Insets of all figures are representing change in absorbance at 370 nm in a variable time window.*

The colloidal stability increases with increasing concentrations of HA and shows maximum stability in presence of 10 $mgL^{-1}$ HA. Such increase in the colloidal stability could be explained by the increased negative charge density on the surface of NPs [15]. The effects were slightly more pronounced in case of ZnO NP than citrate-capped ZnO NP. Previously, it was conjectured that capping agents become less important determinant of colloidal stability of NPs in presence of NOM [25] likely due to ligand displacement or co-adsorption of HA on the NP surface [37]. In our study, we found that such stabilizations effects are slightly more prominent in case of non-functionalized NPs than functionalized NPs. This could be the result of a balancing act between the stabilization effects and ligand exchange between NOM

and surface-capped NPs. To further establish the sustained Zn delivery mechanism, we have performed reactive oxygen species (ROS) generation assay of citrate capped ZnO NP in dark and white light illuminated conditions at variable times. ZnO NP is known to produce ROS under light due to electron-hole pair production [38]. During the dissolution of citrate functionalized ZnO NP, we observed an increase in photoinduced ROS production (Figure 6.6).

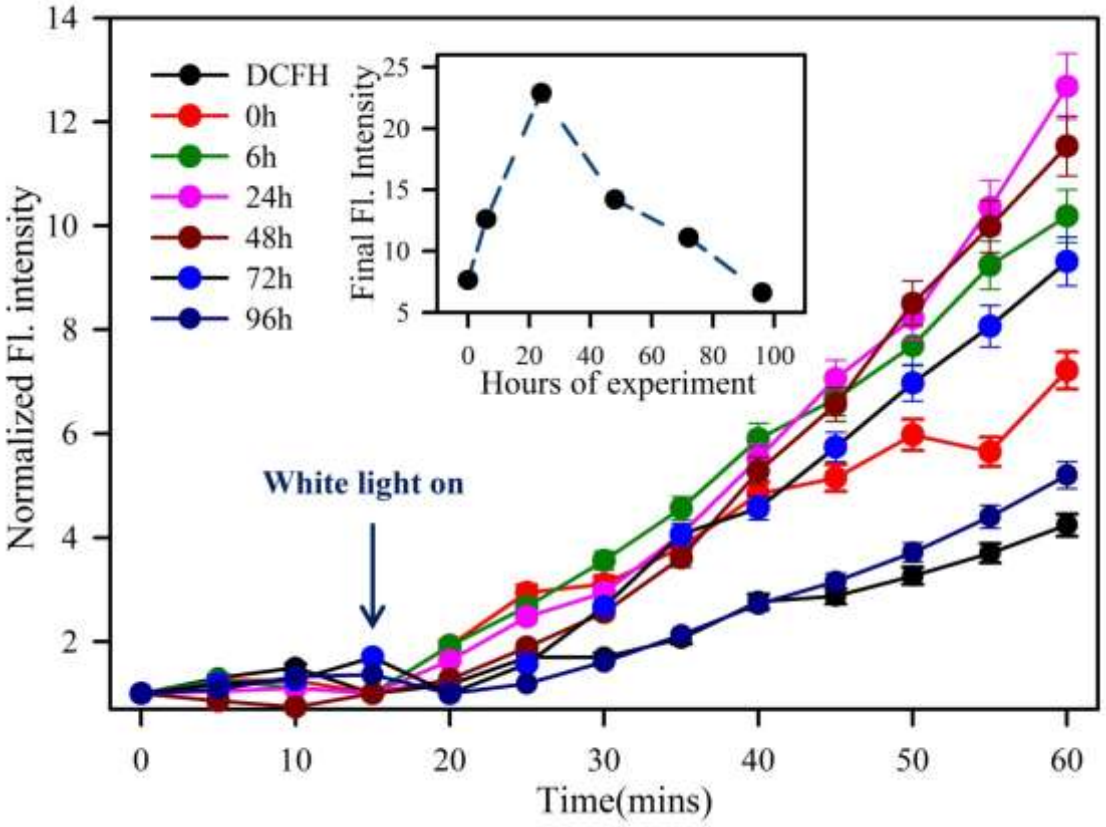


***Figure 6.6.*** *DCFH oxidation with time in presence of citrate functionalized ZnO monitored through the emission intensity at 520 nm. The excitation was at 488 nm. The reaction was monitored under dark for first 15 minutes followed by white light illuminated condition. Inset shows overall ROS generation with variable time window.*

This increase in ROS is found to be time dependent. The ROS production rate gradually decreases as the dissolution process continues. As shown in the inset of Figure 6.6, ROS production tend to increases for first 24 hrs which implies that the size of NP decreases initially increasing effective surface to volume ratio. Then the ROS production decreases which depicts production of $Zn^{2+}$ ions from surface of ZnO NP. This indicates the mechanism behind the dissolution nature of capped ZnO systems. Finally, the effects of nanohybrids on the growth of wheat plant were

investigated. It is known that wheat plants can utilize nanoformulations of ZnO to assimilate Zn for growth and development [39]. We found that wheat plants responded well to the application of citrate-functionalized ZnO as it resulted in better growth than ZnO NPs containing similar Zn levels and control treatments, as shown in Figure 6.7.

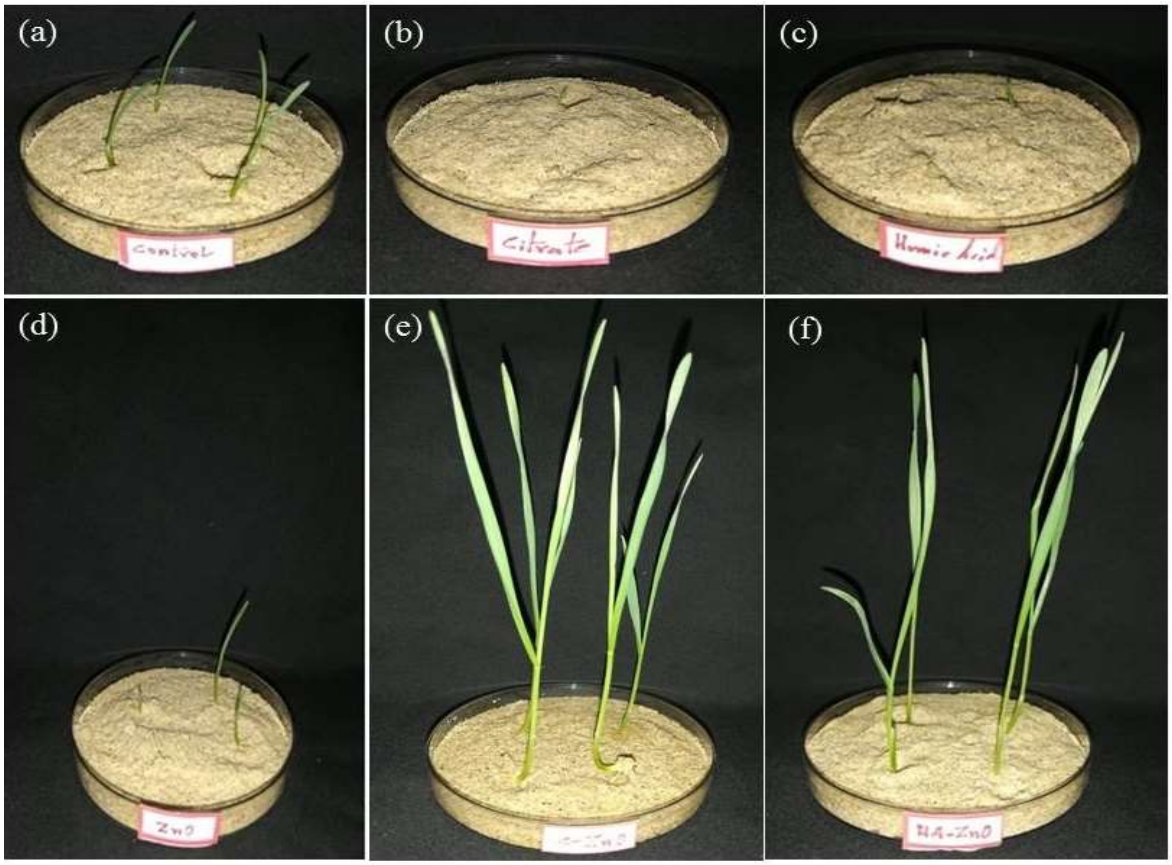


***Figure 6.7.*** *Growth of wheat (Triticum aestivum) plant under (a) control, (b) citrate, (c) humic acid, (d) ZnO NP, (e) citrate-capped ZnO and (f) humic acid capped ZnO treatments on the 8th day after planting the seeds.*

Table 6.3 shows the plant parameters which demonstrate considerable improvementsin plant growth due to the application of nanohybrids. The plant dry weight increased considerably due to the application of citrate capped ZnO NP (220 mg) compared to ZnO (<10 mg). Likewise, shoot and root height increased by a factor of 4 to 4.5 due to the application of citrate capped ZnO NP (12.5 cm, 5.5 cm) as compared to ZnO NP (4.5 cm, 1.3 cm). Results of the inductively coupled plasma/mass spectrometry (ICP-MS) analysis (Table 6.3) of plant digests show

greater concentration of Zn in the root and shoots of plants treated with citrate-capped ZnO NP than other treatments.

***Table 6.3.*** *Effect of surface engineered ZnO-based micronutrient formulations on wheat*

| Treatment | Parameters | | | | | |
|---|---|---|---|---|---|---|
| | Shoot height (cm) | Shoot dry weight (g) | Root length (cm) | Root dry weight (g) | Shoot Zn content (mg/kg) | Root Zn content (mg/kg) |
| Control | 3.5 ± 0.03 | 0.03 ± 0.03 | 1.8 ± 0.02 | 0.05 ± 0.01 | 12.7 ± 0.5 | 13.2 ± 0.5 |
| Citrate only | 0.4 ± 0.03 | ND | 0.75 ± 0.01 | ND | - | - |
| HA only | 0.8 ± 0.04 | ND | 0.5 ± 0.01 | ND | - | - |
| ZnO | 4.5 ± 0.1 | 0.04 ± 0.01 | 1.3 ± 0.02 | 0.02 ± 0.01 | 13.7 ± 0.6 | 25.3 ± 0.5 |
| Citrate capped ZnO | 12.5 ± 0.3 | 0.13 ± 0.01 | 5.5 ± 0.1 | 0.09 ± 0.03 | 19.7 ± 0.5 | 37.4 ± 0.8 |
| HA capped ZnO | 14.0 ± 0.3 | 0.12 ± 0.01 | 5.2 ± 0.2 | 0.06 ± 0.02 | 15.7 ± 0.4 | 24.4 ± 0.4 |

As the nutrient solution used in our study did not have any Zn supplements added to it, the observed differences can be perceived as sole effects of nanoformulations used during seed inoculation. Citrate and HA (alone) treatments showed lesser growth than control treatments. Interestingly, plants receiving HA capped ZnO NP (shoot dry weight (120 mg), shoot and root lengths (14 cm, 5.2 cm)) and citrate capped ZnO NP treatments exhibited comparable growth parameters. For HA capped system, HA simulating natural organic substance, may have stimulated plant growth. Note that ICP results reveal the presence of less amount of Zn in plants (roots) treated with humic capped ZnO NP than citrate capped system. The lesser Zn delivery by the humic capped ZnO NP could be a result of the stabilization effect of HA observed in the dissolution patterns of ZnO in Figure 6.5. Also, the effects of plant root and microbial exudates may influence the stability of organic-NP association [40, 41]. It is noteworthy in this context that earlier reports suggest that HA diminishes the effects of surface capped NP [25]. This trend was not observed in our study. These outcomes are significant first steps towards unfolding the effects of

organically coated NP interfaces rather than individual effects of NPs or humic acid (only) on plant system.

**6.3. Conclusion:** Surface functionalized ZnO-based nanoformulations were investigated for the controlled release of Zn micronutrient in soil, which is a desirable feature for micronutrient delivery systems. The overarching goal was to understand how the formation of the nanoheterojunctions and resultant change in the NP dissolution patterns could favor the Zn micronutrient management. Physicochemical characterization revealed that 'core etching' of ZnO NP by citrate ligand translated into sustained dissolution of ZnO NP over a broad range of environmentally relevant pH values. Key understandings were obtained on the potential change that may occur in the dissolution characteristics of ZnO NP upon interaction with naturally ubiquitous organic ligand. Humic acid imparted slight colloidal stability to aqueous nano ZnO suspensions but humic acid capped ZnO NP led to comparable plant growths. Thus, regardless of the nature of the functionalizing molecule, nanohybrids led to enhanced and sustained plant growth compared to non-functionalized NP. Steady state and picosecond-resolved fluorescence studies revealed efficient photoinduced charge transfer at the interfaces of the HA-coated ZnO NPs. In reflecting the final outcome, this study reveals a promising strategy to reduce resource loss and environmental burden by judicious selection of nutrient forms, which signals the advent of need-based micronutrient delivery systems. Furthermore, we anticipate that NP-induced oxidative damage (ROS) may exert growth inhibiting effects to soil-borne plant pathogens and pests responsible for plant diseases. Therefore the modified ZnO NPs may act as a dual action micronutrient source with synergistic pesticidal effects. This leaves a scope for future study our interpretation of the global cycling of major and trace elements can be informed by further delineating complex reactions governing metal oxide-DOM associations and role of external stimuli in mediating metal speciation and nutrient bioavailability in natural systems. Future studies should investigate photoinduced charge recombination possibilities at the NP-organic interfaces to check the potential of NOM coated NPs as natural light harvesting photovoltaics and photocatalysts.

# References

[1] S. Kabiri, F. Degryse, D.N. Tran, R.C. da Silva, M.J. McLaughlin, D. Losic, Graphene oxide: A new carrier for slow release of plant micronutrients, *ACS Appl. Mater. Interfaces* 9 (2017) 43325.

[2] C. Navizaga, C. Lenzo, H. Zhang, Z. Braziene, V. Paltanavicius, J. Petrauskiene, R. Mazeika, G. Staugaitis, A.M. Sviklas, J. Baltrusaitis, Efficiency evaluation of dairy wastewater derived zinc micronutrient containing sustainable fertilizers, *ACS Sustain. Chem. Eng.* 5 (2017) 6692.

[3] H. Zhang, M. Frey, C. Navizaga, C. Lenzo, J. Taborda, W. Taifan, A. Sadeghnejad, A.M. Sviklas, J. Baltrusaitis, Dairy wastewater for production of chelated biodegradable Zn micronutrient fertilizers, *ACS Sustain. Chem. Eng.* 4 (2016) 1722.

[4] N. Milani, M.J. McLaughlin, S.P. Stacey, J.K. Kirby, G.M. Hettiarachchi, D.G. Beak, G. Cornelis, Dissolution kinetics of macronutrient fertilizers coated with manufactured zinc oxide nanoparticles, *J. Agric. Food Chem.* 60 (2012) 3991.

[5] M.U. Chattha, M.U. Hassan, I. Khan, M.B. Chattha, A. Mahmood, M. Nawaz, M.N. Subhani, M. Kharal, S. Khan, Biofortification of wheat cultivars to combat zinc deficiency, *Front. Plant Sci.* 8 (2017) 281.

[6] I. Cakmak, M. Kalayci, Y. Kaya, A. Torun, N. Aydin, Y. Wang, Z. Arisoy, H. Erdem, A. Yazici, O. Gokmen, Biofortification and localization of zinc in wheat grain, *J. Agric. Food Chem.* 58 (2010) 9092.

[7] A. Dapkekar, P. Deshpande, M.D. Oak, K.M. Paknikar, J.M. Rajwade, Zinc use efficiency is enhanced in wheat through nanofertilization, *Sci. Rep.* 8 (2018) 6832.

[8] M. Zhang, B. Gao, J. Chen, Y. Li, A.E. Creamer, H. Chen, Slow-release fertilizer encapsulated by graphene oxide films, *Chem. Eng. J.* 255 (2014) 107.

[9] M. Ashfaq, N. Verma, S. Khan, Carbon nanofibers as a micronutrient carrier in plants: Efficient translocation and controlled release of Cu nanoparticles, Environ. *Sci. Nano* 4 (2017) 138.

[10] C.O. Dimkpa, J.C. White, W.H. Elmer, J. Gardea-Torresdey, Nanoparticle and ionic Zn promote nutrient loading of sorghum grain under low NPK fertilization, *J. Agric. Food Chem.* 65 (2017) 8552.

[11] T. Prasad, P. Sudhakar, Y. Sreenivasulu, P. Latha, V. Munaswamy, K.R. Reddy, T. Sreeprasad, P. Sajanlal, T. Pradeep, Effect of nanoscale zinc oxide particles on the germination, growth and yield of peanut, *J. Plant Nutr.* 35 (2012) 905.

[12] F. Caillaud, A. Smith, J. Baumard, Morphological differences in ZnO films deposited by the pyrosol technique: Effect of HCl, *J. Eur. Ceram. Soc.* 6 (1993) 313.

[13] S.J. Yoon, J.I. Kwak, W.M. Lee, P.A. Holden, Y.-J. An, Zinc oxide nanoparticles delay soybean development: A standard soil microcosm study, *Ecotox. Environ. Safe.* 100 (2014) 131.

[14] N.R. Scott, H. Chen, H. Cui, Nanotechnology applications and implications of agrochemicals toward sustainable agriculture and food systems, in, *J. Agric. Food Chem.* 66 (2018) 6451.

[15] S. W. Bian, I.A. Mudunkotuwa, T. Rupasinghe, V.H. Grassian, Aggregation and dissolution of 4 nm ZnO nanoparticles in aqueous environments: Influence of pH, ionic strength, size, and adsorption of humic acid, *Langmuir* 27 (2011) 6059.

[16] H. Kaya, F. Aydın, M. Gürkan, S. Yılmaz, M. Ates, V. Demir, Z. Arslan, A comparative toxicity study between small and large size zinc oxide nanoparticles in tilapia (Oreochromis niloticus): Organ pathologies, osmoregulatory responses and immunological parameters, *Chemosphere* 144 (2016) 571.

[17] D. He, M.W. Bligh, T.D. Waite, Effects of aggregate structure on the dissolution kinetics of citrate-stabilized silver nanoparticles, *Environ. Sci. Technol.* 47 (2013) 9148.

[18] A. Giri, N. Goswami, M. Bootharaju, P.L. Xavier, R. John, N.T. Thanh, T. Pradeep, B. Ghosh, A. Raychaudhuri, S.K. Pal, Emergence of multicolor photoluminescence in $La^{0}$. $67Sr^{0}$. $33MnO_3$ nanoparticles, *J. Phys. Chem. C* 116 (2012) 25623.

[19] A. Philippe, G.E. Schaumann, Interactions of dissolved organic matter with natural and engineered inorganic colloids: A review, *Environ. Sci. Technol.* 48 (2014) 8946.

[20] G.V. Lowry, K.B. Gregory, S.C. Apte, J.R. Lead, Transformations of nanomaterials in the environment, in, *Environ. Sci. Technol.* 13 (2012) 6893.

[21] A. Amirbahman, T.M. Olson, Transport of humic matter-coated hematite in packed beds, *Environ. Sci. Technol*. 27 (1993) 2807.

[22] A. Piccolo, The supramolecular structure of humic substances, *Soil Sci.* 166 (2001) 810.

[23] G.R. Aiken, H. Hsu-Kim, J.N. Ryan, Influence of dissolved organic matter on the environmental fate of metals, nanoparticles, and colloids, in, *ACS Publications* 8 (2011) 3196.

[24] V.K. Sharma, J. Filip, R. Zboril, R.S. Varma, Natural inorganic nanoparticles–formation, fate, and toxicity in the environment, *Chem. Soc. Rev.* 44 (2015) 8410.

[25] D.P. Stankus, S.E. Lohse, J.E. Hutchison, J.A. Nason, Interactions between natural organic matter and gold nanoparticles stabilized with different organic capping agents, *Environ. Sci. Technol.* 45 (2010) 3238.

[26] J.J. Mobed, S.L. Hemmingsen, J.L. Autry, L.B. McGown, Fluorescence characterization of IHSS humic substances: Total luminescence spectra with absorbance correction, *Environ. Sci. Technol.* 30 (1996) 3061.

[27] A. Giri, A. Makhal, B. Ghosh, A. Raychaudhuri, S.K. Pal, Functionalization of manganite nanoparticles and their interaction with biologically relevant small ligands: Picosecond time-resolved FRET studies, *Nanoscale* 2 (2010) 2704.

[28] T. Dutta, D. Bagchi, A. Bera, S. Das, T. Adhikari, S.K. Pal, Surface engineered ZnO-humic/citrate interfaces: Photoinduced charge carrier dynamics and potential application for smart and sustained delivery of zn micronutrient, *ACS Sustain. Chem. Eng.* 7 (2019) 10920.

[29] N. Goswami, S. Chaudhuri, A. Giri, P. Lemmens, S.K. Pal, Surface engineering for controlled nanocatalysis: Key dynamical events from ultrafast electronic spectroscopy, *J. Phys. Chem. C* 118 (2014) 23434.

[30] R. Viswanatha, S. Sapra, S. Sen Gupta, B. Satpati, P. Satyam, B. Dev, D. Sarma, Synthesis and characterization of Mn-doped ZnO nanocrystals, *J. Phys. Chem. B* 108 (2004) 6303.

[31] A. Makhal, S. Sarkar, T. Bora, S. Baruah, J. Dutta, A. Raychaudhuri, S.K. Pal, Dynamics of light harvesting in ZnO nanoparticles, *Nanotechnology*, 21 (2010) 265703.

[32] J.L. Brédas, J. Cornil, D. Beljonne, D.A. Dos Santos, Z. Shuai, Excited-state electronic structure of conjugated oligomers and polymers: A quantum-chemical approach to optical phenomena, *Acc. Chem. Res.* 32 (1999) 267.

[33] S. Sardar, P. Kar, H. Remita, B. Liu, P. Lemmens, S.K. Pal, S. Ghosh, Enhanced charge separation and FRET at heterojunctions between semiconductor nanoparticles and conducting polymer nanofibers for efficient solar light harvesting, *Sci. Rep.* 5 (2015) 17313.

[34] R.M. Cory, D.M. McKnight, Fluorescence spectroscopy reveals ubiquitous presence of oxidized and reduced quinones in dissolved organic matter, *Environ. Sci. Technol*. 39 (2005) 8142.

[35] E. Selli, A. De Giorgi, G. Bidoglio, Humic acid-sensitized photoreduction of Cr (VI) on ZnO particles, *Environ. Sci. Technol*. 30 (1996) 598.

[36] K. Yang, D. Lin, B. Xing, Interactions of humic acid with nanosized inorganic oxides, *Langmuir* 25 (2009) 3571.

[37] H. Wu, N.I. Gonzalez-Pech, V.H. Grassian, Displacement reactions between environmentally and biologically relevant ligands on $TiO_2$ nanoparticles: Insights into the aging of nanoparticles in the environment, *Environ. Sci. Nano* 6 (2019) 489.

[38] A. Sirelkhatim, S. Mahmud, A. Seeni, N.H.M. Kaus, L.C. Ann, S.K.M. Bakhori, H. Hasan, D. Mohamad, Review on zinc oxide nanoparticles: Antibacterial activity and toxicity mechanism, *Nano Micro Lett.* 7 (2015) 219.

[39] T. Adhikari, S. Kundu, A. Biswas, J. Tarafdar, A. Subba Rao, Characterization of zinc oxide nano particles and their effect on growth of maize (Zea mays L.) plant, *J. Plant Nutr.* 38 (2015) 1505.

[40] M. Bonebrake, K. Anderson, J. Valiente, A. Jacobson, J.E. McLean, A. Anderson, D.W. Britt, Biofilms benefiting plants exposed to ZnO and CuO nanoparticles studied with a root-mimetic hollow fiber membrane, *J. Agric. Food Chem.* 26 (2018) 6619.

[41] M. Keiluweit, J.J. Bougoure, P.S. Nico, J. Pett-Ridge, P.K. Weber, M. Kleber, Mineral protection of soil carbon counteracted by root exudates, *Nat. Clim. Change* 5 (2015) 588.

# Chapter 7

# Synthesis of Different Types of Metal Oxide Nanoparticles and to Study Their Activities for Potential Biological Applications

**7.1. Introduction:** Photodynamic therapy (PDT) is a revolutionary most exciting therapy strategy that involves non-invasive treatment of cancers of various types and locations [1-4]. It depends on the application of a photosensitizer (PS), which is intensely assembled in pathological tissues. The PS molecules generate ROS upon excitation at particular wavelength which involves selective destruction of the infected cells [5]. Over the last five decades, riboflavin (Rf) or vitamin $B_2$ has been used as a potential photosensitizer because of its tremendous ROS generation ability under visible light irradiation [6, 7]. It is a water soluble essential micronutrient and substantially available in dietary products of both vegetable and animal origin [8-10]. The effectiveness of PDT depends on the photo excitation of the PS assembled at the target sites as well as its pharmacokinetic properties to achieve the desired biological response. However, conventional therapeutic agent assists some limitations such as poor solubility, short circulation time, high immunogenicity and non-specific distribution throughout the body, which lead to induction of various side effects in normal tissues [11, 12].

Nanomaterials as drug carriers can overcome these limitations as they exhibit upgraded pharmacokinetics and biodistribution of drugs and their accumulation at the targeted site reduces toxicity [13]. Also, the solubility of hydrophobic drugs increases upon formulation of nanoconjugates [14]. Moreover, sensitization of drugs by inorganic nanoparticles (NPs) through formulation of nanohybrid is key for the enhancement of drug activity [15]. In recent years, a variety of nanohybrids have been used to deliver drugs and biomolecules to achieve satisfying therapeutic effects [16-18]. Amongst all, ZnO based nanohybrids are most promising in terms of

modulation of drug activity, disease site specific targeted delivery and less toxicity [19].The utilization of duel sensitization can be very useful in order to get more efficiency in photodynamic therapy. This novel approach is based on the fluorescence resonance energy transfer (FRET) between covalently linked donor molecules to the acceptor, attached to the surface of semiconductor which has been previously used to enhance the efficiency in dye sensitized solar cell [20, 21]. In recent times, a few groups have reported the dual sensitized nanohybrids consisting of quantum dots and upconverson nanomaterials [22-26]. Although, all of the earlier reported nanohybrids are only toxic, they also require complicated and expensive methods for their synthesis. However, the implementation of this kind of system in PDT is not highlighted in contemporary literatures. In this regard, development of organic/inorganic nanohybrid system using plasmonic NPs could be a better solution for the enhanced efficacy in PDT and thus is one of the main motives of the present work.

Herein, we have selected Rf as a model photosensitizer, attached with ZnO NPs and further attached with Au decorated ZnO. We specifically chose Au NPs as noble metal because of their greater biocompatibility than that of other noble metals and ease of synthesis [27]. The sizes of the NPs and decoration of Au on the ZnO surface are confirmed by electron microscopic techniques. The attachment of Rf has been investigated by optical spectroscopic and DFT based methods. Picosecond-resolved fluorescence study explores the excited-state photoelectron transfer process from Rf to ZnO and FRET from RF to Au in Rf-ZnO-Au nanohybrids which has been confirmed by fluorescence transient of Rf-$Al_2O_3$-Au nanohybrid. The presence of Au influences huge charge separation in the Rf-ZnO-Au nanohybrid upon blue light irradiation which leads to greater production of ROS upon blue light irradiation. The Rf-ZnO-Au nanohybrids show enhanced antibacterial activity in dose-dependent manner against Methicillin-resistant *staphylococcus aureus* (MRSA) due to photoinduced ROS. In short, the present study demonstrates duel sensitization of Rf for enhanced ROS generation for potential antibacterial activity that could be effective for photodynamic therapy.

## 7.2. Results and Discussion:

**7.2.1. Dual-Sensitization via Electron and Energy Harvesting in a Nanohybrid for Improvement of Therapeutic Efficacy [28]:** Figures 7.1.a and 7.1.b show the high resolution transmission electron microscopy (HRTEM) image of Au decorated ZnO NPs. It depicts Au NPs are uniformly decorated on the surface of ZnO and the average diameter of Au NPs is found to be ~10 nm. The interplanar distance of the lattice fringes of ZnO NPs is measured to be 0.28 nm which corresponds to the (100) crystal planes. Whether an interplanar distance of 0.31 nm for the Au NPs signifies the (222) crystal planes [29, 30].

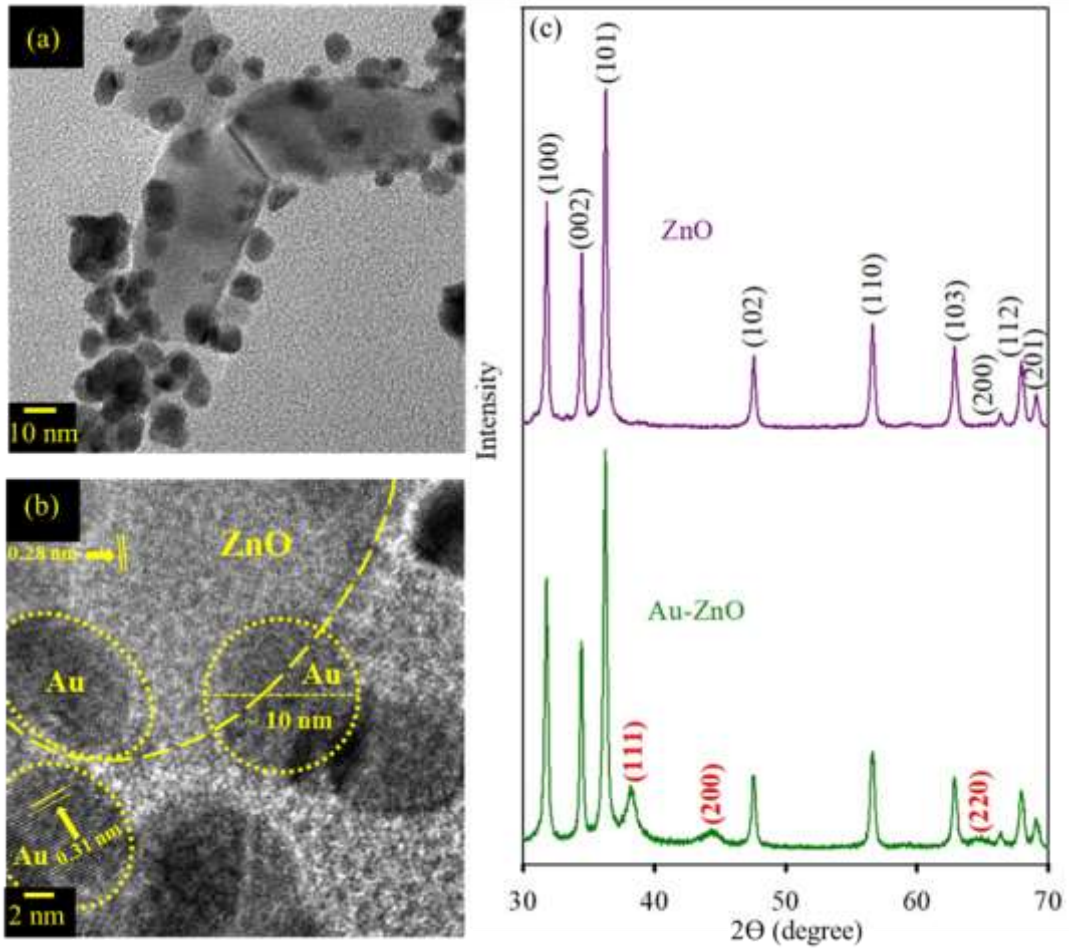


***Figure 7.1.*** *(a) TEM image of Au-ZnO. (b) HRTEM image of Au-ZnO. (c) Powder XRD pattern of ZnO (violet) and Au-ZnO (green).*

The low magnification TEM images of Au-ZnO show the uniform decoration of Au on the surface of ZnO (Figures 7.2.a, 7.2.b and 7.2.c). The size distribution of Au NPs on the surface of ZnO has been calculated (Figure 7.2d). The average

size of Au nanoparticles is found to be ~9 nm. The atomic percentage of Au is found to be 6.85. Figure 7.1.c displays characteristic X-ray diffraction (XRD) patterns of ZnO and Au-ZnO hybrids. The diffraction pattern of the ZnO NPs suggests its hexagonal wurtzite structure [31]. The decoration of Au NP into the surface of ZnO NPs could not change the position of the diffraction peaks of ZnO which indicates the surface of ZnO remains intact upon Au decoration. However, some additional characteristic peaks of Au NPs appear in the XRD pattern of the Au-ZnO nanohybrids.

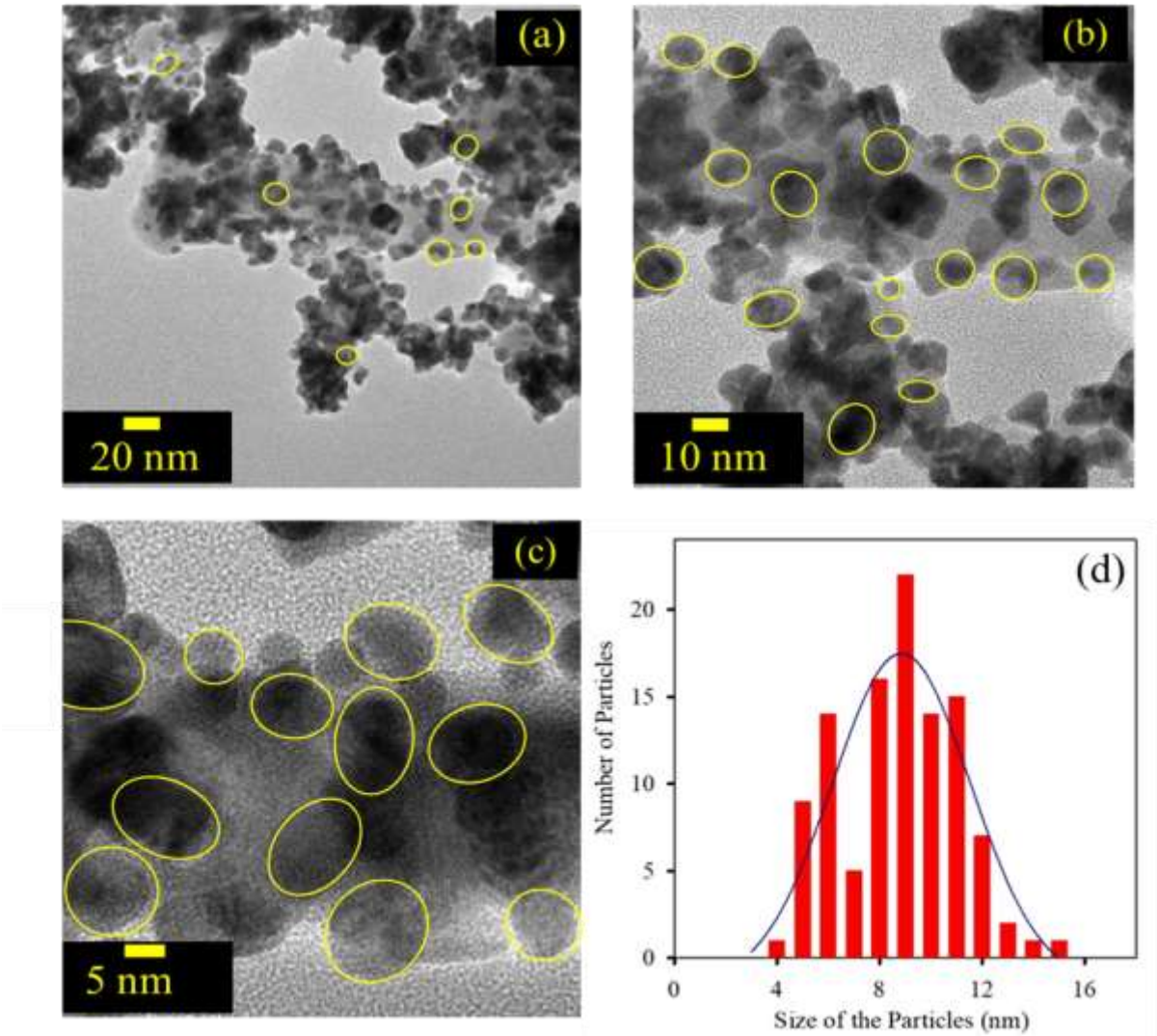


**Figure 7.2.** *(a), (b) and (c) The low-magnification TEM images of Au-ZnO nanohybrid. (d) Size distribution of Au nanoparticles on the surface of ZnO. The average size of Au nanoparticles is found to be ~9 nm.*

The positions (2θ value) of the diffraction peaks of Au NPs are observed to be at 38.13°, 44.28° and 64.55° which signifies the (111), (200) and (220) crystal planes

respectively [32]. The absorption spectra (Figure 7.3.a) of Rf in ethanol exhibits two characteristic peaks at 351 nm and 445 nm respectively. In case of Rf-ZnO and Rf-ZnO-Au, the change in absorbance peak at 445 nm indicates the complex formation between Rf and the surfaces of both ZnO, Au-ZnO as shown in Figure 7.3.a. The absorption spectra of Au-ZnO possess two characteristic peaks of Au and ZnO at 536 nm and 369 nm respectively.

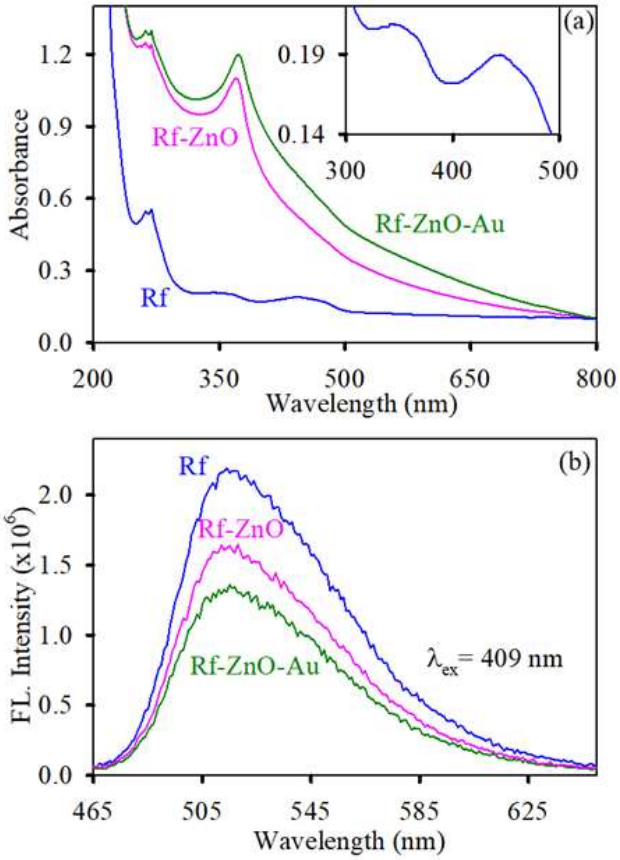


***Figure 7.3.*** *(a) UV-VIS absorption spectra of Rf (blue), Rf-ZnO (pink) and Rf-ZnO-Au (green) in ethanol. Insert shows enlarge absorption spectra of Rf in ethanol (c) Room temperature emission spectra of Rf (blue), Rf-ZnO (pink) and Rf-ZnO-Au (green) in ethanol.*

No distinct peak of Rf is notified in both nanohybrid due to very low concentration of Rf and significant scattering of the NPs. Whereas, the characteristic peak of ZnO is visible for both nanohybrid. However, the attachment of Rf is concluded from steady state emission spectrum. It shows a sharp emission peak at 520 nm upon excitation at 409 nm in ethanol. In case of Rf-ZnO and Rf-ZnO-Au, the characteristic peak of Rf is observed along with significant quenching in emission intensity as depicted in Figure 7.3.b. The emission quenching for both nanohybrids signifies the existence of

an excited stated non-irradiative process. Further, the DFT and TD-DFT based computational calculations are performed to understand the electronic structures. Computational investigations are particularly useful for understanding trends observed in the properties of molecular materials. The structure of Rf is optimized by DFT/B3LYP method as shown in the inset of Figure 7.4.a.

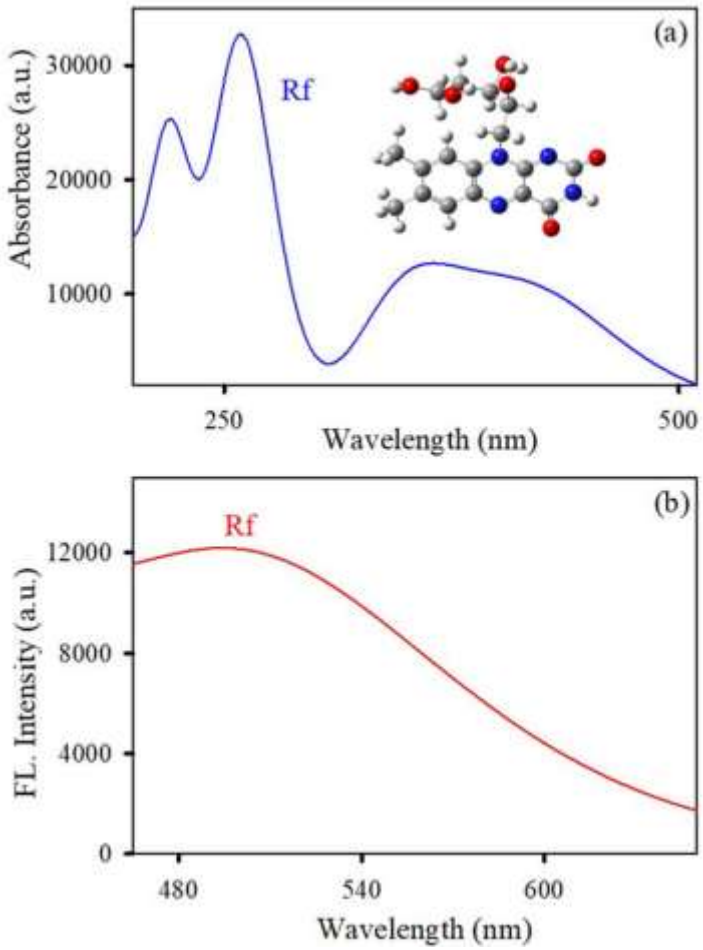


***Figure 7.4.*** *(a) Theoretical UV-Visible absorbance of Rf. Insets shows the structure of Rf. (b) Theoretical Emission spectra of Rf.*

The UV-vis absorption spectra are calculated using the most stable structure of Rf by TD-DFT/B3LYP based method as depicted in Figure 7.4.a which is well matched with experimental absorption. Figure 7.4.b depicts the calculated emission spectra of Rf. The calculated emission peak is well consistent with experimental findings. The TDOS of Rf is calculated using DFT/B3LYP exchange correlation functional method and plotted in GaussSum 2.1.4 software as shown in Figure 7.5.a. It composed of valence and conduction bands of Rf which is separated by an energy gap of 2.7 eV. Figure 7.5.b shows electron delocalization of Rf at HOMO and LUMO respectively.

The structure of pristine $Zn_{12}O_{12}$ is prepared by eight hexagons of $(ZnO)_3$ and six tetragons of $(ZnO)_2$ rings with tetrahedral rotational as well as inversion symmetry. Inset of Figure 7.6.a depicts the structural geometry of pristine $Zn_{12}O_{12}$. Average bond lengths of hexagons ($L_1$) and tetragons ($L_2$) are about 1.88 and 1.96 Å respectively. The angles in hexagons ($\theta_1$, $\theta_2$) and tetragons ($\theta_3$, $\theta_4$) are 126.68°, 112.29°,91.07° and 87.75° respectively. Recently, the optimized structure of $Zn_{12}O_{12}$ using DFT/B3LYP exchange correlation functions showed that the distances $L_1$ and $L_2$ were 1.85 and 1.93 Å respectively. The calculated $\theta_1$, $\theta_2$, $\theta_3$ and $\theta_4$ angles were obtained to be 126.41°, 112.37°, 91.97° and 86.92° respectively [33]. It can be concluded that the obtained theoretical results are well matched with previously reported literatures [33, 34]. The absorption spectrum of $Zn_{12}O_{12}$ is calculated by using same exchange-correlation function. The calculated absorption peak is found to be at a wavelength of 350 nm as shown in Figure 7.4.a which is well consistent with our experimental absorption spectra [34].

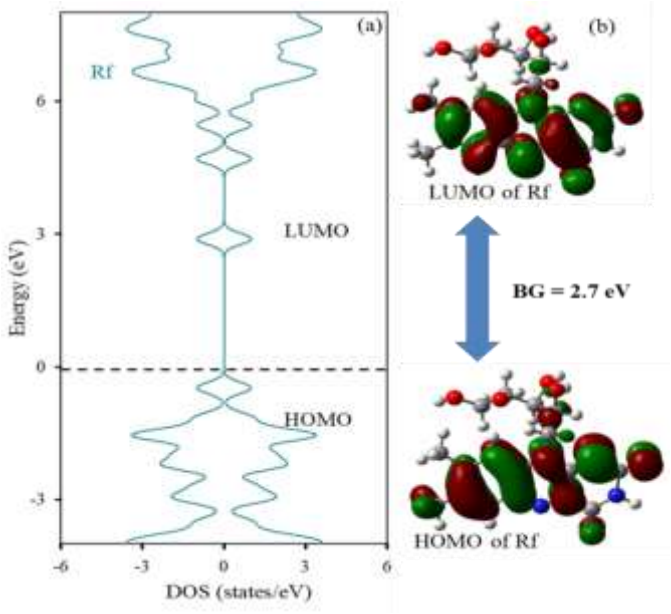


***Figure 7.5.*** *(a) The density of states (DOS) plot of Rf. (b) HOMO and LUMO of optimized geometrical structure of Rf. Energy gap between HOMO and LUMO is 2.7 eV.*

The TDOS of $Zn_{12}O_{12}$ is calculated using B3LYP exchange correlation functional method and plotted in GaussSum 2.1.4 software as shown in Figure 7.6.b. It depicts proper orbital delocalization in valence and conduction bands of $Zn_{12}O_{12}$ NPs. HOMO and LUMO of $Zn_{12}O_{12}$ are separated by a band-gap of 3.48 eV which is well

The calculated band-gap is found to be 1.89 eV, which indicates the formation of Au-doped $Zn_{12}O_{12}$ hybrid nanomaterials.

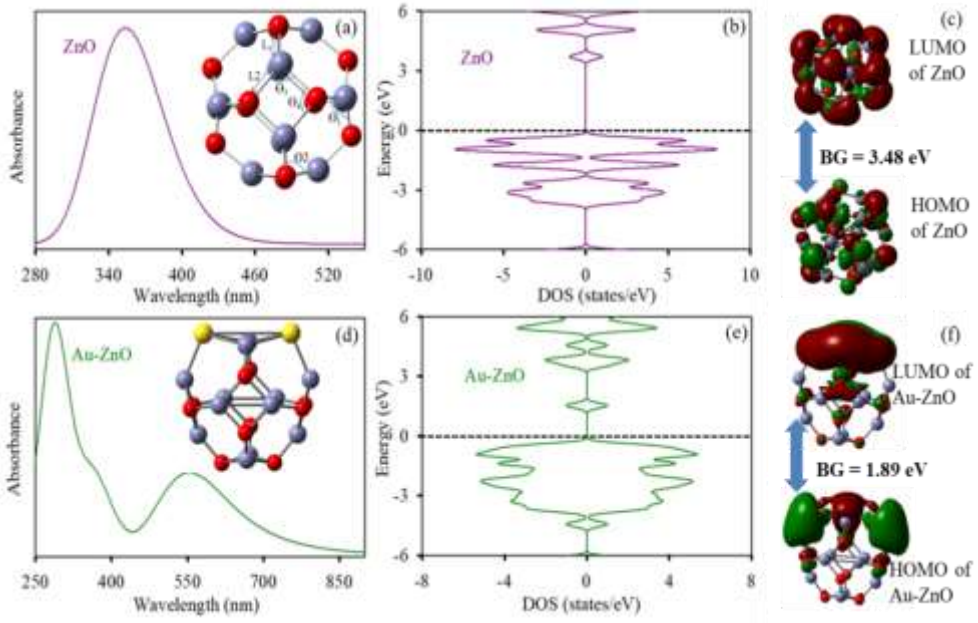


***Figure 7.6.*** *(a) Theoretical UV-Visible absorbance of ZnO. Inset shows the structure of $Zn_{12}O_{12}$. (b) The density of states (DOS) plot of ZnO. (c) LUMO (top) HOMO (bottom) of optimized geometrical structure of ZnO. Energy gap between HOMO and LUMO is 3.48 eV. (d) Theoretical UV-Visible absorbance of Au-ZnO. Inset shows the structure of Au-doped $Zn_{12}O_{12}$. (e) The density of states (DOS) plot of Au-ZnO. (f) LUMO (top) HOMO (bottom) of optimized geometrical structure of Au-ZnO. Energy gap between HOMO and LUMO is 1.89 eV.*

matched with reported literature [35]. Figure 7.6.c depicts surfaces of the frontier molecular orbitals (HOMO/LUMO) of $Zn_{12}O_{12}$. The molecular orbitals (HOMO and LUMO) of the $Zn_{12}O_{12}$ NPs are localized on respective Zn and O sites which imply the Zn sites are electrophilic and O sites are nucleophilic in nature. The Au-doped $Zn_{12}O_{12}$ NPs are prepared by replacing two Zn atoms of optimized $Zn_{12}O_{12}$ structure with two Au atoms. Inset of Figure 7.6.d depicts the optimized geometry of Au-doped $Zn_{12}O_{12}$ structure calculated by B3LYP/6-311++G (d,p)-SDD based method. The UV-vis absorption spectra of Au-doped $Zn_{12}O_{12}$ are calculated with the most stable geometry of hybrids as shown in Figure 7.6.d which well matches our experimental results. The TDOS of Au-doped $Zn_{12}O_{12}$ nanoparticle is calculated as shown in Figure 7.6.e. The doping of Au shifts the HOMO level to higher energies, and consequently, the band-gap becomes comparatively narrowed. The surfaces of

the frontier molecular orbitals (HOMO/LUMO) of Au-doped $Zn_{12}O_{12}$ hybrid is depicted in Figure 7.6.f. It depicts the electron density is shifted towards Au due to higher electron affinity. The attachment of Rf on the surface of Au-ZnO is optimized by using DFT/B3LYP method as shown in Figure 7.7.a. The DOS of Rf-ZnO-Au (Figure 7.7.b) depicts some additional states which indicate the electron transfer process from LUMO of Rf to the conduction band of ZnO [37].

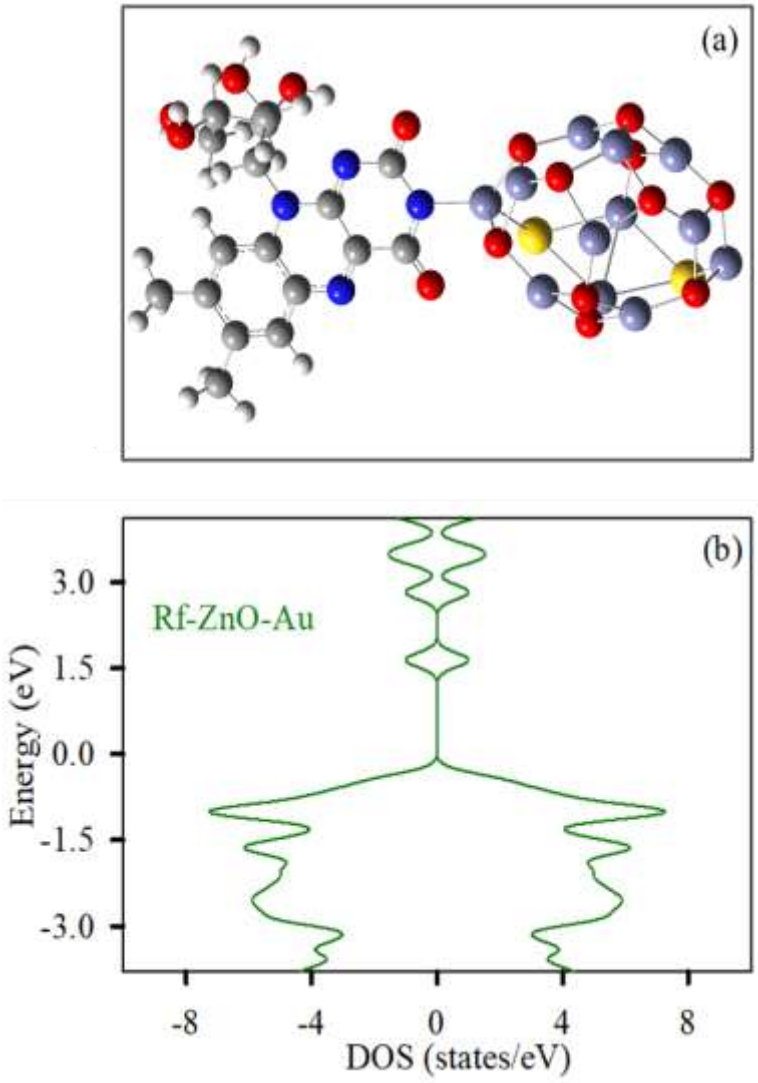


***Figure 7.7.*** *(a) The attachment of Rf on the surface of Au-ZnO. (b) The density of states (DOS) plot of Rf-ZnO-Au.*

In order to study the charge transfer process, the picosecond-resolved fluorescence experiment is performed. The times-resolved transients depict the faster fluorescence decay for both Rf-ZnO and Rf-ZnO-Au nanohybrid as compared to only Rf solution (Figure 7.8.a). The fluorescence decay was monitored at 520 nm with excitation of

409 nm laser source. The fluorescence transient of Rf is characterized by two-time constants of 643 ps and 5313 ps with an average lifetime of 3762 ps which decreases significantly for the Rf-ZnO due to presence of an additional faster component of ~54 ps (having 46.33 % contribution).

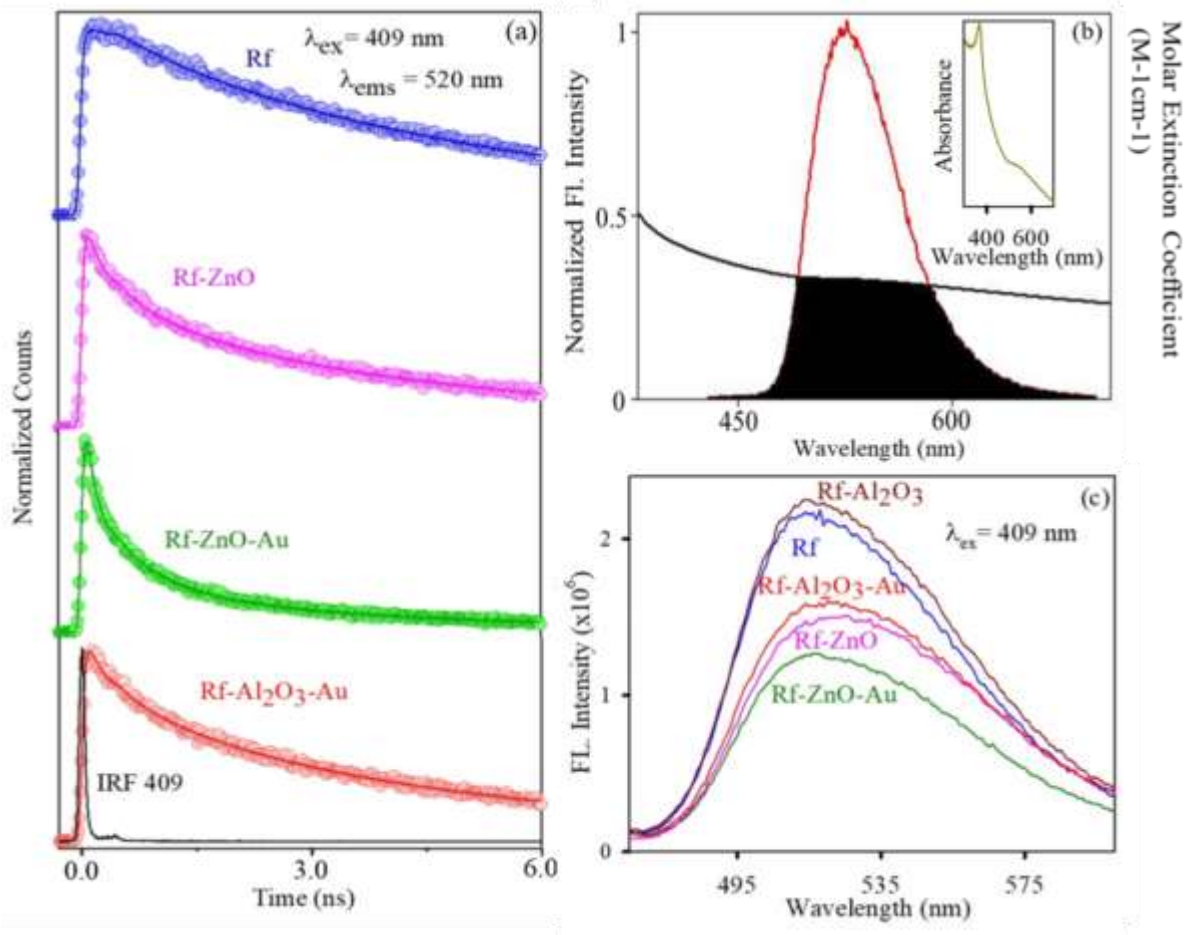


***Figure 7.8.*** *(a) Picosecond resolved fluorescence transients of Rf (blue), Rf-ZnO (pink), Rf-ZnO-Au (green) and Rf-$Al_2O_3$-Au (red) in ethanol. (b) Spectral overlap between Emission Rf (red) and Absorption of Au-ZnO (black).Inset shows the enlarge absorption spectra of Au-ZnO. (c) Room temperature emission spectra of Rf (blue), Rf-ZnO (pink), Rf-ZnO-Au (green), Rf-$Al_2O_3$ (grey) and Rf-$Al_2O_3$-Au (red) in ethanol.*

The faster component of 54 ps attributes interfacial excited state photoelectron transfer process from the LUMO of Rf to the conduction band (CB) of ZnO NPs [38-40]. In case of Rf-ZnO-Au nanohybrid, the faster component of 48 ps attributes interfacial excited state electron transfer [15]. It has to be states that the time component of 155 ps could be manifestation of FRET from Rf to Au [38]. Moreover, we have introduced Rf-$Al_2O_3$-Au nanohybrid ($Al_2O_3$ is an insulator) and measured time resolved fluorescence for further clarification. Herein, the time constant of 143 ps (contribution of 38.6%) indicates the energy transfer from Rf to Au NPs (Since

$Al_2O_3$ is an insulator, the possibility of excited state photoelectron transfer process from Rf to $Al_2O_3$ is insignificant). In case of Rf-ZnO-Au nanohybrid, an almost similar times constant of 155 ps implies the energy transfer from Rf to Au. The fitting parameters of fluorescence transient are listed in Table 7.1. Moreover, the overlap between emission of donor (Rf) and absorption of acceptor as shown in Figure 7.8.b (Herein, gold is the acceptor, the enlarge absorption spectra of Au-ZnO are shown in the inset of Figure 7.8.b where the peak of Au at 530 nm is visible) confirm the possibility of significant dipolar coupling between Rf and Au.

***Table 7.1.*** *Lifetime of picosecond time-resolved fluorescence transients of Rf, Rf-ZnO, Rf-ZnO-Au and Rf-$Al_2O_3$-Au in ethanol*

| System | Excitation wavelength (nm) | Emission wavelength (nm) | $\tau_1$ (ps) | $\tau_2$ (ps) | $\tau_2$ (ps) | $\tau_{avg}$ (ps) |
|---|---|---|---|---|---|---|
| **Rf** | 409 | 520 | 643 (33.20%) | 5313 (66.80%) | | 3762.56 |
| **Rf-ZnO** | 409 | 520 | 54 (46.33%) | 646 (28.67%) | 5020 (25%) | 1466.23 |
| **Rf-ZnO-Au** | 409 | 520 | 48 (54.6%) | 155 (32.3%) | 4202 (13.1%) | 626.84 |
| **Rf-$Al_2O_3$-Au** | 409 | 520 | 143 (38.6%) | 823 (28.6%) | 5098 (32.8%) | 1962.72 |

The steady state emission of all the samples is represented in Figure 7.8.c. It shows significant emission quenching of Rf-$Al_2O_3$-Au with respect to only Rf which also indicates the FRET between RF and Au. The FRET efficiency and the overlap integral [J (λ)] are calculated to be 47.83% and $5.89 \times 10^{15}$ $M^{-1}$ $cm^{-1}$ $nm^4$, respectively. The distance between donor (Rf) and acceptor (surface of Au NPs) is found to be 5.11 ± 0.025 nm, which is within the probing limit of FRET (1-10 nm). The presence of Au NPs with SPR band influences the enhanced electron injection from Au to ZnO as

evident from other reported literatures [41-44]. Photoinduced ROS generation is illustrated using a well-known non-fluorescent marker dichlorofluorescein (DCFH). DCFH oxidise to fluorescent dichlorofluorescein (DCF) by ROS exhibiting an emission near 520 nm upon excitation at 488 nm. Thus, the enhancement of ROS level is demonstrated by the enhancement of emission intensity at 520 nm [45]. The oxidation of DCFH is monitored for 8 minutes in the dark and then under irradiation of blue light for 24 minutes. In dark, there is no enhancement of emission intensity at 520 nm. Weather with increase in light exposure time, a greater enhancement of emission intensity is observed for Rf-Au-ZnO nanohybrid as compared to Rf-ZnO, Rf-$Al_2O_3$-Au, Rf and others controls (Figure 7.9.a). On the other hand Rf-ZnO produces greater ROS as compared to Rf-$Al_2O_3$-Au, Rf-$Al_2O_3$, Au-ZnO, Rf and DCFH only. In the course of excited state photoelectron transfer process of Rf-ZnO nanohybrid, the separated free electrons and the holes produce a significant from neighbouring oxygen and water molecules [46-48].

**z**

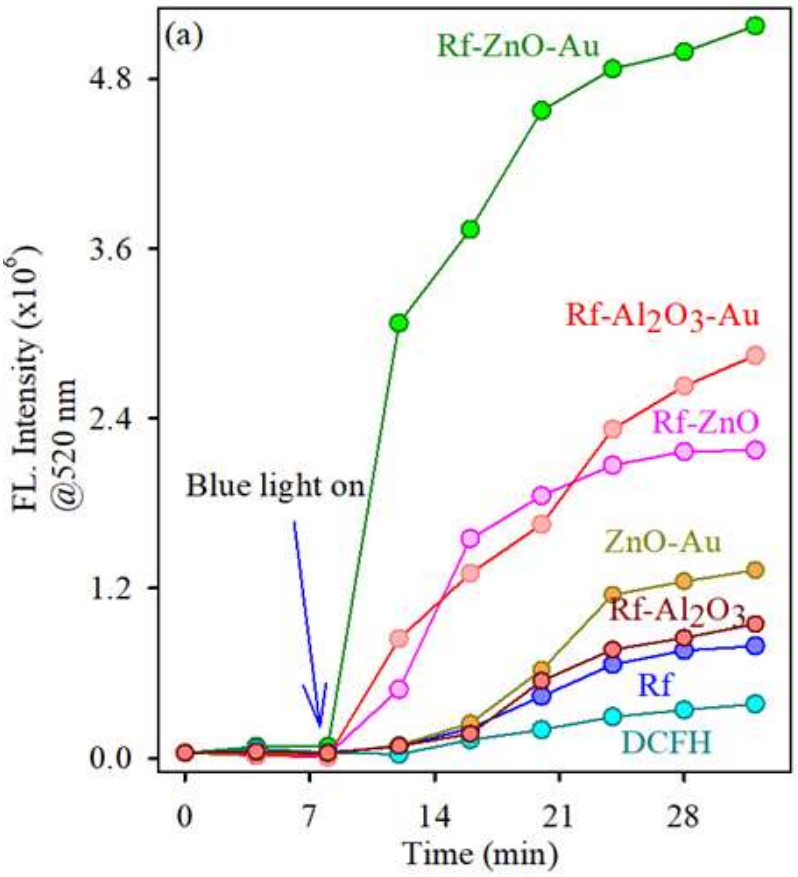


***Figure 7.9.*** *(a) DCFH oxidation (monitored at 520 nm) with time in presence of Rf (blue), Rf-ZnO (pink), Rf-ZnO-Au (green), Rf-$Al_2O_3$ (grey), Rf-$Al_2O_3$-Au (red) and DCFH (cyan) only only under dark (8 min) and blue light (24 min).*

In case of Rf-ZnO-Au nanohybrid, the energy transfer from Rf to Au NPs takes place due to dipolar coupling between Rf and Au NPs. Besides the photoelectron transfer process from the excited state of Rf to CB of ZnO in the Rf-ZnO-Au nanohybrid, the dipolar coupling between Rf and Au NPs also leads to electron transfer from Au NPs to the conduction band of ZnO [42-44].

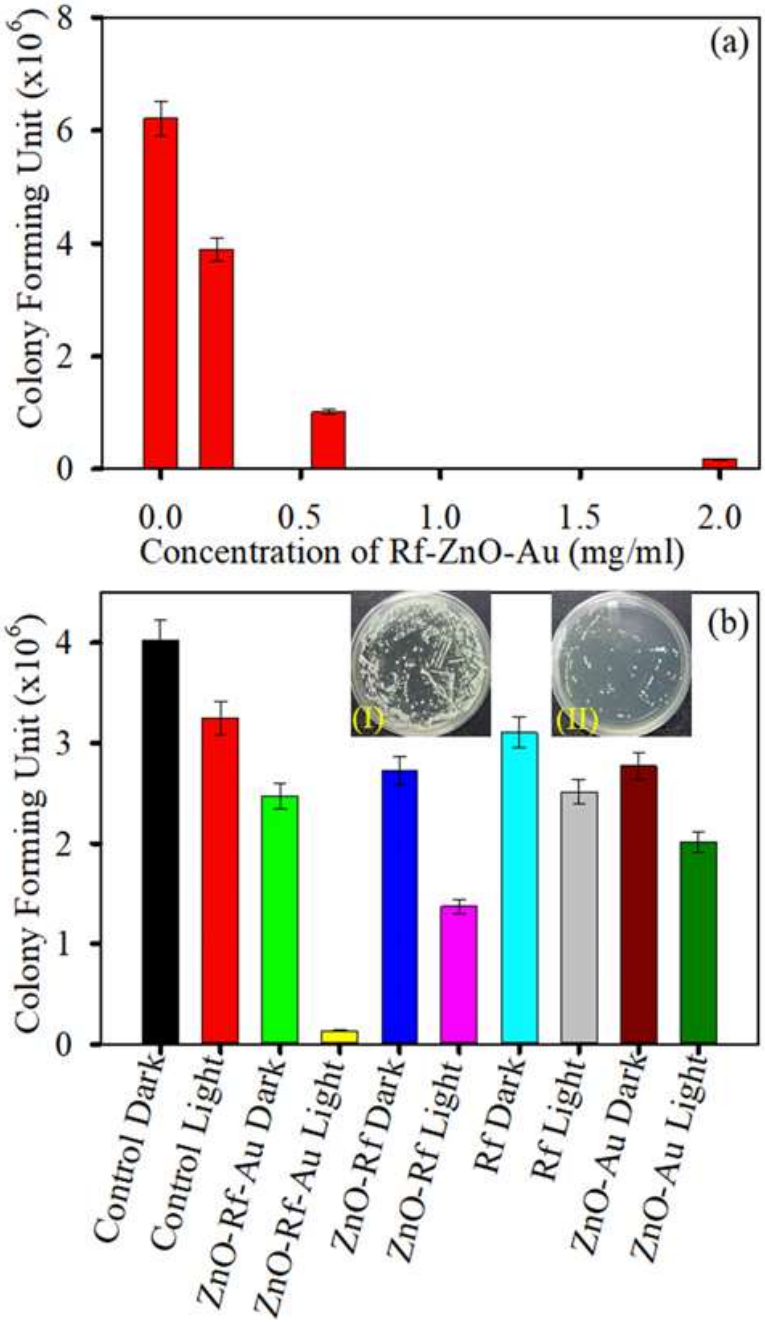


***Figure 7.10.*** *(a) Dose-dependent antibacterial effect of Rf-ZnO-Au at concentrations ranging from 0 to 2 mg/ml on MRSA under dark conditions. (b) Bacterial viability after treatment with 0.2 mg/ml Rf-ZnO-Au in the presence and absence of blue light irradiation (30 min). The inset shows images of MRSA plates treated with Rf-ZnO-Au before (I) and after (II) blue light irradiation.*

This seems to be huge charge separation in the Rf-ZnO-Au nanohybrid upon excitation, which results an excessive amount of ROS production over Rf-ZnO nanohybrid and other controls under blue light irradiation. Next, we have evaluated antimicrobial action of Rf-ZnO and Rf-Au-ZnO towards MRSA under dark and blue light illumination. In order to determine the dose dependent toxicity of RF-ZnO-Au nanohybrid towards MRSA, variable concentration of Rf-ZnO-Au (ranging from 0 to 2 mg/ml) was examined on the growth of MRSA using the CFU assay under dark condition (Figure 7.10.a). The minimum inhibition in the bacterial growth was observed at concentration of 0.2 mg/ml, whereas at the concentration of 1 mg/ml, the inhibition of bacterial growth is quite significant. In order to examine the photodynamic action, a concentration of 0.2 mg/ml of the Rf-ZnO-Au nanohybrid has been prepared. The images of MRSA plates represents the bacterial CFU significantly less in number in presence of light as compared to dark. There is no antibacterial activity under dark and light-irradiated conditions for the control treated samples (Figure 7.10.b). In case of Rf-ZnO treated sample, the bacterial growth is observed to have decreased by 65.9% in CFU compared to 96.7% for the Rf-ZnO-Au nanohybrid treated samples under irradiation with blue light. Thus, the inhibition in growth of the bacterial culture for the Rf-ZnO-Au nano-hybrid is highest (96.7%) relative to the other controls.

**7.3. Conclusion**: We have explored the effectiveness Rf-ZnO-Au nanohybrid in visible light harvesting over Rf-ZnO nanohybrid for the implementation in PDT. The attachment of Rf on ZnO surface and Au-ZnO surface was characterized electron microscopic, optical spectroscopic and DFT analysis techniques. The DFT and TD-DFT based calculations corroborates results from the experimental data. The picosecond resolved fluorescence transient shows the excited state electron transfer dynamics of Rf-ZnO and Rf-ZnO-Au. The photoinduced excited state charge transfer from Rf to ZnO in nanohybrid is responsible for overall efficient ROS generation over free Rf dye. Besides the excited state photoelectron transfer process, the presence of Au on ZnO surface influences the dipolar coupling between Au and Rf which leads to a huge charge separation in the Rf-ZnO-Au nanohybrid upon

excitation at blue light. This huge charge separation upon excitation results in greater of production of ROS for Rf-ZnO-Au nanohybrid over Rf-ZnO nanohybrid. The key advantage of Au on ZnO surface in the Rf-ZnO-Au nanohybrid is the enhancement of efficiency in ROS generation. The photodynamic antibacterial action on MRSA by both Rf-ZnO and Rf-ZnO-Au nanohybrid is confirmed from the CFU assay. After incubation of MRSA with the Rf-ZnO-Au nanohybrid, the significant reduction (96.7%) in CFU was observed upon blue light irradiation. Overall, the results highlight the crucial role of the plasmonic NPs in the Rf-ZnO-Au nanohybrid which influences efficiency of ROS production and hence antibacterial activity under blue light irradiation. It provides promising aspect for the improvement of Visible/NIR light driven photodynamic therapy which could be translated for others suitable photosensitizer.

# References

[1] N.P. Brodin, C. Guha, W.A. Tomé, Photodynamic therapy and its role in combined modality anticancer treatment, *Technol. Cancer Res. Treat.* 14 (2015) 355.

[2] Y. Li, S. Lv, Z. Song, J. Dang, X. Li, H. He, X. Xu, Z. Zhou, L. Yin, Photodynamic therapy-mediated remote control of chemotherapy toward synergistic anticancer treatment, *Nanoscale* 10 (2018) 14554.

[3] J. Zhang, C. Jiang, J.P.F. Longo, R.B. Azevedo, H. Zhang, L.A. Muehlmann, An updated overview on the development of new photosensitizers for anticancer photodynamic therapy, *Acta Pharm. Sin.* 8 (2018) 137.

[4] M.N. Hasan, A. Bera, T.K. Maji, S.K. Pal, Sensitization of nontoxic MOF for their potential drug delivery application against microbial infection, *Inorg. Chim. Acta* 523 (2021) 120381.

[5] D.R. Cardoso, S.H. Libardi, L.H. Skibsted, Riboflavin as a photosensitizer. Effects on human health and food quality, *Food Funct.* 3 (2012) 487.

[6] R. Huang, E. Choe, D. Min, Kinetics for singlet oxygen formation by riboflavin photosensitization and the reaction between riboflavin and singlet oxygen, *J. Food Sci.* 69 (2004) C726.

[7] A.D.L Rochette, E. Silva, I. Birlouez-Aragon, M. Mancini, A.M. Edwards, P. Morlière, Riboflavin: Photodegradation and photosensitizing effects are highly dependent on oxygen and ascorbate concentrations, *Photochem. Photobiol.* 72 (2000) 815.

[8] E. Barton-Wright, T. Moran, H. Sarson, Riboflavin and Vitamin $B_1$ In Nineteenth Century Buns and Ale, *Natur*e 152 (1943) 273.

[9] R. Huang, H.J. Kim, D.B. Min, Photosensitizing effect of riboflavin, lumiflavin, and lumichrome on the generation of volatiles in soy milk, *J. Agric. Food Chem.* 54 (2006) 2359.

[10] S. Chaudhuri, S. Batabyal, N. Polley, S.K. Pal, Vitamin B2 in nanoscopic environments under visible light: Photosensitized antioxidant or phototoxic drug?, *J. Phys. Chem. A* 118 (2014) 3934.

[11] L. Zhang, F. Gu, J. Chan, A. Wang, R. Langer, O. Farokhzad, Nanoparticles in medicine: Therapeutic applications and developments, *Clin. Pharmacol. Ther.* 83 (2008) 761.

[12] M.E. Davis, Z. Chen, D.M. Shin, Nanoparticle therapeutics: An emerging treatment modality for cancer, *Nanosci. Technol.*: *A collection of reviews from nature journals* 25 (2010) 239.

[13] B. Mishra, B.B. Patel, S. Tiwari, Colloidal nanocarriers: A review on formulation technology, types and applications toward targeted drug delivery, *Nanomedicine: Nanotechnol., Biol., Med.* 6 (2010) 9.

[14] M. Narvekar, H.Y. Xue, J.Y. Eoh, H.L. Wong, Nanocarrier for poorly water-soluble anticancer drugs barriers of translation and solutions, *Aaps. Pharmscitech.* 15 (2014) 822.

[15] D. Bagchi, V.S. Rathnam, P. Lemmens, I. Banerjee, S.K. Pal, NIR-Light-active ZnO-based nanohybrids for bacterial biofilm treatment, *ACS omega* 3 (2018) 10877.

[16] N. Zhao, L. Yan, X. Zhao, X. Chen, A. Li, D. Zheng, X. Zhou, X. Dai, F.-J. Xu, Versatile types of organic/inorganic nanohybrids: From strategic design to biomedical applications, *Chem. Rev.* 119 (2018) 1666.

[17] L.L. Tan, L. Shang, Smart Delivery Systems Based on Poly (glycidyl methacrylate) s-Coated Organic/Inorganic Core–Shell Nanohybrids, *Macromol. Rapid Commun.* 40 (2019) 1800879.

[18] C. Liang, X. Zhang, Z. Wang, W. Wang, M. Yang, X. Dong, Organic/inorganic nanohybrids rejuvenate photodynamic cancer therapy, *J. Mater. Chem. B* 8 (2020) 4748.

[19] X. Huang, X. Zheng, Z. Xu, C. Yi, ZnO-based nanocarriers for drug delivery application: From passive to smart strategies, *Int. J. Pharm* 534 (2017) 190.

[20] C. Siegers, J. Hohl-Ebinger, B. Zimmermann, U. Würfel, R. Mülhaupt, A. Hinsch, R. Haag, A dyadic sensitizer for dye solar cells with high energy-transfer efficiency in the device, *ChemPhysChem* 8 (2007) 1548.

[21] J. Patwari, S. Sardar, B. Liu, P. Lemmens, S.K. Pal, Three-in-one approach towards efficient organic dye-sensitized solar cells: Aggregation suppression,

panchromatic absorption and resonance energy transfer, *Beilstein J. Nanotechnol.* 8 (2017) 1705.

[22] E. Lee, C. Kim, J. Jang, High-Performance Förster Resonance Energy Transfer (FRET)-Based Dye-Sensitized Solar Cells: Rational Design of Quantum Dots for Wide Solar-Spectrum Utilization, *Chem. Eur. J.* 19 (2013) 10280.

[23] S. Sarkar, A. Makhal, K. Lakshman, T. Bora, J. Dutta, S. Kumar Pal, Dual-sensitization *via* electron and energy harvesting in CdTe quantum dots decorated ZnO nanorod-based dye-sensitized solar cells, *J. Phys. Chem. C* 116 (2012) 14248.

[24] A.K. Pandey, M.S. Ahmad, M. Alizadeh, N. Abd Rahim, Improved electron density through hetero-junction binary sensitized $TiO_2$/CdTe/D719 system as photoanode for dye sensitized solar cell, Physica E: Low-dimensional Systems and *Nanostructures* 101 (2018) 139.

[25] M. Ambapuram, R. Ramireddy, G. Maddala, S. Godugunuru, P.V.S. Yerva, R. Mitty, Effective upconverter and light scattering dual function $LiYF_4$: $Er^{3+}$/$Yb^{3+}$ assisted photoelectrode for high performance cosensitized dye sensitized solar cells, *ACS Appl. Electron. Mater.* 2 (2020) 962.

[26] H. Gu, J. Wang, Y. Li, Z. Wang, Y. Fu, The core-shell-structured $NaYF_4$: $Er^{3+}$, $Yb^{3+}$@ $NaYF_4$: $Eu^{3+}$ nanocrystals as dual-mode and multifunctional luminescent mechanism for high-performance dye-sensitized solar cells, *Mater. Res. Bull.* 108 (2018) 219.

[27] A.M. Craciun, M. Focsan, K. Magyari, A. Vulpoi, Z. Pap, Surface plasmon resonance or biocompatibility: Key properties for determining the applicability of noble metal nanoparticles, *Materials* 10 (2017) 836.

[28] A. Bera, M.N. Hasan, A. Chatterjee, D. Mukherjee, S.K. Pal, Dual sensitization *via* electron and energy harvesting in a nanohybrid for improvement of therapeutic efficacy, *ACS Phys. Chem. A*u 2 (2022) 171.

[29] X. Liu, M. Atwater, J. Wang, Q. Huo, Extinction coefficient of gold nanoparticles with different sizes and different capping ligands, *Colloids Surf. B* 58 (2007) 3.

[30] S. Chaudhuri, S. Sardar, D. Bagchi, S.S. Singha, P. Lemmens, S.K. Pal, Sensitization of an endogenous photosensitizer: Electronic spectroscopy of riboflavin

in the proximity of semiconductor, insulator, and metal nanoparticles, *J. Phys. Chem. A* 119 (2015) 4162.

[31] S.S. Kumar, P. Venkateswarlu, V.R. Rao, G.N. Rao, Synthesis, characterization and optical properties of zinc oxide nanoparticles, *Int. Nano Lett.* 3 (2013) 2228.

[32] A. Chatterjee, P. Kar, D. Wulferding, P. Lemmens, S.K. Pal, Flower-like BiOI microspheres decorated with plasmonic gold nanoparticles for dual detoxification of organic and inorganic water pollutants, *ACS Appl. Nano Mater.* 3 (2020) 2733.

[33] T. Afshari, M. Mohsennia, Transition metals doped ZnO nanocluster for ethylene oxide detection: A DFT study, *Main Group Met. Chem.* 42 (2019) 113.

[34] O.V. de Oliveira, J.M. Pires, A.C. Neto, J.D. dos Santos, Computational studies of the $Ca_{12}O_{12}$, $Ti_{12}O_{12}$, $Fe_{12}O_{12}$ and $Zn_{12}O_{12}$ nanocage clusters, *Chem. Phys. Lett.* 634 (2015) 25.

[35] M.N. Hasan, T.K. Maji, U. Pal, A. Bera, D. Bagchi, A. Halder, S.A. Ahmed, J.H. Al-Fahemi, T.M. Bawazeer, T. Saha-Dasgupta, S.K. Pal, Wide bandgap semiconductor-based novel nanohybrid for potential antibacterial activity: Ultrafast spectroscopy and computational studies, *RSC Adv.* 10 (2020) 38890.

[36] H.Y. Ammar, H.M. Badran, A. Umar, H. Fouad, O.Y. Alothman, ZnO nanocrystal-based chloroform detection: Density functional theory (DFT) study, *Coatings* 9 (2019) 769.

[37] T.K. Maji, M.N. Hasan, S. Ghosh, D. Wulferding, C. Bhattacharya, P. Lemmens, D. Karmakar, S. Kumar Pal, Development of a magnetic nanohybrid for multifunctional application: From immobile photocatalysis to efficient photoelectrochemical water splitting: A combined experimental and computational study, *J. Photochem. Photobiol. A* 397 (2020) 112575.

[38] J. Patwari, A. Chatterjee, S. Sardar, P. Lemmens, S.K. Pal, Ultrafast dynamics in co-sensitized photocatalysts under visible and NIR light irradiation, *Phys. Chem. Chem. Phys.* 20 (2018) 10418.

[39] S. Chaudhuri, S. Sardar, D. Bagchi, S. Dutta, S. Debnath, P. Saha, P. Lemmens, S.K. Pal, Photoinduced dynamics and toxicity of a cancer drug in proximity of inorganic nanoparticles under visible light, *ChemPhysChem* 17 (2016) 270.

[40] S.E. Koops, B.C. O'Regan, P.R. Barnes, J.R. Durrant, Parameters influencing the efficiency of electron injection in dye-sensitized solar cells, *J. Am. Chem. So*c. 131 (2009) 4808.

[41] P. Reineck, D. Gómez, S.H. Ng, M. Karg, T. Bell, P. Mulvaney, U. Bach, Distance and wavelength dependent quenching of molecular fluorescence by Au@ $SiO_2$ core–shell nanoparticles, *ACS nano* 7 (2013) 6636.

[42] W.R. Erwin, H.F. Zarick, E.M. Talbert, R. Bardhan, Light trapping in mesoporous solar cells with plasmonic nanostructures, *Energy Environ. Sci.* 9 (2016) 1577.

[43] S.T. Kochuveedu, T. Son, Y. Lee, M. Lee, D. Kim, D.H. Kim, Revolutionizing the FRET-based light emission in core-shell nanostructures *via* comprehensive activity of surface plasmons, *Sci. Rep.* 4 (2014) 4735.

[44] K.A. Kang, J. Wang, J.B. Jasinski, S. Achilefu, Fluorescence manipulation by gold nanoparticles: From complete quenching to extensive enhancement, *J. Nanobiotechnology* 9 (2011) 1477.

[45] S.A. Ahmed, M. Nur Hasan, D. Bagchi, H.M. Altass, M. Morad, I.I. Althagafi, A.M. Hameed, A. Sayqal, A.E.R.S. Khder, B.H. Asghar, Nano-MOFs as targeted drug delivery agents to combat antibiotic-resistant bacterial infections, *R. Soc. Open Sci* 7 (2020) 200959.

[46] W. He, H.K. Kim, W.G. Wamer, D. Melka, J.H. Callahan, J.J. Yin, Photogenerated charge carriers and reactive oxygen species in ZnO/Au hybrid nanostructures with enhanced photocatalytic and antibacterial activity, *J. Am. Chem. Soc.* 136 (2014) 750.

[47] W. He, H. Wu, W.G. Wamer, H.K. Kim, J. Zheng, H. Jia, Z. Zheng, J.J. Yin, Unraveling the enhanced photocatalytic activity and phototoxicity of ZnO/metal hybrid nanostructures from generation of reactive oxygen species and charge carriers, *ACS Appl. Mater. Interface*s 6 (2014) 15527.

[48] Z. Kang, X. Yan, L. Zhao, Q. Liao, K. Zhao, H. Du, X. Zhang, X. Zhang, Y. Zhang, Gold nanoparticle/ZnO nanorod hybrids for enhanced reactive oxygen species generation and photodynamic therapy, *Nano Res.* 8 (2015) 2004.

# Chapter 8

# Synthesis of Different Metal Sulphide Nanoparticles for Their Light Harvesting Activity Including Anticancer Effects

**8.1. Introduction:** Semiconducting nanoparticles (NPs) have elicited a multitude of investigations into their unique characteristics such as charge transport, light emission, mechanics and thermal diffusion [1, 2]. Since decade, it represents a dynamic area of interest in molecular and biomedical sciences [3]. However, NPs have a tendency to aggregate in order to minimise their surface energies which create a technical challenge to control their size, shape, stability, and dispersibility in desired solvent [4, 5]. Therefore, development of some effective surface protection strategies is very important to maintain the stability of the NPs. These strategies involve functionalization with organic ligands such as small organic molecules or surfactants, polymers, and biomolecules [6-8].

Over the past decade, 3d transition metal oxides ($M_xO_y$) NPs have attracted broad interest because of their potential applications in various fields including catalysis, energy storage, drug delivery and biomedical imaging [9-13]. In general, most transition metal oxides are analogous to typical transition metal sulfides $M_xS_y$. Previously, transition metal (Fe, Co, Ni, Cu, Zn and Mo) sulfides have received much attention due to their manifold crystal structures and potential applications in lithium-ion batteries (LIBs), solar cells, sensors, thermoelectric devices, fuel cells and supercapacitors [14-19]. In past few years, the transition metal sulfide NPs has been mainly explored for energy and catalysis-related applications which gain key interest from biomedical researchers across the world. But, there is still much scope for large improvements in terms of potential biological applications.Since the last decade, the implementation of surface functionalized manganese oxide ($Mn_xO_y$) NPs achieves ground breaking success in biomedical research. The variable oxidation states of manganese (II, III, IV and VII) provide a pH-dependent redox medium which has been utilized for efficient production of ROS (reactive oxygen species) and

antioxidants [20-23]. In this regard, development of surface functionalized MnS NPs could be an exciting attempt for potential biological applications. Manganese sulfide (MnS), a p-type semiconductor, has been used for sensing, magnetic resonance imaging (MRI) electrochemical water oxidation, lithium-ion batteries and photocatalysis because of its excellent optical and electrical properties [24-29]. However, its biological applications are barely reported. Also, the effects of capping ligand to modulate the surface properties of MnS NPs and the subsequent appearance of novel optical properties have not been studied yet.

In our present study, we have synthesized MnS NPs and then functionalized with citrate. The surface functionalization makes MnS NPs soluble in water. Microscopic and optical spectroscopic tools have been used in order to characterise both uncapped MnS NPs and citrate-MnS NPs respectively. We monitored the generation of ROS using dichlorofluorescin (DCFH) indicator. Citrate-MnS NPs produce an excessive amount of ROS at acidic/neutral pH without any photo activation. It is revealed that the mixed valence state of Mn (+2, +3 and +4) along with in the citrate-MnS NPs lead to this exceptional ROS production without photo activation. To study the nature of ROS, we performed the DCFH assay in presence of singlet oxygen quencher ($NaN_3$) and hydroxyl radical quencher (TAB). The citrate-MnS NPs exhibit a significant efficiency in bilirubin degradation and antibacterial activity against a gram-positive bacteria Staphylococcus hominies (*S. hominis)*. The remarkable efficiency of the citrate-MnS NPs in ROS generation without any photo activation indicates the promise of these NPs in potential therapeutic applications.

## 8.2. Results and Discussion:

### 8.2.1. Implementation of Surface Functionalization of MnS Nanoparticle for Achieving of Novel Optical Properties and Improving Therapeutic Potential [30]:

The X-ray diffraction (XRD) patterns of the as-synthesized NPs are shown in Figure 8.1.a. All diffraction peaks {(100), (002), (101), (110), (103) and (112) planes corresponding 26°, 28°, 29°, 46°, 50° and 54° diffraction angles respectively)} in the Figure 8.1.a are perfectly matched with wurtzite MnS crystal indexed in the literature [31, 32]. The TEM (Figure 8.1.b) and HRTEM (Figure 8.1.c) study has been

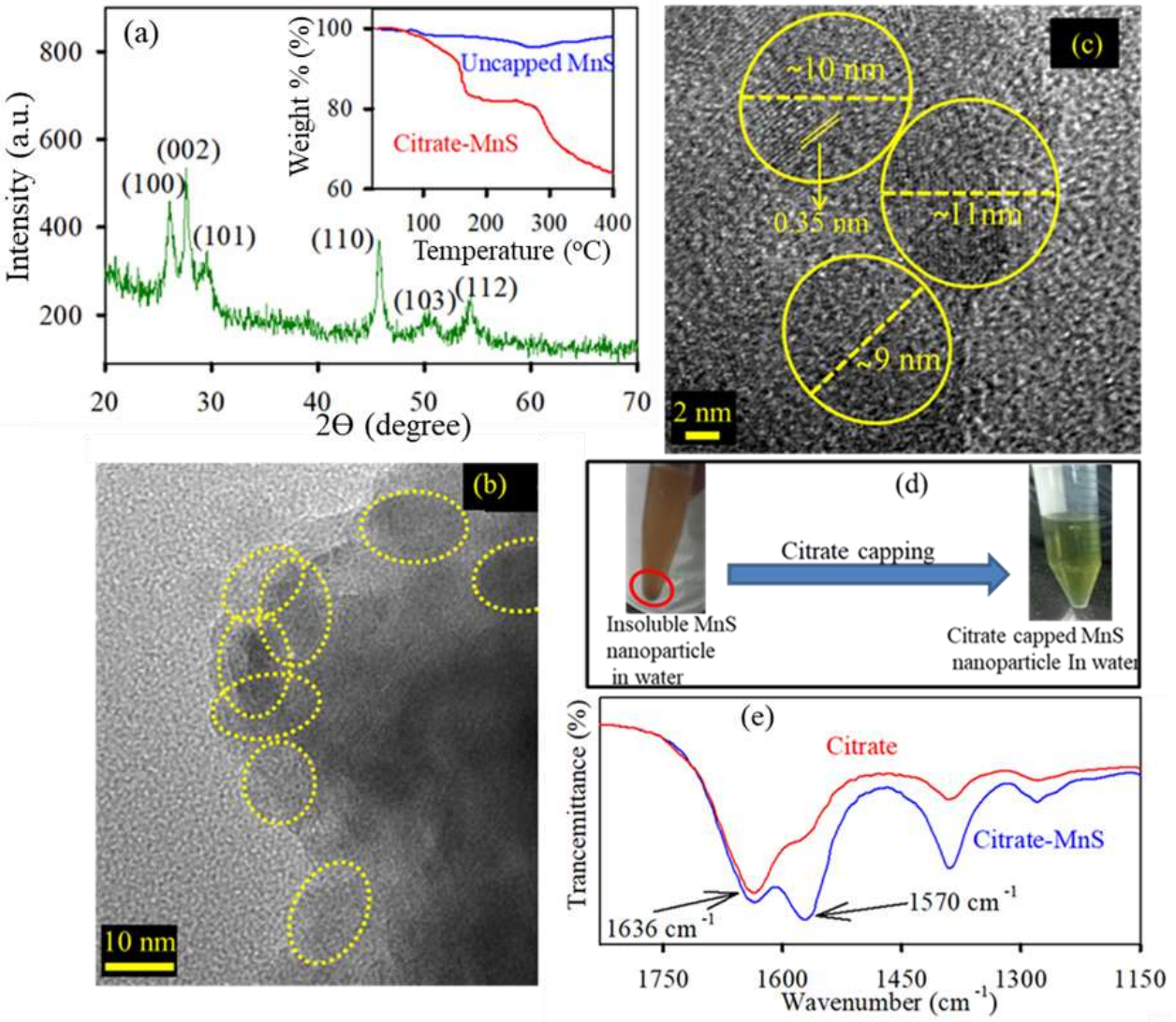


***Figure 8.1.*** *(a) XRD of MnS nanoparticles. (b) and (c) TEM and HRTEM of MnS nanoparticles respectively. (d) Scheme of citrate functionalization with MnS nanoparticles. (e) FTIR spectra of citrate (red) and citrate-MnS (blue).*

carried out in order to estimate the size and crystalline nature of the MnS NPs. The average size of MnS NPs is found to be around 10 nm. The HRTEM image depicts the crystallinity of the MnS NPs having interplanar distance of 0.35 nm, corresponding to the (100) plane of the crystal lattice [32].

The functionalization of MnS NPs with citrate influences their subsequent appearance of novel optical properties. As shown in Figure 8.1.d, the brownish dispersed solution MnS NPs turns to greenish and transparent upon citrate functionalization which infers the water solubility of citrate-MnS NPs. The loading of citrate on MnS was studied by thermogravimetric analysis (TGA). The inset of Figure 8.1.a shows the ther mogravimetric curves of uncapped MnS NPs and citrate-

MnS NPs. The presence of water molecules is responsible for the initial weight loss upto 154 $^{o}$C for citrate-MnS NPs. However, a significant percentage of weight loss is observed between 154 $^{o}$C to 400 $^{o}$C for citrate-MnS. The thermal degradation of about 29.7% in between154 $^{o}$C to 400 $^{o}$C for citrate-MnS is attributed to the presence of citrate molecules. Whereas in case of uncapped MnS NPs, negligible thermal degradation is observed upto 400 $^{o}$C. The number of citrate molecules on the surface of a single MnS NP was calculated to be 2317. The FTIR spectra of sodium citrate possess stretching frequencies at 1570 $cm^{-1}$ and 1632 $cm^{-1}$ corresponding to both symmetric and asymmetric stretching of $CO_3$ group respectively where the intensity of asymmetric stretching peak is much higher as compared to symmetric stretching peak (Figure 8.1.e). However, a huge increment in intensity of symmetric stretching

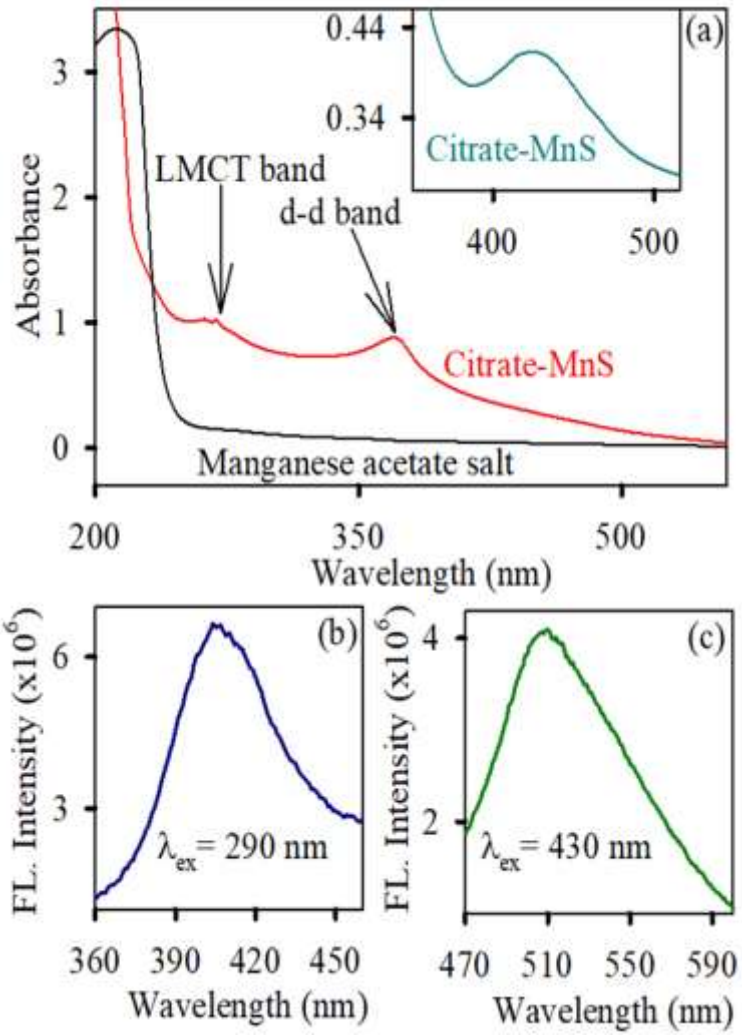


***Figure 8.2.*** *(a) UV-Vis absorption spectra of citrate-MnS (red) and manganese acetate salt (black) in water. Inset shows enlarge spectra of citrate-MnS in water (sky blue). (b) and (c) Steady state emission spectra of citrate-MnS upon excitation at 290 nm (blue) and 430 nm (green) respectively.*

peak is observed for citrate-MnS which implies the bi-dentate binding of citrate on the surface of MnS NPs. Citrate-MnS exhibits two characteristic absorption peaks at 293 nm and 430 nm in water (Figure 8.2.a). The peak at around 290 nm (in the inset) corresponds to the high energy ligand-to-metal charge transfer transition (LMCT) The LMCT is originated due to the interaction between the $Mn^{3+}$ centres and the surface bound citrate ligands in the citrate-MnS NPs [33]. Another band at 430 nm is attributed to d–d transitions cantered over $Mn^{2+/3+}$ ions in citrate–MnS NPs [33, 34]. Steady state emission spectrum of citrate-MnS shows a characteristic peak at 410 nm upon excitation at LMCT band ($\lambda_{ex}$ = 290 nm) (Figure 8.2.b). Whereas, the excitation at d-d band ($\lambda_{ex}$ = 430 nm) provides a strong emission peak at 520 nm (Figure 8.2.c).

To determine the production of ROS by citrate-MnS NPs, a well-known non-fluorescent marker dichlorofluorescein (DCFH) is used which is oxidized to fluorescent dichlorofluorescein (DCF) by ROS. DCF exhibits an emission near 520 nm upon excitation at 488 nm [35]. The oxidation of DCFH in the dark is monitored for 30 minutes in presence of citrate-MnS at pH 5, pH 7 and pH 8 separately, a huge enhancement of emission intensity at 520 nm at both acidic (pH 5) and neutral (pH 7) pH is observed indicating the presence of ROS and no change in emission intensity is observed at pH 8 indicating the absence of ROS (Figure 8.3.a). This phenomenon is consistent with the fact that, in acidic/neutral pH, $Mn^{3+}$ ions are unstable and have tendency to disproportionate into $Mn^{2+}$ and $Mn^{4+}$. This redox medium is responsible for huge generation of ROS. Furthermore, we have done another DCFH assay in a "light on-light off" manner for more clarification about pH-dependent redox medium (Figure 8.3.b). At first, we have measured the ROS at pH 5 under dark for 5 minutes and then base was added to maintain the pH of the solution at 8. The enhancement of emission intensity at 520 nm is arrested after the addition of base. But, under blue light irradiation for 5 minutes, the intensity at 520 nm is started to increase and further remains constant upon switching off the light. This process remains continues till saturation is established. The $Mn^{3+}$ ions disproportionate into $Mn^{2+}$ and $Mn^{4+}$ at PH 5 which is responsible for the increment of ROS but the process of disproportionation is irrupted upon addition of base (pH 8). Further, the

blue light irradiation influences the electron-hole separation in the MnS lattice which influences enhancement of ROS production [35, 36]. Furthermore, to investigate the

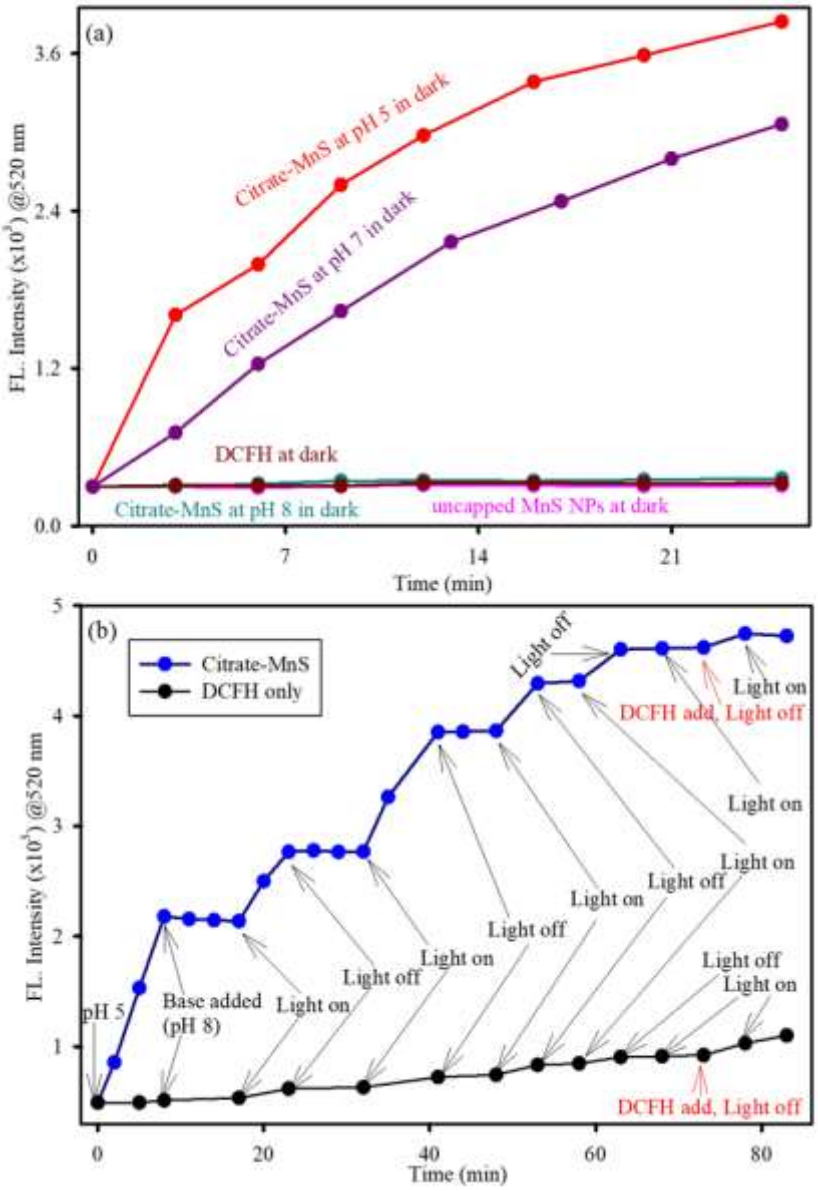


***Figure 8.3.*** *(a) DCFH oxidation (monitored at 520 nm) with time in presence of Citrate-MnS at pH 5 (red), at pH 7 (purple), at pH 8 (cyan), uncapped MnS NPs (pink) and DCFH only (gray). (b) DCFH oxidation (monitored at 520 nm) with time in presence of Citrate-MnS from pH 5 to pH 8 in a "light on-light off" (blue light) manner with time intervals.*

nature of generated ROS, we have performed DCFH assay for citrate-MnS at pH 5 in presence of singlet oxygen ($NaN_3$) quencher and hydroxyl radical quencher (TBA) [37, 38]. In presence of both $NaN_3$ and TBA, the enhancement of emission intensity at 520 nm is significantly quenched which implies the presence of both singlet oxygen and hydroxyl radical as ROS (Figure 8.4.a). The ability of singlet oxygen production

is always very useful in terms of anticancer and antitumor treatment. Moreover, we have performed bilirubin degradation in presence of citrate-MnS at pH 5 and pH 7 for 30 minutes at dark. The decrease in absorbance peak of bilirubin at 432 nm indicates the degradation of bilirubin [39]. As shown in figure 4b, the rate of degradation is significantly higher in both acidic/neutral pH.

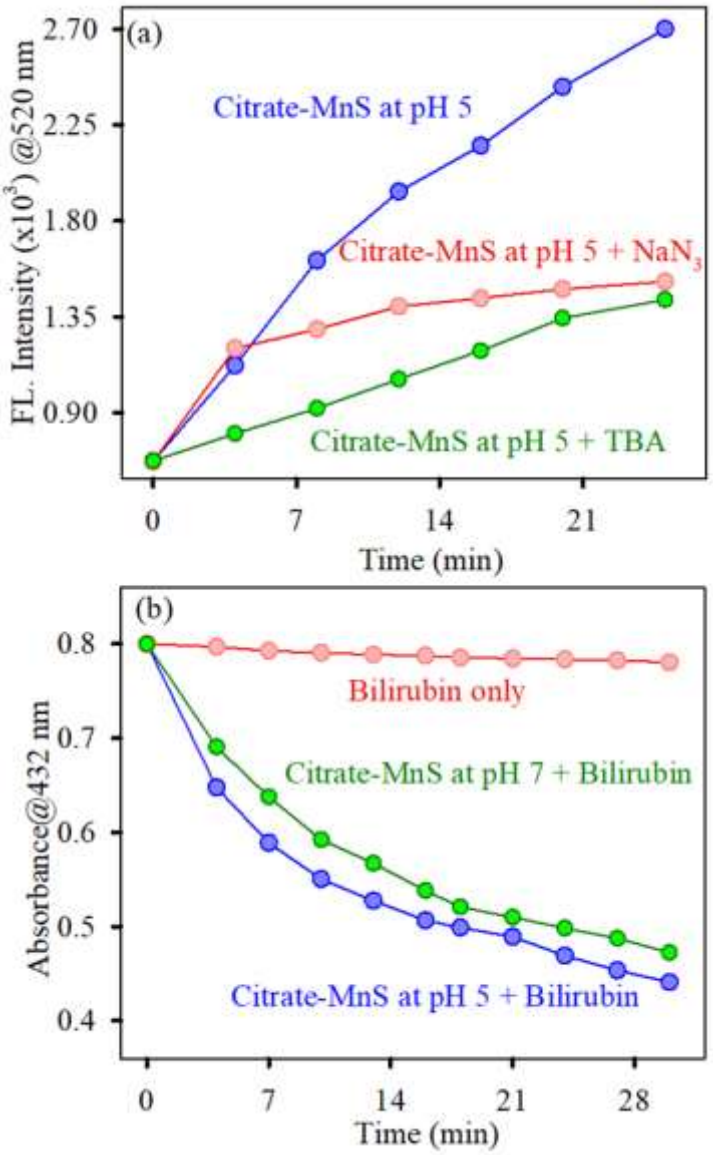


***Figure 8.4.*** *(a) DCFH oxidation (monitored at 520 nm) with time in presence of Citrate-MnS at pH 5 with singlet oxygen scavenger $NaN_3$ (red), hydroxyl radical scavenger (green) and without any scavenger (red). (b) Bilirubin degradation by citrate-MnS at pH 5 (blue), pH 7(green) and bilirubin only (red).*

Whereas, the degradation rate at acidic pH is much higher as compared to that of neutral pH. The significant production of ROS in acidic/neutral pH is responsible

for the degradation of bilirubin. Thus, the citrate-MnS NPs could be implemented as a potential therapeutic agent for hyperbilirubinemia. The antimicrobial activity of citrate-MnS has been examined against the *S. Hominis* growth to explore the therapeutic potential of citrate-MnS for use in anti-cancer and anti-tumor therapy.

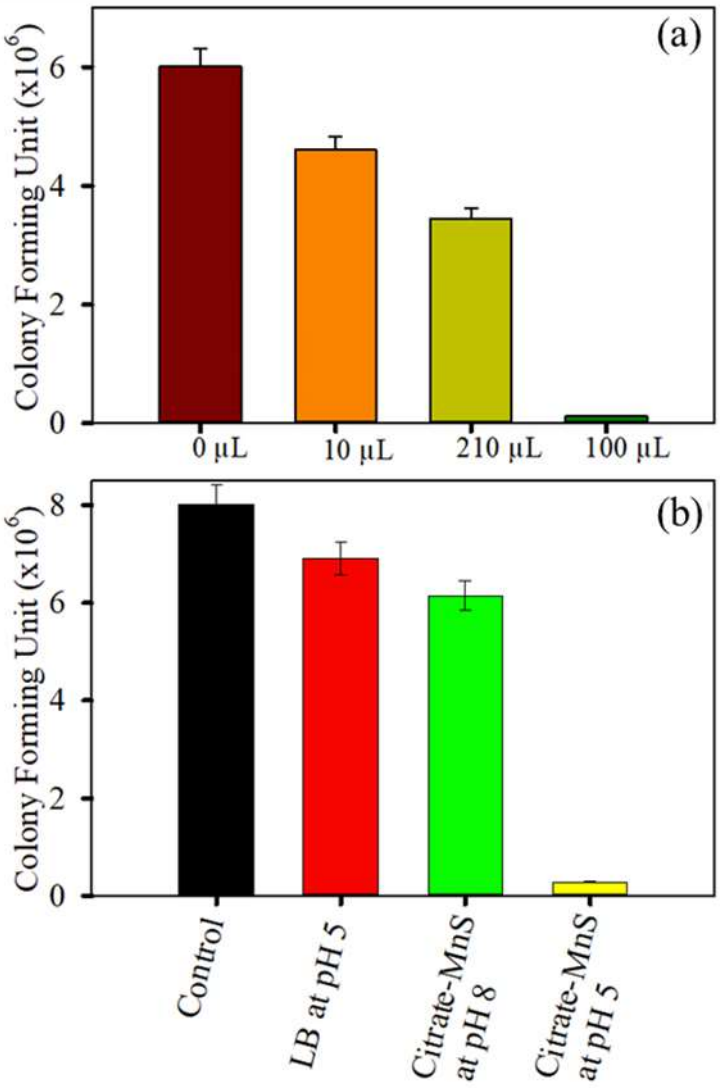


**Figure 8.5.** *(a) Dose-dependent antibacterial effect of citrate-MnS at concentrations ranging from 0 to 100 µL on S. hominis under dark conditions. (b) Bacterial viability after treatment with citrate-MnS at pH 5 and pH 8.*

The concentration dependent toxicity of citrate-MnS at pH 5 was examined on the growth of *S. Hominis* the colony-forming unit (CFU) assay under dark condition. At a concentration of 10 µL, a significant inhibition of bacterial growth is observed (Figure 8.5.a). To probe the antibacterial action 10 µL of as-prepared citrate-MnS have been used for incubating the culture for 3 h. As shown in Figure 8.5.b, less

number of colonies is observed (the bacterial growth is found to be decreased by 96% in CFU) for citrate-MnS treated plate at pH 5 which implies a significant antibacterial effect. Whereas, citrate-MnS treated plate at pH 8 exhibits less inhibition (the bacterial growth is observed to have decreased by 23% in CFU) against the growth of *S. Hominis*.

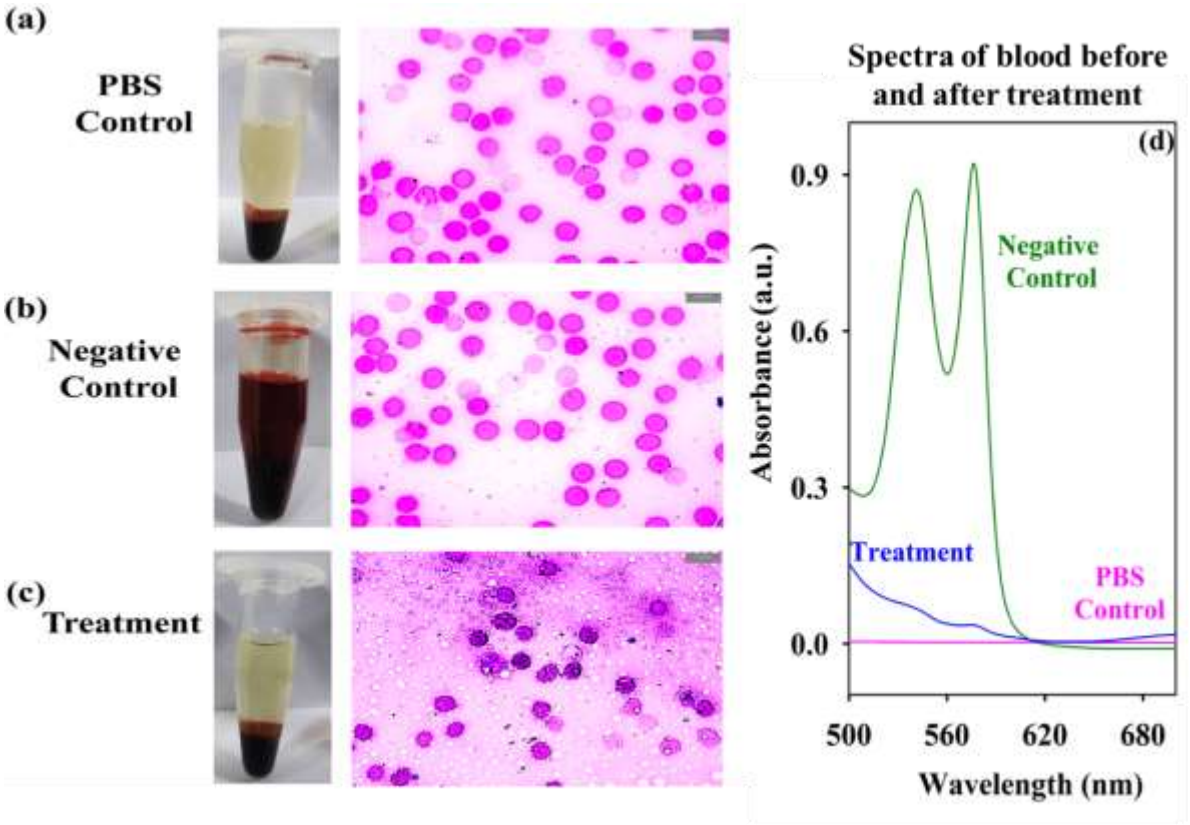


**Figure 8.6.** *Pictorial diagram for the hemolysis assay for (a) PBS Control (b) Negative control and (c) NPs treatement. (d) Absorbance of the supernatant showing the amount of hemolysis.*

To assess the cytotoxicity of the citrate-MnS the hemolysis assay on RBC was performed. We observed no significant hemolysis in the RBC samples treated with the NPs, as comparable to the PBS control group (Figure 8.6.a and 8.6.c). On the contrary, 100% hemolysis was observed in the negative control groups due to the rupture of the RBCs 9 (Figure 8.6.b). To further confirm our results we measured the absorbance of the supernatant (Figure 8.6.d) which shows absence of any q bands of hemoglobin in the treated group. Thus, our experiment suggests that the citrate-MnS NPs are is selective to the microorganisms, having no cytotoxicity to the RBC's. Overall, our study highlights the scope of developing citrate-MnS as a potent

antibacterial agent and potential therapeutic agent against hyperbilirubinemia. The ability of pH-triggered ROS production by citrate-MnS could be used by biomedical researchers to the utilization of these NPs in potential biological applications.

**8.3. Conclusion:** In summary, we have for the first time demonstrated that highly water-soluble citrate-MnS NPs exhibit intrinsic photoluminescence and can generate an excessive amount of ROS without any photo-activation. We have synthesized the as-prepared MnS NPs and functionalized by citrate ligand. We have characterized the uncapped MnS NPs using XRD and HRTEM. The surface functionalization makes the MnS NPs soluble in water. The citrate-MnS NPs exhibit LMCT and d-d band in UV-Vis absorption spectra and strong photoluminescence. FTIR spectra of both capped and uncapped MnS NPs were taken to confirm the surface functionalization of uncapped MnS NPs. DCFH assay was performed to measure ROS without any photo activation. Citrate-MnS NPs decompose bilirubin at acidic pH (pH 5). The pH-dependent disproportionation of manganese ions is responsible for the production of huge amount of ROS. Detection of singlet oxygen and hydroxyl radical has also been done using an appropriate scavenger. The antibacterial activity of the citrate-MnS NPs nanohybrid is confirmed from the CFU assay on gram-positive bacteria *S. Hominis*. A significant inhibition {(96%) in CFU} was observed for citrate-MnS NPs at pH 5. The efficacy of ROS production at acidic/neutral pH without any photo activation provides key aspects for multifunctional applications in human health. Therefore, multidisciplinary efforts are needed from biologists to obtain a clear understanding of citrate-MnS-based nanomedicine, which will further facilitate the clinical translation.

# References


[1] S. Goel, F. Chen, W. Cai, Synthesis and biomedical applications of copper sulfide nanoparticles: From sensors to theranostics, *Small* 10 (2014) 631.

[2] S. Suresh, Semiconductor nanomaterials, methods and applications: A review, Nanosci. *Nanotechnol*. 3 (2013) 62.

[3] G. Chen, I. Roy, C. Yang, P.N. Prasad, Nanochemistry and nanomedicine for nanoparticle-based diagnostics and therapy, *Chem. Rev.* 116 (2016) 2826.

[4] A. Deonarine, B.L. Lau, G.R. Aiken, J.N. Ryan, H. Hsu-Kim, Effects of humic substances on precipitation and aggregation of zinc sulfide nanoparticles, *Environ. Sci. Technol.* 45 (2011) 3217.

[5] K.A. Ubaid, X. Zhang, V.K. Sharma, L. Li, Fate and risk of metal sulfide nanoparticles in the environment, *Environ. Chem. Lett*. 18 (2020) 97.

[6] W. Wu, Q. He, C. Jiang, Magnetic iron oxide nanoparticles: Synthesis and surface functionalization strategies, *Nanoscale Res. Lett.* 3 (2008) 397.

[7] S. Liu, B. Yu, S. Wang, Y. Shen, H. Cong, Preparation, surface functionalization and application of $Fe_3O_4$ magnetic nanoparticles, *Adv. Colloid Interface Sci.* 281 (2020) 102165.

[8] X. Kang, B. Wang, L. Zhu, H. Zhu, Synthesis and tribological property study of oleic acid-modified copper sulfide nanoparticles, *Wear* 265 (2008) 150.

[9] T. Tabakova, V. Idakiev, D. Andreeva, I. Mitov, Influence of the microscopic properties of the support on the catalytic activity of Au/ZnO, Au/$ZrO_2$, Au/$Fe_2O_3$, Au/$Fe_2O_3$–ZnO, Au/$Fe_2O_3$–$ZrO_2$ catalysts for the WGS reaction, *Appl. Catal. A Gen.* 202 (2000) 91.

[10] J. Lee, N. Kumari, S.M. Kim, S. Kim, K.-W. Jeon, G.H. Im, M.-S. Jang, W.J. Lee, J.H. Lee, I.S. Lee, Anchoring ligand-effect on bright contrast-enhancing property of hollow $Mn_3O_4$ nanoparticle in T1-weighted magnetic resonance imaging, *Chem. Mater.* 30 (2018) 4056.

[11] P. Jain, K. Patel, A.K. Jangid, A. Guleria, S. Patel, D. Pooja, H. Kulhari, Biotinylated $Mn_3O_4$ nanocuboids for targeted delivery of gemcitabine hydrochloride to breast cancer and MRI applications, *Int. J. Pharm.* 606 (2021) 120895.

[12] T. Montini, M. Melchionna, M. Monai, P. Fornasiero, Fundamentals and catalytic applications of $CeO_2$-based materials, *Chem. Rev.* 116 (2016) 5987.
[13] M. Martínez-Carmona, Y. Gun'Ko, M. Vallet-Regí, ZnO nanostructures for drug delivery and theranostic applications, *Nanomaterials* 8 (2018) 268.
[14] Y. Guo, T. Park, J.W. Yi, J. Henzie, J. Kim, Z. Wang, B. Jiang, Y. Bando, Y. Sugahara, J. Tang, Nanoarchitectonics for transition-metal-sulfide-based electrocatalysts for water splitting, *Adv. Mater.* 31 (2019) 1807134.
[15] A. Asok, A.A. Naik, S. Arunachalam, R. Govindaraj, K. Haribabu, Microwave assisted synthesis of polythiophene–molybdenum sulfide counter electrode in dye sensitized solar cell, *J. Mater. Sci. Mater. Electron.* 30 (2019) 13655.
[16] M. Matoba, S. Anzai, A. Fujimori, Effect of early transition-metal (M= Ti, V and Cr) doping on the electronic structure of charge-transfer type compound NiS studied by thermoelectric power and X-ray photoemission measurements, *J. Phys. Soc. Japan* 63 (1994) 1429.
[17] J. Zhao, Y. Zhang, Y. Wang, H. Li, Y. Peng, The application of nanostructured transition metal sulfides as anodes for lithium ion batteries, *J. Energy Chem.* 27 (2018) 1536. [18] A.A. Sagade, R. Sharma, Copper sulphide ($Cu_xS$) as an ammonia gas sensor working at room temperature, *Sens. Actuators B Chem.* 133 (2008) 135.
[19] Y.N. Zhou, Y.R. Zhu, X.-Y. Chen, B. Dong, Q.-Z. Li, Y.-M. Chai, Carbon–based transition metal sulfides/selenides nanostructures for electrocatalytic water splitting, *J. Alloys Compd*. 852 (2021) 156810.
[20] L. Lu, M. Huang, Y. Huang, P.F.-X. Corvini, R. Ji, L. Zhao, $Mn_3O_4$ nanozymes boost endogenous antioxidant metabolites in cucumber (Cucumis sativus) plant and enhance resistance to salinity stress, *Environ. Sci. Nano* 7 (2020) 1692.
[21] N. Singh, Antioxidant metal oxide nanozymes: Role in cellular redox homeostasis and therapeutics, *Pure Appl. Chem.* 93 (2021) 187.
[22] A. Adhikari, S. Mondal, S. Darbar, S.K. Pal, Role of nanomedicine in redox mediated healing at molecular level, *Biomol. Concepts* 10 (2019) 160.
[23] J. Huang, Y. Dai, K. Singewald, C.C. Liu, S. Saxena, H. Zhang, Effects of $MnO_2$ of different structures on activation of peroxymonosulfate for bisphenol: A degradation under acidic conditions, *Chem. Eng. J.* 370 (2019) 906.

[24] I.G. Orletsky, M.I. Ilashchuk, E.V. Maistruk, H.P. Parkhomenko, P.D. Marianchuk, I.P. Koziarskyi, D.P. Koziarskyi, Electrical properties of heterostructures MnS/n-CdZnTe obtained by spray pyrolysis, *Mater. Res. Express.* 8 (2021) 015905.

[25] N. Zhang, R. Yi, Z. Wang, R. Shi, H. Wang, G. Qiu, X. Liu, Hydrothermal synthesis and electrochemical properties of alpha-manganese sulfide submicrocrystals as an attractive electrode material for lithium-ion batteries, *Mater. Chem. Phys.* 111 (2008) 13.

[26] T. Veeramanikandasamy, K. Rajendran, K. Sambath, P. Rameshbabu, Effect of Cu-doping on optical, electrical and magnetic properties of chemically synthesized MnS nanocrystals, *Mater. Chem. Phys.* 171 (2016) 328.

[27] M. Li, Q. Zhao, X. Yi, X. Zhong, G. Song, Z. Chai, Z. Liu, K. Yang, Au@ MnS@ ZnS core/shell/shell nanoparticles for magnetic resonance imaging and enhanced cancer radiation therapy, *ACS Appl. Mater. Interfaces* 8 (2016) 9557.

[28] S. Ramki, K. Pandi, S.M. Chen, Y.-T. Ye, T.-W. Chen, Q. Hao, Hydrothermal synthesis of manganese sulfide decorated graphene oxide for effective electrochemical sensing of dopamine, *Int. J. Electrochem. Sci* 14 (2019) 1069.

[29] S. He, W. Qiu, L. Wang, F. Gao, W. Wang, Z. Hu, Q. Wang, Hollow MnS nanospheres as electron transfer promoters of hemoglobin and their electrochemical sensing applications, *J. Mater. Sci.* 51 (2016) 7156.

[30] A. Bera, M. N. Hasan, N. Pan, R. Ghosh, R. Alsantali, H. M. Altass, R J. Obaid, S. A. Ahmed and S. K. Pal, Implementation of surface functionalization of MnS nanoparticle for achieving of novel optical properties and Improving Therapeutic Potential, RSC Adv. (2022) DOI: 10.1039/d2ra01087a.

[31] Y. Zhang, R. Xu, W. Chen, O. Zhuo, Q. Wu, J. Cai, X. Wang, Z. Hu, Solution–solid–solid growth of metastable wurtzite γ-MnS nanowires with controlled length, *J. Mater. Chem. C* 5 (2017) 6493.

[32] Y. Yuan, X. Yan, Y. Wang, Y. Xiong, C. Tian, Z. Lin, L. Chai, Interface effects on the phase transition of MnS nanocrystal, *Surf. Interfaces* 23 (2021) 101015.

[33] A. Giri, N. Goswami, C. Sasmal, N. Polley, D. Majumdar, S. Sarkar, S.N. Bandyopadhyay, A. Singha, S.K. Pal, Unprecedented catalytic activity of $Mn_3O_4$

nanoparticles: Potential lead of a sustainable therapeutic agent for hyperbilirubinemia, *RSC Adv.* 4 (2014) 5075.

[34] A. Giri, N. Goswami, M. Pal, M.T.Z. Myint, S. Al-Harthi, A. Singha, B. Ghosh, J. Dutta, S.K. Pal, Rational surface modification of $Mn_3O_4$ nanoparticles to induce multiple photoluminescence and room temperature ferromagnetism, *J. Mater. Chem. C* 1 (2013) 1885.

[35] A. Bera, D. Bagchi, S.K. Pal, Improvement of Photostability and NIR Activity of Cyanine Dye through Nanohybrid Formation: Key Information from Ultrafast Dynamical Studies, *J. Phys. Chem. A* 123 (2019) 7550.

[36] W. He, H.K. Kim, W.G. Wamer, D. Melka, J.H. Callahan, J.-J. Yin, Photogenerated charge carriers and reactive oxygen species in ZnO/Au hybrid nanostructures with enhanced photocatalytic and antibacterial activity, *J. Am. Chem. Soc* 136 (2014) 750.

[37] Z. Kang, X. Yan, L. Zhao, Q. Liao, K. Zhao, H. Du, X. Zhang, X. Zhang, Y. Zhang, Gold nanoparticle/ZnO nanorod hybrids for enhanced reactive oxygen species generation and photodynamic therapy, *Nano Res*. 8 (2015) 2004.

[38] R. Huang, E. Choe, D. Min, Kinetics for singlet oxygen formation by riboflavin photosensitization and the reaction between riboflavin and singlet oxygen, *J. Food Sci.* 69 (2004) C726.

[39] A.I. Cederbaum, A. Qureshi, G. Cohen, Production of formaldehyde and acetone by hydroxyl-radical generating systems during the metabolism of tertiary butyl alcohol, *Biochem. Pharmacol.* 32 (1983) 3517.

[40] A. Adhikari, N. Polley, S. Darbar, D. Bagchi, S.K. Pal, Citrate functionalized $Mn_3O_4$ in nanotherapy of hepatic fibrosis by oral administration, *Future Sci.* 2 (2016) FSO146.

# List of Publications

**(Peer-reviewed journals)**

1. **A. Bera**, D. Bagchi and S. K. Pal
"Improvement of Photostability and NIR Activity of Cyanine Dye through Nanohybrid Formation: Key Information from Ultrafast Dynamical Studies"
*The Journal of Physical Chemistry A* 123 (2019) 7550.

2. **A. Bera**, M. N. Hasan, U. Pal, D. Bagchi, T. K. Maji, T. Saha-Dasgupta, R. Das and S. K. Pal
"Fabrication of nanohybrids toward improving therapeutic potential of a NIR photo-sensitizer: An optical spectroscopic and computational study"
*Journal of Photochemistry and Photobiology A: Chemistry* 424 (2022) 113610.

3. **A. Bera**, M. N. Hasan, A. Chatterjee, D. Mukherjee and S. K. Pal
"Dual- Sensitization via Electron and Energy Harvesting in a Nanohybrid for Improvement of Therapeutic Efficacy" ACS Physical Chemistry Au"
*ACS Physical Chemistry Au* 3 (2022) 171.

4. **A. Bera**, M. N. Hasan, N. Pan, R. Ghosh, R. Alsantali, H. M. Altass, R J. Obaid, S. A. Ahmed and S. K. Pal
**"**Implementation of surface functionalization of MnS nanoparticle for achieving of novel optical properties and Improving Therapeutic Potential"
*RSC Advance (2022)* DOI: 10.1039/d2ra01087a.

5. T. Dutta, D. Bagchi, **A. Bera**, S. Das, T. Adhikari and S. K. Pal
"Surface Engineered ZnO-Humic/Citrate Interfaces: Photoinduced Charge Carrier Dynamics and Potential Application for Smart and Sustained Delivery of Zn Micronutrient"
*ACS Sustainable Chemistry & Engineering* 7 (2019) 10920.

6.* M. N. Hasan, A. Bera, T. K. Maji and S. K. Pal
"Sensitization of nontoxic MOF for their potential drug delivery

application against microbial infectionn"
*Inorganica Chimica Acta* 523 (2021) 120381.

7.* M. N. Hasan, **A. Bera**, T. K. Maji, D. Mukherjee, N. Pan, D. Karmakar and S. K. Pal
"Functionalized Nano-MOF for NIR Induced Bacterial Remediation: A Combined Spectroscopic and Computational Study"
*Inorganica Chimica Acta* 532 (2022) 120733.

8.* M. N. Hasan, T. K. Maji, U. Pal, **A. Bera**, D. Bagchi, A. Halder, S. A. Ahmed, J. H. Al-Fahemi, T. M. Bawazeer, T. Saha-Dasgupta, and S. K. Pal
"Wide bandgap semiconductor based novel nanohybrid for potentialantibacterial activity: Ultrafast Spectroscopy and Computational Studies"
*RSC Advances* 10 (2020) 38890.

9.* S. Rani, D. Bagchi, U. Pal, M. Kumari, M. Sharma, **A. Bera**, J. Shabir, S. K. Pal, T. Saha-Dasgupta, and S. Mozumdar
"The Role of Imidazolium-Based Surface-Active Ionic Liquid to Restrain the Excited-State Intramolecular H-Atom Transfer Dynamics of Medicinal Pigment Curcumin: A Theoretical and Experimental Approach"
*ACS Omega* 5 (2020) 25582.

10* M. Sharma, U. Pal, M. Kumari, D. Bagchi, S. Rani, D. Mukherjee, **A. Bera**, S. K. Pal, T. Saha-Dasgupta and S. Mozumdar
"Effect of solvent on the photophysical properties of isoxazole derivative of curcumin: A combined spectroscopic and theoretical study"
*Journal of Photochemistry and Photobiology A: Chemistry* 410 (2021) 113164.

11* M. M. Kumari, M. Sharma, D. Bagchi, S. Rani, D. Mukherjee, **A. Bera**, S. K. Pal and S. Mozumdar "Enhanced charge separation through modulation of defect-state in wide band-gap semiconductor for potential photocatalysis application: ultrafast spectroscopy and computational studies"
*Journal of Photochemistry and Photobiology A: Chemistry* 416 (2021)

113337.

12* D. Mukherjee, M. N. Hasan, R. Ghosh, G. Ghosh, **A. Bera,** E. S. Prasad, A. Hiwale, P. Vemula, R. Das and S. K. Pal
"Decoding the Kinetic Pathways Towards Lipid/DNA Complex of Alkyl-alcohol Cationic lipids formed in a Microfluidic Channel"
***The Journal of Physical Chemistry B*** 126 (2022) 588.

13* S. Mondal, N. Pan, R. Ghosh, **A. Bera**, D. Mukherjee, T.K. Maji, A. Adhikari, S. Ghosh, C. Bhattacharya and S. K. Pal
"Interaction of a Jaundice Marker Molecule with Redox Modulatory Nano- Hybrid: A Combined Electrochemical and Spectroscopic Study towards Development of a Theranostics Tool"
***ChemMedChem (2022).*** DOI: 10.1002/cmdc.202100660.

14* S. A. Ahmed, M. N. Hasan, H. M. Altass, **A. Bera**, R. I. Alsantali, N. Pan, A. Y. A. Alzahrani, D. Bagchi, J. H. Al-Fahemi, A. S. Khder, and S. K. Pal
"Photo Sensitization of Tri-hybrid Nanomaterial for Potential Removal of Antibiotic Burden and Bacterial Remediation: A Combined Spectroscopic and Computational Investigation"
***ACS Applied Nano Material*** 5 (2022) 4484.

15* S. Singh, A. Halder, A. Banerjee, M. N. Hasan, **A. Bera**, O. Sinha, S.K. Ghosh, A. Mitra, S. K. Pal
"An Optical Scattering Based Cost-Effective Approach Towards Quantitative Assessment of Turbidity and Particle Size Estimation In Drinking Water Using Image Analysis"
***Journal of Environmental Science & Engineering (2021).***

*Not included in the thesis

# List of International/ National Conferences

1. Poster entitled as "Improvement of Photostability and NIR Activity of Cyanine Dye Through Nanohybrid Formation: Key Information From Ultrafast Dynamical Studies" by **A. Bera** and S. K. Pal, was presented in the conference named ***International Conference on Nanoscience and Technology (ICONSAT 2020)*** held at S. N. Bose National Centre for Basic Sciences.

2. Attended the conference named Industry Academia Meet 2018 held at S. N. Bose National Centre for Basic Sciences, Kolkata on 6 October 2018.

3. Attended the conference named International Conference on Current Trends in Materials Science and Engineering, held at S. N. Bose National Centre for Basic Sciences, Kolkata in 2019